Università degli Studi di Trieste

Dipartimento di Fisica

Master Degree in Nuclear and Subnuclear Physics

Master Degree Thesis

Feasibility study for the measurement of the angular asymmetry in the production of a bottom quark-antiquark pair in electron-positron collisions with a center-of-mass energy of 91 GeV at the future accelerator FCC-ee at CERN

Author:
Leonardo Toffolin

Supervisor:
Prof. Marina Cobal

Co-supervisor:
Dr. Michele Pinamonti

Academic Year 2021/2022

Università degli Studi di Trieste

Dipartimento di Fisica

Master Degree in Nuclear and Subnuclear Physics

Master Degree Thesis

Feasibility study for the measurement of the angular asymmetry in the production of a bottom quark-antiquark pair in electron-positron collisions with a center-of-mass energy of 91 GeV at the future accelerator FCC-ee at CERN

Author:
Leonardo Toffolin

Supervisor:
Prof. Marina Cobal

Co-supervisor:
Dr. Michele Pinamonti

Academic Year 2021/2022

Università degli Studi di Trieste

Dipartimento di Fisica

Laurea Magistrale in Fisica Nucleare e Subnucleare

Tesi di Laurea Magistrale

Studio di fattibilità per la misura della asimmetria di produzione angolare di coppie di quark e antiquark di tipo bottom in collisioni elettrone-positrone con energia nel centro di massa di 91 GeV al futuro acceleratore FCC-ee al CERN

Candidato
Leonardo Toffolin

Relatore:
Prof. Marina Cobal

Correlatore
Dr. Michele Pinamonti

Anno Accademico 2021/2022

Abstract

The Standard Model (SM) of particle physics has proved to be an extremely successful theory of elementary interactions, and its predictions have been tested up to the per-mill level by a wide variety of measurements. On the other hand, several experimental facts require the extension of the Standard Model and explanations are needed for observations such as the domination of matter over antimatter, the evidence for *dark matter* and the non-zero neutrino masses. Theoretical issues that need to be addressed include the *hierarchy problem*, the neutrality of the Universe, the stability of the Higgs boson mass upon quantum corrections and the *strong CP problem*.

Global fits to electroweak precision data, comparing the measured values of different quantities with the SM predictions, provide important checks of the SM consistency and sensitivity to beyond-the-SM (BSM) effects. The two most sensitive determinations of $\sin^2\theta_{\mathrm{W,eff}}$, from the LEP measurement of the b-quark production forward-backward asymmetry at the Z-boson mass pole $A_{FB}^{0,b}$, and from the SLD measurement of A_ℓ, are in $\sim$3 σ tension with each other, constituting the largest deviation in global electroweak fits.

This issue has remained unsolved for the past 25 years, as documented by the flourishing literature regarding its possible nature. Possible BSM explanations would require a sizable correction to the right-handed $Zb\bar{b}$ coupling, keeping the left-handed $Zb\bar{b}$ coupling unchanged.

To shed light on this discrepancy, it is thus essential to exclude the possibility that it was caused by a statistical fluctuation or, even if almost excluded by dedicated studies, by some subtle underestimation of systematic experimental uncertainties. In both cases, it is clear that a new experimental, even indirect, determination of $A_{FB}^{0,b}$ is quite urgent.

This thesis belongs to the context of research for new physics in the electroweak sector at Z-pole, and consists in the presentation of a feasibility study on the measurement of an asymmetry, $A_{FB}^{0,b}$, in the associated production of a bottom quark-antiquark pair coming from a decaying Z-boson, at the future collider FCC-ee. This provides a clean observable, which is affected by hadronic uncertainties of both experimental and theoretical origin.

The definition of this asymmetry intrinsically requires some sensitivity to the charge of the bottom quark/antiquark in the final state, which represents an important experimental challenge.

By means of a fast-simulation based study, with the generation of samples of signal and background events from electron-positron collisions at the center-of-mass energy of 91 GeV, a simple technique for the b-quark charge identification is investigated, relying on charged particle tracks within the cone of the hadronic jet resulting from the its fragmentation process.

The directions of the reconstructed hadronic jets, together with the information on their identified charge, are then used to build the final observable. A simple unfolding technique is then implemented, and pseudo-experiments based on simulated data are performed in

order to estimate the expected statistical uncertainty and the main sources of systematic uncertainty in the proposed measurement.

The first projections for an $A_{FB}^{0,b}$ measurement at the FCC-ee are then reported, indicating the possibility of significantly improving on the current precision of the measurement performed at LEP.

Riassunto

Il Modello Standard della fisica delle particelle si è dimostrato essere un'ottima teoria delle interazioni fondamentali, e le sue predizioni sono state testate con una precisione del per-mille in un'ampia varietà di misure. D'altra parte, diverse considerazioni sperimentali richiedono un'estensione del Modello Standard e sono richieste ulteriori spiegazioni per osservazioni quali il dominio della materia sull'antimateria, l'evidenza della *materia oscura* e le masse non nulle dei neutrini. Le questioni teoriche che vanno indagate includono il *problema della gerarchia*, la neutralità elettrica dell'Universo, la stabilità della massa del bosone di Higgs e il problema della violazione della simmetria CP.

I fit globali sui dati di precisione del settore elettrodebole, confrontando i valori misurati delle diverse quantità con le predizioni del Modello Standard, forniscono importanti conferme della consistenza del modello stesso e della sensibilità ad effetti *oltre il Modello Standard* (BSM). Le due determinazioni più precise di $\sin^2\theta_{W,\text{eff}}$, dalla misura a LEP dell'asimmetria avanti-indietro nella produzione del quark bottom al polo della massa del bosone Z, $A_{FB}^{0,b}$, e dalla misura a SLD di A_l, sono in tensione a $\sim 3\sigma$ l'una con l'altra, costituendo la più grande deviazione nei fit globali elettrodeboli.

Questo problema è rimasto irrisolto negli ultimi 25 anni, come documenta la letteratura al riguardo. Possibili spiegazioni oltre il Modello Standard riguarderebbero significative correzioni all'accoppiamento right-handed $Zb\bar{b}$, lasciando invariato l'accoppiamento left-handed $Zb\bar{b}$.

Al fine di far luce su questa discrepanza, è pertanto necessario escludere la possibilità che sia causata da fluttuazioni statistiche o da una sottostima delle incertezze sustematiche sperimentali. In entrambi i casi, è chiaro che una nuova determinazione, anche indiretta, di $A_{FB}^{0,b}$ risulta urgente.

Questo lavoro di tesi appartiene al contesto della ricerca di nuova fisica nel settore elettrodebole al polo del bosone Z, e consiste nella presentazione di uno studio di fattibilità nella misura dell'asimmetria $A_{FB}^{0,b}$ nella produzione associata di una coppia quark/antiquark bottom dal decadimento di un bosone Z, al futuro acceleratore leptonico FCC-ee. Questo produce un'osservabile pulita, benché affetta da incertezze adroniche di origine sia sperimentale sia teorica.

La definizione di questa asimmetria richiede intrinsecamente una certa sensibilità alla carica del quark/antiquark bottom nello stato finale, il che rappresenta un'importante sfida sperimentale.

Per mezzo di uno studio basato su una simulazione parametrica, con la generazione di eventi di segnale e fondo da collisioni elettrone-positrone ad un'energia nel centro di massa di 91 GeV, è applicata una semplice tecnica per l'identificazione della

carica elettrica del quark b; questa tecnica riguarda le tracce delle particelle cariche all'interno del cono del jet adronico risultante dal processo di frammentazione del b-quark stesso.

Le direzioni dei jet adronici ricostruiti, insieme all'informazione sulla loro carica, sono poi usate per costruire l'osservabile finale. Un semplice metodo di unfolding viene infine implementato, e sono generati degli pseudo-esperimenti basati sui dati simulati al fine di stimare l'incertezza statistica attesa e le principali fonti di incertezza sistematica nella misura proposta.

Le prime proiezioni per una misura di $A_{FB}^{0,b}$ a FCC-ee sono infine riportate, indicando la possibilità di un miglioramento significativo della precisione attuale nella misura svolta a LEP.

Contents

Chapter 1

1 Standard Model of fundamental interactions

The theory called *Standard Model* (SM) represents the state of the art of human understanding about the physics of elementary particles and their interactions. It is built using *Quantum Field Theory* (QFT), founded on Quantum Mechanics [1] and it is based on the combination of several sub-theories which describe individual aspects of the model [2].

The Standard Model is a *gauge theory*, in which the interactions among the matter constituents are determined by *gauge invariance* and carried by *gauge bosons* [3].

The Universe appears to be formed by just a few different particles. Atoms are the bound states of negatively charged electrons (e^-) which orbit around a central nucleus composed of positively charged protons (p) and electrically neutral neutrons (n). The electrons are bound to the nucleus by the electrostatic attraction between opposite charges, which is the low-energy manifestation of the fundamental theory of electromagnetism, called *Quantum Electrodynamics* (QED). The rich structure of the properties of the periodic table elements emerges from quantum mechanics, which dictates the precise electronic structure of the different atoms. In the atomic nucleus, the protons and neutrons are bound together by the strong nuclear force, which is the manifestation of the fundamental theory of strong interactions, namely *Quantum Chromodynamics* (QCD). The fundamental interactions of particle physics are completed by the weak force, that is responsible for the nuclear β-decays of certain radioactive isotopes and the nuclear fusion processes that fuel the Sun and the other stars. In both nuclear β-decay and nuclear fusion, another particle, the nearly massless *electron neutrino* (ν_e) is produced. Almost all commonly encountered physical phenomena can be described in terms of the electron, electron neutrino, proton and neutron, interacting via the electromagnetic, strong and weak forces. Gravity, however, is not included in the SM framework, as discussed in Section 1.2.

The picture is completed by gravity, which although extremely weak, is always attractive and is therefore responsible for large-scale structure in the Universe.

1.1 Classification of the SM particles

As all the quantum field theories, a Lagrangian $\mathscr{L}$ is what sets the behaviour of the SM, as well as its kinematics and dynamics. The SM Lagrangian divided into several pieces [4]:

$$\mathscr{L} = \mathscr{L}_{\text{Gauge}} + \mathscr{L}_{\text{Matter}} + \mathscr{L}_{\text{Yukawa}} + \mathscr{L}_{\text{Higgs}} \tag{1}$$

The first piece is the pure gauge Lagrangian, given by:

$$\mathscr{L}_{\text{Gauge}} = -\frac{1}{2}\text{Tr}\big(\mathbf{G}^{\mu\nu}\mathbf{G}_{\mu\nu}\big) - \frac{1}{8}\text{Tr}\big(\mathbf{W}^{\mu\nu}\mathbf{W}_{\mu\nu}\big) - \frac{1}{4}B^{\mu\nu}B_{\mu\nu} \tag{2}$$

where $\mathbf{G}^{\mu\nu}$, $\mathbf{W}^{\mu\nu}$ and $B^{\mu\nu}$ are the gluon, weak, and hypercharge field-strength tensors. These terms contain the kinetic energy of the gauge fields and their self-interactions.

The next piece is the matter Lagrangian, given by:

$$\mathscr{L}_{\text{Matter}} = \bar{Q}^i_L i\gamma^\mu D_\mu Q^i_L + \bar{u}^i_R i\gamma^\mu D_\mu u^i_R + \bar{d}^i_R i\gamma^\mu D_\mu d^i_R + \bar{L}^i_L i\gamma^\mu D_\mu L^i_L + \bar{e}^i_R i\gamma^\mu D_\mu e^i_R, \tag{3}$$

where Q^i_L and L^i_L are the quark and lepton doublets, and a sum of the index i, which represents the generation, is implied. This piece contains the kinetic energy of the fermions and their interactions with the gauge fields, which are contained in the covariant derivatives D_μ.

The next piece of the Lagrangian consists in the Yukawa interaction of the Higgs field with the fermions, given by:

$$\mathscr{L}_{\text{Yukawa}} = \Gamma^{ij}_u \bar{Q}^i_L \epsilon \phi^* u^j_R - \Gamma^{ij}_d \bar{Q}^i_L \phi d^j_R - \Gamma^{ij}_e \bar{L}^i_L \phi e^j_R + \text{h.c.}\ ^1, \tag{4}$$

where the coefficients Γ_u, Γ_d, Γ_e are 3×3 complex matrices.

The last term is the Higgs Lagrangian, given by:

$$\mathscr{L}_{\text{Higgs}} = (D^\mu \phi)^\dagger D_\mu \phi + \mu^2 \phi^\dagger \phi - \lambda(\phi^\dagger \phi)^2. \tag{5}$$

This piece contains the kinetic energy of the Higgs field ϕ, its gauge interactions, and the Higgs potential (see Section 1.2.4).

The SM is also a gauge theory, one where the Lagrangian does not change under a set of transformations, namely *gauge transformations*, and as such is built on the local symmetries of its components:

$$SU(3)_C \times SU(2)_L \times U(1)_Y. \tag{6}$$

The $U(n)$ is the n-dimensional *Unitary Group*, a symmetry group which can be represented as a set of $n \times n$ matrices with the property that:

$$U^\dagger U = U U^\dagger = I \tag{7}$$

[1] $\epsilon = i\sigma_2$ is the total antisymmetric tensor in two dimensions, related to the second Pauli matrix σ_2, required to ensure each term separately to be electrically neutral. The expression "h.c." indicates the hermitian conjugate.

or, equivalently:

$$U^\dagger = U^{-1} \tag{8}$$

where the *dagger* (†) indicates the hermitian conjugate (complex conjugate and transpose) and I is the identity matrix. The $SU(n)$ is the *Special Unitary Group*, which can be represented as the set of $n \times n$ unitary matrices with determinant equal to 1. These three symmetry groups represent the component field theories of the SM: in particular, the strong force is given by $SU(3)$, while $SU(2) \times U(1)$ are the groups related to the weak and electromagnetic forces, mixed together, as discussed in Section 1.2.

The SM, in its minimal extension (often called *Minimal Standard Model*, MSM), describes 17 fundamental types of elementary particles [2] (see Fig. 1) which get sorted into two major groups (and several sub-groups) according to their characteristics, with the major division based on *spin* (that is the intrinsic angular momentum). These groups are *fermions*, particles with half integer spin, and *bosons*, particles with integer spin [3].

1.1.1 Fermions

The fundamental fermions represent the particles which make up what is traditionally thought of as "matter" (i.e. atoms). Due to the spin-statistics theorem, fermions obey the *Pauli exclusion principle*, which states that two identical fermions cannot occupy the same quantum state. The consequence of the exclusion principle is that gives rise to macroscopic matter built from composite fermion states. Elementary SM fermions are subdivided further into two groups: quarks and leptons [5].

Leptons do not experience strong interactions, while quarks do. Quarks, as well as *gluons* (which are the mediators of the strong interaction) can not be seen as free particles, but they appear as composite bound states called *hadrons*; hadrons can be then divided into the *baryons*, which are bound states of three quarks, and *mesons*, which are bound states of a quark and an antiquark.

Leptons Leptons, from the greek $\lambda\epsilon\pi\tau\acute{o}\varsigma$ for "light" [3], are elementary spin-1/2 particles which do not feel the strong force, since they do not exhibit colour charge, but experience weak and electromagnetic interactions. Similar to quarks, as mentioned

[2] The term "elementary" referred to a particle indicates the absence of a structure in that particle, which is thus not decomposable into other particles.

[3] The greek word $\lambda\epsilon\pi\tau\acute{o}\varsigma$ refers to the fact that the first two negative-charged leptons which had been discovered, which are the electron (by J. J. Thomson in 1896) and the muon (thanks to the experiment by M. Conversi, E. Pancini and O. Piccioni in 1947) were much lighter than the proton and neutron.

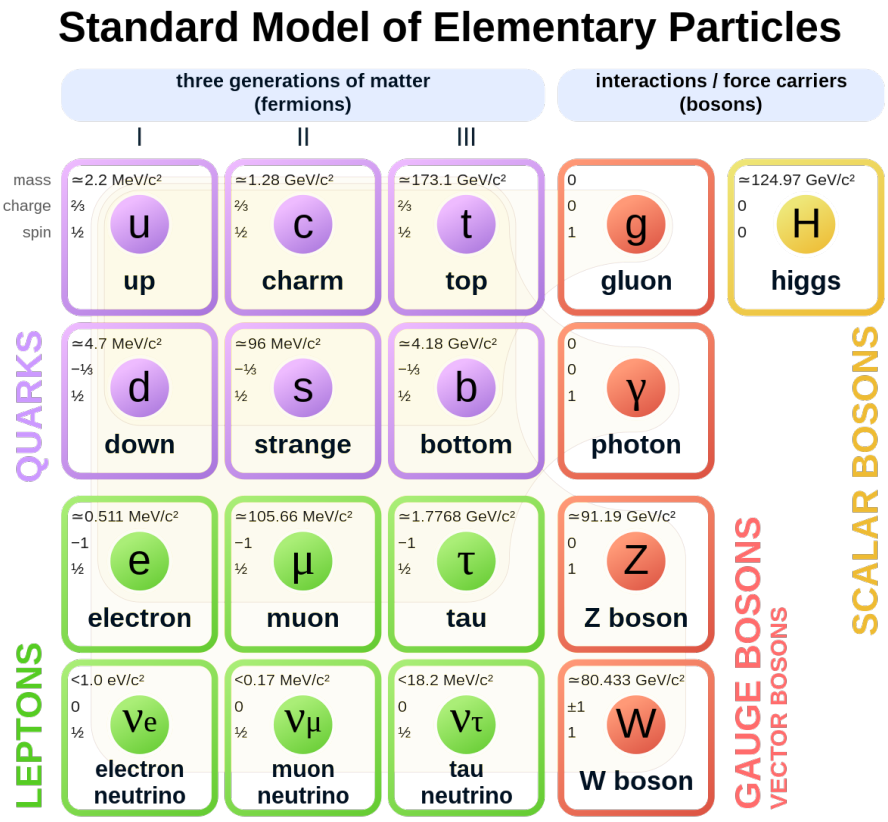

Fig. 1: Table of the SM particle content, organized by spin-statistics (fermions/bosons), flavour (quarks/leptons), and by generations. Each entry indicates the mass, charge, and spin of the particle in the upper left-hand corner. The table shows also the gauge and Higgs bosons described in Section 1.1.2.

in Section 1.1.1, leptons come in six flavors and are organized into three families, or *generations* of matter, of increasing mass; in each one, the negative-charged lepton and its correspondent neutral neutrino are organized in an *isospin doublet* in the context of weak interactions. The SM leptons are reported in Tab. 1.

Generation	Lepton	Symbol	Q	T_3	Mass $[MeV]$
1^{st}	electron neutrino	ν_e	0	$+1/2$	$< 10^{-4}$
	electron	e^-	-1	$-1/2$	0.511
2^{nd}	muon neutrino	ν_μ	0	$+1/2$	< 1
	muon	μ^-	-1	$-1/2$	105.658
3^{rd}	tauon neutrino	ν_τ	0	$+1/2$	< 100
	tauon	τ^-	-1	$-1/2$	1776.86

Tab. 1: The six leptons in the Standard Model. Electric charge (Q) is reported with respect to the fundamental charge of the electron, $e = -1.60 \cdot 10^{-19}\, C$.

The electron has been discovered by Joseph John Thomson (1856-1940) in 1896 and identified as the component of the cathode rays. Its charge-to-mass ratio is independent of the cathode material. Its electric charge $e = -1.60 \cdot 10^{-19}\, C$ has been determined in 1909 by Robert Andrews Millikan (1868-1953) and it is the fundamental charge in Nature. The electron is a stable particle, which does not decay in other particles.

The muon has been seen for the first time in the penetrating component of the cosmic rays by Seth Henry Neddermeyer (1907-1988) and Carl David Anderson (1905-1991) in the 1930's. During World War II some of its features were investigated, in order to establish whether it coincided with the so-called *pion*, the meson postulated by Hideki Yukawa (1907-1981) as the mediator of the nuclear interaction between the proton and the neutron. In particular, the experiment made up by Marcello Conversi (1917-1988), Ettore Pancini (1915-1981) and Oreste Piccioni (1915-2002) shed light on this *mesotron puzzle*, showing that the muon is effectively a lepton and not the mediator of the strong (nuclear) force. A muon can be essentially considered as a heavier version of the electron, with mass $m_\mu \simeq 200\, m_e$, and has a lifetime $\tau_\mu = 2.2 \cdot 10^{-6}\, s$, which makes it a quasi-stable particle. It decays in the leptonic channel:

$$\mu^- \longrightarrow e^- + \bar{\nu}_e + \nu_\mu \tag{9}$$

The tau lepton (or tauon) has been discovered in the Mark I experiment at DESY (*Deutsches Elektronen-Synchrotron*, near Hamburg, Germany) in 1975, through e^+e^- collisions. The tauon has a mass $m_\tau \simeq 3500\, m_e$ and lifetime $\tau_\tau = 2.9 \cdot 10^{-13}\, s$, being then a long-lived, but unstable particle. Tauon has a mass heavy enough to produce hadrons, besides decaying leptonically in a similar way as the muon:

$$\tau^- \longrightarrow e^- + \bar{\nu}_e + \nu_\tau \tag{10}$$

$$\tau^- \longrightarrow \mu^- + \bar{\nu}_\mu + \nu_\tau \tag{11}$$

As confirmed by many experiments, the strenght of the electro-weak interactions of leptons are identical, i.e. there is basically no difference between lepton generations, except for the mass. This fact is called *lepton universality*, and is relevant in the calculation of the *interaction amplitudes* in the Feynman diagrams.

Quarks Quarks [4] are the elementary constituents of hadrons and are defined by a key characteristic, the exibition of the *colour charge*; they are the only known

[4] The work "quark" was chosen by M. Gell-Mann inspired by the book *Finnegans Wake*, by James Joyce.

elementary particles to interact with all four fundamental forces (strong, weak, electromagnetism and gravity). They have spin equal to 1/2 and a fractional electric charge Q, either $\pm\frac{2}{3}e$ or $-\pm\frac{1}{3}$.

Quarks come in six varieties, known as *flavours*, which are organized into three generations like for the leptons. The first generation is composed of the two lightest quarks: the up (u) quark which has an electric charge of $+2/3\,e$, and the down (d) quark which has an electric charge of $-1/3\,e$. All three generations of quarks contain both an up-type quark ($Q = +2/3\,e$) and a down-type quark ($Q = -1/3\,e$), where the key difference between the generations is the increasing mass value. The second generation is composed by the charm (c) and strange (s) quarks, and the third generation contains the top (t) and bottom (b) quarks.

Since the quarks in the second and third generations have higher masses, they will readily decay into the first generation quarks, which are nominally stable and therefore make up most of the stable matter of the Universe.

Generation	Quark	Symbol	Q	T_3	Mass $[GeV]$
1^{st}	up	u	$+2/3$	$+1/2$	0.003
	down	d	$-1/3$	$-1/2$	0.005
2^{nd}	charm	c	$+2/3$	$+1/2$	1.3
	strange	s	$-1/3$	$-1/2$	0.1
3^{rd}	top	t	$+2/3$	$+1/2$	174
	bottom	b	$-1/3$	$-1/2$	4.5

Tab. 2: The six quarks in the Standard Model. Like leptons, the three generations are organized in isospin doublets. Electric charge (Q) is reported with respect to the fundamental charge of the electron, $e = -1.60 \cdot 10^{-19}\,C$.

From a historically point of view, the theory of quarks was introduced independently by Murray Gell-Mann (1929-2019) and George Zweig (1937-) at the beginning of the 1960's, in order to expain the nature of all the known *resonances*, i.e. the unstable particles with a Breit-Wigner energy distribution discovered at that time in colliders and fixed target experiments [6]. In this model, *strange* particles like *kaons* and *hyperons* are made up by a combination of s quark and u, d quarks.

Later on, to the original quark model the *charm* quark was included after the discovery of the J/ψ resonance, both in the Brookhaven fixed target experiment and at SLAC (*Stanford Linear Accelerator Center*, California, United States) electron-positron linear collider in 1974 [7]. The J/ψ was then interpreted as a charm-anticharm quark bound state.

Finally, the quark model was extended to the third family thanks to the discovery of the Υ resonance, the bottom-antibottom bound state, by Leon Max Lederman

(1922-2018) in 1977 [8], and of the *top* quark by the $D0$ and CDF Collaborations in 1994 [9], at FNAL (*Fermi National Accelerator Laboratory*, usually called *Fermilab*).

1.1.2 Bosons

The fundamental bosons mediate all the SM interactions between particles. Unlike fermions, they do not obey the Pauli exclusion principle, so that more bosons can occupy the same quantum state. The five elementary bosons of the SM fall into one of two categories, based on their spin. If the boson's spin is equal to one ($s = 1$), then it is a *vector* boson. Whereas if the boson has spin equal to zero ($s = 0$), it is a *scalar* boson.

Gauge bosons Four of the five bosons described by the SM are vector bosons; these are the force-carrying particles of the fundamental interactions (gauge bosons). These bosons allow for interactions between particles as take place via exchange of the corresponding (virtual) gauge bosons. A *virtual particle* can be depicted as one that exists for a time interval Δt, linked to the energy ΔE of the particle that it upholds the uncertainty principle:

$$\Delta E \Delta t \geq \frac{\hbar}{2}. \tag{12}$$

The most familiar gauge boson is the carrier of the electromagnetic force: the *photon* (γ). The electromagnetic force, and by extension the photon, is responsible for most of the macroscopic phenomena that we experience. The photon has spin equal to 1, is chargeless, and only interacts with those particles which also have an electric charge, since charge is the intrinsic property of a particle which is related to the intensity of the electromagnetic force it undergoes. It is also massless, and this fact has two consequences:

- the photon will always travel at the speed of light in a vacuum;
- the electromagnetic interaction has infinite range [10].

The photon can not interact with itself: in fact, a photon can not produce another photon in vacuum, at leading order in QED.

The force carrier of the strong interaction are the *gluons* (g), which are responsible for keeping quarks together to form matter particles known as *hadrons*, which include all protons and neutrons that make up atoms. The gluons are more complicated than photons. A general $SU(n)$ gauge theory will have $n^2 - 1$ gauge bosons which mediate the interactions. For example there are 3 gauge bosons of the $SU(2)$ weak

force group. So for the $SU(3)$ strong force there are 8 gauge bosons which engage in the interaction, all of which are considered gluons (as opposed to "anti-gluons"). As the photon, gluons are also massless and electrically neutral. However, despite photons, gluons not only mediate, but also interact via the strong force, meaning they exhibit colour charge. This also means that gluons undergo self-interaction, being *non-abelian* [5] gauge bosons.

The weak force is likely the least familiar of the four forces, but it is responsible for radioactive decay, and thus plays a crucial role in the thermonuclear processes which occur in the center of the sun [11]. Unlike the other forces, it has two associated gauge bosons: the $W^{\pm}$ and Z spin-1 bosons.

The $W^{\pm}$-bosons have a charge of $\pm 1e$. This means that they are the only gauge bosons to interact via electromagnetic force, and that any interaction which involves a $W^{\pm}$ will change the electric charge by one unit, by flipping the isospin of the particles (fermions) involved in the interaction (*weak charged currents*). The Z-boson, instead, has no electric charge and can therefore only be involved in neutral interactions: in this case *weak neutral currents* emerge, without any isospin flipping or charge changing.

Both the $W^{\pm}$ and the Z have large masses, $m_W = 80.4\,GeV$ and $m_Z = 91.2\,GeV$ respectively, and therefore decay very rapidly. This limits the effective range of the weak interaction to very short length scales, which is what gives the force its name. These gauge bosons can also self-interact, as long as charge is conserved in the interaction, since they are non-abelian.

Higgs boson The last recent SM particle discovered is the Higgs boson (H), the only elementary scalar boson currently known. The Higgs boson discovery was announced in a joint press conference on 4^{th} July 2012 by the ATLAS and CMS Collaborations at the CERN laboratory, Geneva, Switzerland. The Higgs boson was an important discovery as it served as evidence of the underlying Higgs field, a quantum field which is responsible for the electroweak symmetry breaking (EWSB) and for giving particles their mass.

The inclusion of the Higgs field was necessary in order to keep the SM consistent with experimental evidence. Without it, the theory predicts that all the fundamental particles would be massless as a result of the symmetries of their respective field theories. However, it was known that several of these particles have mass; therefore, a mechanism was required to break the corresponding symmetries in order to explain the masses of SM bosons and fermions.

[5] "Non-abelian" boson means that the generator which is associated to that force-carrying boson commutes with the generator correspondent to another force-carrying boson.

In this way, similarly to how charge is the intrinsic property which indicates how strongly a particle interacts with the electromagnetic field, at the fundamental level, mass can be seen as the intrinsic property which describes how strongly a particle interacts with the Higgs field [12]. Thus, the mass of of an elementary particle is directly related to its coupling with the Higgs field. Unlike electromagnetism however, this only applies to particles at the elementary level; the mass of composite particles is given by their rest energy, which can be attributed to binding energy and the masses of their component particles.

1.1.3 Antimatter

The SM predicts that every particle has an associated antiparticle, a particle which is identical in every way except that their quantum numbers are reversed. For example, the *positron*, which is the antiparticle to the electron, discovered in 1932 by Anderson [13], has the same mass as the electron but opposite electric charge +1, according to Dirac equation [14] [15]. These particles are often denoted with an overline (bar), or if their charge is explicitly represented, then the sign is changed; for example: $\bar{c}$ and e^+ are the notations to indicate the charm antiquark and the positron.

There are two classes of fermions, based on their associated antiparticle. On the one hand, Majorana fermions are those which act as their own antiparticle i.e., the particle has no quantum numbers which change sign; alternatively, Dirac fermions are massive fermions which are not their own antiparticle. All the charged leptons are Dirac fermions, with their antiparticles having opposite electric charge. By convention, the charged leptons have a negative electric charge, with their antiparticles having positive electric charge. All quarks are also Dirac fermions, where their associated antiquarks have opposite electric charge and anticolour. The convention for quarks is that all up-type quarks have positive electric charge, and all down-type quarks have negative electric charge. It is not currently known if neutrinos are Dirac or Majorana fermions; this represents one of the many unanswered questions in particle physics.

Unlike the fermions, the majority of the elementary bosons in the SM are their own antiparticles. This category includes the photon, the Z boson, and the Higgs boson. Similar to the charged leptons, the two charged W bosons antiparticles differ only by the sign of their electric charge, meaning that they are each the other's antiparticle.

Moreover, each of the eight gluons described in Section 1.1.2 has an associated antiparticle, distinct to itself.

1.2 Fundamental interactions

This section discusses the quantum field theories which make up the SM, with the inclusion of the strong interaction, which is discussed in more detail later. The SM describes *strong*, *electromagnetic*, *weak interactions*, the Higgs mechanism and the Yukawa mechanism, which are responsible to the attribution of mass to the gauge bosons and fermions. *General relativity*, the geometric theory of gravitation in Physics [16], could not be included in the SM, since it seems to be incompatible with the mathematical framework of the SM, and this is a serious problem of the theory, in practice; gravity does not affect the processes undergoing among the elementary particles.

1.2.1 Quantum Electrodynamics

QED is the theory which describes the fundamental interactions of electromagnetism, developed by combining Maxwell's Equations with a relativistically-invariant gauge theory (via the Dirac Equation). Put simply, QED describes how the photon interacts with charged particles.

In its simplest form, QED describes two basic processes: scattering and annihilation. Scattering, in the context of QED, describes the action in which any two charged particles interact by exchanging a photon in between them. This can include when any two like-charged particles repel each other, or when two different oppositely-charged particles attract each other. Annihilation, on the other hand, is the process that occurs when a particle and its associated antiparticle collide; the total energy and momentum of the initial pair are conserved in the process and distributed among a set of other particles in the final state.

Coupling constants As the first experimentally successful quantum field theory, QED introduces several concepts which are crucial to all the component theories of the SM. One such concept is that of a *coupling constant*, a parameter which determines how strongly a particle (usually a fermion) will interact with the force-mediator (which is a boson). The coupling constant of QED is the particle's charge, Q; then an electron will couple to the photon with an intensity given by e. These coupling constants are important since they play a role in determining *cross-sections* (σ), which can be thought of as a probability for a given interaction to occur.

As an example, the cross-section for an electron and a positron annihilating to create a muon-antimuon pair (see Fig. 2a) is proportional to e^4 since all four particles have charge equal to $|e|$:

$$\sigma(e^+e^- \longrightarrow \mu^+\mu^-) \propto e^4 \tag{13}$$

Alternatively, if the electron-positron pair annihilate to form a quark-antiquark pair (see Fig. 2b), the cross-section would be:

$$\sigma(e^+e^- \longrightarrow q\bar{q}) \propto e^2Q^2 \tag{14}$$

where Q refers to the charge of the quarks (either $\pm\frac{2}{3}e$ or $\pm\frac{1}{3}e$). There is, of course, a lot of other information which may impact on the cross-section, such as the mass and energies, and eventually the colours of the particles involved, but the coupling constant serves as a simple way to estimate the relative magnitude of the probability of a process.

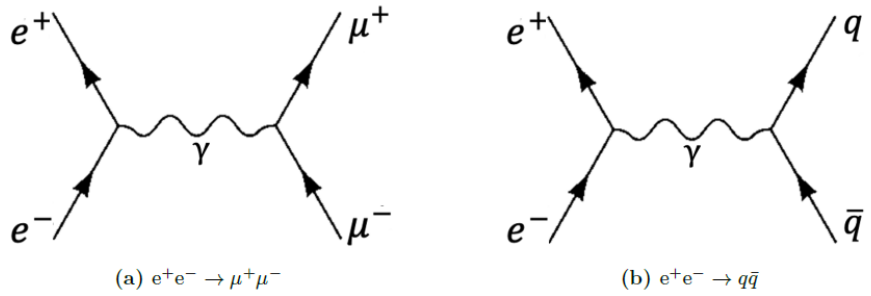

(a) $e^+e^- \to \mu^+\mu^-$ (b) $e^+e^- \to q\bar{q}$

Fig. 2: Feynman diagrams for two elementary processes: (a) annihilation of an electron-positron pair to produce a muon-antimuon pair via a virtual photon. (b) annihilation of an electron-positron pair to produce a quark-antiquark pair via a virtual photon. In both these so-called s-channel diagrams, time runs along the horizontal axis, and position runs along the vertical axis.

1.2.2 The weak interaction

The weak interaction comes in two major components: the charged and neutral current interactions. Neutral current interactions are those mediated by a Z-boson. Since it has no electric charge, the Z-boson can only engage in scattering processes in which the total charge of the incoming and outgoing particles is the same. Therefore, in terms of types of interactions, the Z-boson behaves very similarly to the photon, or in fact as any neutral boson. However its large mass makes it far less likely to be present in a process instead of a photon in any given interaction. One such interaction where the neutral current can work in a way similar to the photon is in high-energy processes such as the Drell-Yan Process [17] (see Fig. 3), where a quark-antiquark pair annihilate to produce a virtual photon, Z-boson, or Higgs boson, and each of

them can then pair produces leptons. [6] However, unlike photons, the Z-boson can interact with neutrinos (although very weakly) and serves as the only SM mediator for *neutrino-neutrino scattering* phenomena.

The charged current interactions are instead those mediated by the $W^{\pm}$-bosons. These processes can exchange particles between different fermion generations, and involve the exchange of electric charge. Two example processes are given by:

$$\begin{aligned} \mu^- &\longrightarrow \nu_\mu + W^- \\ W^- &\rightarrow e^- + \bar{\nu}_e \end{aligned} \tag{15}$$

$$\begin{aligned} c &\longrightarrow s + W^+ \\ W^+ &\rightarrow u + \bar{d} \end{aligned} \tag{16}$$

where the intermediary (virtual) $W^{\pm}$-boson decays to a fermion in association with the antiparticle of its same family partner such that charge is conserved. The charged current can also transform ("mix") quarks of one generation to quarks of a different one, for instance $c \rightarrow d + W^+$, but these interactions are suppressed (that is, are less likely to happen) in comparison to the transformation inside the same family.

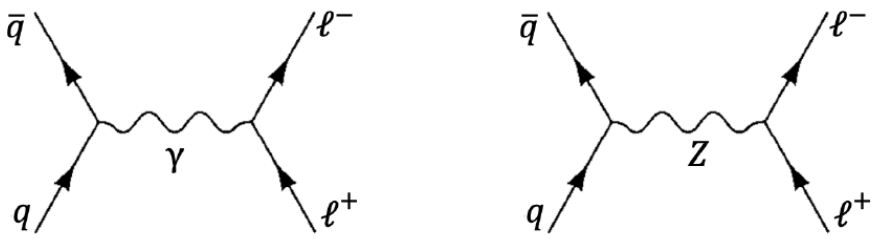

(a) $q\bar{q} \rightarrow \gamma \rightarrow \ell^-\ell^+$ (b) $q\bar{q} \rightarrow Z \rightarrow \ell^-\ell^+$

Fig. 3: Feynman diagrams of the Drell-Yan process mediated by a photon (a) and a neutral Z boson (b). Like Fig. 2, in both s-channel diagrams time runs along the horizontal axis, and position runs along the vertical axis.

Unlike for the quark sector, mixing between lepton generations is forbidden due to the conservation of *lepton flavor*, wherein every lepton generation is assigned a number and this must (in most cases, with some notable exceptions) be conserved through any process [18].

[6] The process can also proceed via a charged W^+ or W^-, but this produces a charged lepton and a neutrino in the final state [17].

CKM Matrix

The probability for any quark to transform to any other quark of opposite (up/down) type is given by taking the square of the corresponding element in the unitary *Cabibbo-Kobayashi-Maskawa* (CKM) matrix [19] [20]: [7]

$$V_{CKM} = \begin{bmatrix} V_{ud} & V_{us} & V_{ub} \\ V_{cd} & V_{cs} & V_{cb} \\ V_{td} & V_{ts} & V_{tb}. \end{bmatrix}$$

In this representation, the CKM matrix gives the amplitude for a down-type quark to couple to an up-type quark. The diagonal elements give the transition amplitude for the generational mixing, while the off-diagonal elements give the intergenerational mixing amplitudes. In this case, the diagonal elements all have a magnitude close to (but not equal to) 1, and the off diagonal elements [8] all have magnitudes much less than 1, as reported in Ref. [21]:

$$V_{CKM} = \begin{bmatrix} 0.974 & 0.218 & 0.004 \\ 0.218 & 0.975 & 0.040 \\ 0.008 & 0.039 & 0.997. \end{bmatrix}$$

Chirality and weak isospin

An important concept, which has major implications for the weak force, is the concept of *handedness*, which is based on a fermion's chirality. The chirality of a fermion can be determined through action of the projection operators:

$$\begin{aligned} L &= \frac{1}{2}(1 - \gamma^5) \\ R &= \frac{1}{2}(1 + \gamma^5) \end{aligned} \tag{17}$$

where L and R give the left-handed and right-handed component of the fermion field, respectively. L and R are usually called *Weyl operators* and, when applied to a Dirac fermion field ψ, are said to give the two left- and right-handed *Weyl spinors* ψ_L and ψ_R. In Eq. 17, $\gamma^5 = i\gamma^0\gamma^1\gamma^2\gamma^3$ is the "fifth gamma" matrix operator, with γ^μ ($\mu = 0, 1, 2, 3$) being the Dirac gamma matrices. The gamma matrices, in Dirac representation, are defined using 2×2 block matrices, as:

[7] As mentioned in Eq. 7, unitarity condition implies that $V_{CKM}^\dagger V_{CKM} = I$.
[8] Note that the generic element V_{ij} of the CKM matrix must be $0 \leq V_{ij} \leq 1$.

$$\gamma^0 = \begin{pmatrix} I_2 & 0_2 \\ 0_2 & -I_2 \end{pmatrix}, \quad \gamma^i = \begin{pmatrix} 0_2 & \sigma^i \\ -\sigma^i & 0_2. \end{pmatrix}$$

where I_2 is the 2×2 identity matrix, 0_2 is the 2×2 zero-matrix and the σ^i, $i = 1, 2, 3$ are the corresponding Pauli spin matrices. Therefore γ^5 is given by:

$$\gamma^5 = \begin{pmatrix} 0_2 & I_2 \\ I_2 & 0_2 \end{pmatrix}$$

which is not a "true" gamma matrix, but it is crucial for determining fermion's chirality (and therefore its handedness).

Using this handedness, the third component of the *weak isospin*, T_3, can be determined. T_3 behaves as an additional quantum number and must be overall conserved in all weak interactions. As a rule, all right-handed fermions (and so left-handed antifermions) have $T_3 = 0$. Meanwhile, left-handed fermions (and so right-handed antifermions) can have $T_3 = \pm\frac{1}{2}$; negative charge fermions have negative T_3, while their generational counterpart (both the positive quarks and the neutral leptons) have positive T_3. The charged $W^\pm$ bosons have $T_3 = \pm 1$ respectively, while the Z boson presents $T_3 = 0$: this implies that the charged weak current mediators can only engage with left-handed fermions.

1.2.3 Electroweak theory and electroweak symmetry breaking

Although the electromagnetic and the weak force seem very different at macroscopic level, at very high energies the two forces are described by a unified $SU(2)_L \times U(1)_Y$ theory [9] known as electroweak theory (EWT). This unification is characterized by an energy scale known as the electroweak scale. This determines a critical temperature, $T_C = 159$ GeV [22], below which the theory undergoes electroweak symmetry breaking, via the Higgs mechanism, and results in the two separate forces.

EWT introduces a new quantum number, *weak hypercharge* (Y), which is the symmetry of the $U(1)$ component of the theory. Since the symmetries are broken by interacting with the Higgs field [10], neither Y nor T_3 are totally conserved [11], but the combination of the two is conserved:

$$Q = T_3 + Y \tag{18}$$

[9] The subscript L refers to the fact that the gauge bosons $W^\pm$, always couple to left-handed currents.

[10] Remember that if the symmetries in SM were not broken by the interaction with the Higgs scalar complex field, then all the SM particles would be massless.

[11] Note that weak isospin, T, is the symmetry of the $SU(2)$ component.

where Q is the usual electric charge, which must be conserved even through interactions with the Higgs field.

When unified, the electroweak theory mixes together the SM gauge bosons (γ, $W^{\pm}$, Z), except for the gluon, into massless and non-physical fields: W_i (for $i = 1, 2, 3$), the three component bosons of weak isospin, and B for weak hypercharge. These gauge bosons have their own associated coupling constants, g and g', for T and Y respectively. After electroweak symmetry breaking (indicated with EWSB), the first two components of W_i fields become the familiar $W^{\pm}$ bosons, in the form:

$$W^{\pm} = \frac{1}{\sqrt{2}}\big(W_1 \mp iW_2\big) \tag{19}$$

and acquire mass thanks to the interaction with the Higgs field. The remaining W_3 and B non-physical bosons get mixed together to form two different neutral gauge bosons: one (Z_μ) acquires a mass, the other (A_μ) remains massless; these two fields are those of the Z boson and the photon, respectively. This mixing is usually expressed by the introduction of a 2D rotation matrix parameterized by the *weak mixing angle*, θ_W, as shown in Eq. 20:

$$\begin{pmatrix} Z_\mu \\ A_\mu \end{pmatrix} = \begin{bmatrix} \cos\theta_W & -\sin\theta_W \\ \sin\theta_W & \cos\theta_W \end{bmatrix} \begin{pmatrix} W_3 \\ B \end{pmatrix} \tag{20}$$

Moreover, this mixing causes the mass difference between the three gauge bosons of the weak interaction [23].

If EWT had only been described by a $SU(2)$ symmetry, then the spontaneous symmetry breaking would have resulted in three gauge bosons, one neutral and two charged, all with the same mass. However, this would not explain the photon as a massless gauge boson in QED. The inclusion of $U(1)_Y$ hypercharge allows for the proper resultant gauge bosons, but causes an asymmetry in the weak boson masses, with their ratio given by:

$$\frac{m_W}{m_Z} = \cos\theta_W \tag{21}$$

Experimentally, the masses of the vector bosons W and Z are respectively [24]:

$$m_W = 80.379 \pm 0.012\, GeV \tag{22}$$

$$m_Z = 91.1876 \pm 0.0021\, GeV \tag{23}$$

Due to their huge masses, the W and Z gauge bosons are unstable particles, with a

lifetime equal to the inverse of the relative full decay width [24]:

$$\Gamma_W = 2.085 \pm 0.042\, GeV \tag{24}$$

$$\Gamma_Z = 2.4952 \pm 0.0023\, GeV \tag{25}$$

The weak mixing angle (Eqs. 20 and 21) is a useful parameterization, as W can be expressed both in terms of the EWT coupling constants and the elementary charge:

$$\cos\theta_W = \frac{g}{\sqrt{g^2 + g'^2}}, \tag{26}$$

$$\sin\theta_W = \frac{g'}{\sqrt{g^2 + g'^2}} = \frac{e}{g}. \tag{27}$$

1.2.4 Higgs field

The Higgs field ϕ is a scalar, complex field which has the form of a $SU(2)$ doublet [12]. Its potential $V(\phi)$ is:

$$V(\phi) = -\mu^2\phi^\dagger\phi + \frac{\lambda}{2}(\phi^\dagger\phi)^2 \tag{28}$$

where λ is a dimensionless coupling constant which determines the Higgs self-interaction, while μ determines where the potential is minimized and is dimensionally a mass. If $\mu^2 > 0$, then the minimum of the potential is displaced from zero, which breaks the $SU(2)$ symmetry. This causes the field to have a non-zero expectation value:

$$\langle\phi\rangle = \frac{1}{\sqrt{2}}\begin{pmatrix}0\\ v\end{pmatrix} \tag{29}$$

where v is called *vacuum expectation value* for the Higgs field and is given by:

$$v = \sqrt{\frac{\mu^2}{\lambda}} = \frac{1}{(\sqrt{2}G_F)^{\frac{1}{2}}} \simeq 246\, GeV/c^2 \tag{30}$$

with $G_F = 1.166 \times 10\grave{\imath}{-}5\, GeV^{-2}$ being the Fermi constant [24].

The effect of this broken symmetry is that it leaves only one neutral, scalar boson H, which acquires a non-zero mass (m_H), given by the self-interaction term:

$$m_H = \sqrt{2\lambda}v. \tag{31}$$

Since the Higgs field is responsible for the weak gauge boson masses, they too can be expressed in terms of the vacuum expectation value and a coupling constant,

[12] The two components of this scalar field are reals.

so that:

$$m_W = g\frac{v}{2}, \tag{32}$$

$$m_Z = \sqrt{g^2 + g'^2}\frac{v}{2}. \tag{33}$$

Of course, the Higgs field does not couple neither to the electromagnetic nor to the strong force (the field is both electrically and colour neutral), thus both the photon and the gluon remain massless.

Similarly, the mass of fermions (m_f) can be expressed in terms of v and a *Yukawa coupling* $g_{f\bar{f}}$, which represent the general interaction term for $H \to f\bar{f}$, so that:

$$m_f = g_{f\bar{f}}v \tag{34}$$

If the fermion mass is well known, this can serve as a useful tool for probing the Higgs coupling to the fermion.

1.2.5 Quantum Chromodynamics

Quantum Chromodynamics (QCD) is the colour-charge analog of QED and, as such, describes the strong interactions between quarks and gluons. The theory states that all quarks are charged under one of three, physically indistinguishable *colours*, usually denoted as the three primary colours: *red*, *green*, and *blue* (r; g; b). Anticolour ($\bar{r}$; $\bar{g}$; $\bar{b}$) is the analogous charge conjugate for QCD.

Antiquarks have both the opposite electric charge and colour charge of quarks. However, unlike electric charge, colour charge is not an observable property, and due to a property known as *colour confinement*, no coloured particles can exist in nature. As a consequence, isolated quarks cannot exist.

Furthermore, QCD is a non-abelian gauge theory; one where the elements of the symmetry group ($SU(3)_C$) do not commute. [13] Conversely, the $U(1)_Y$ symmetry group of QED is commutative, and is therefore an abelian gauge group.

Another major difference between QCD and QED is that the mediating gauge boson, in this case the gluon, also engages in the strong interaction. In order to conserve their colour charge, gluons must be doubly charged with one colour and one anticolour. Thus, for gluons to remain coloured objects and to have both a colour and anticolour charge, they must have a linear combination of different colour-anticolour pairs. One of the eight possible linearly independent combinations, corresponding to

[13] The subscript C indicates the fact that strong interactions involve colour quantum number.

the eight physically indistinguishable gluons, is reported below:

$$\frac{r\bar{b} - b\bar{r}}{\sqrt{2}} \tag{35}$$

These combinations are generated by the T_α operators:

$$T_\alpha = \frac{\lambda_\alpha}{2}, \quad \alpha = 1, \dots 8 \tag{36}$$

where the λ_α are the *Gell-Mann matrices*, the generalization of the Pauli spin matrices to $SU(3)$ symmetry group [25].

Confinement, hadronization and jets The property of QCD which states that colour-charged objects must exist in colour-singlet states known as hadrons, is called *colour confinement*. Due to this, all the particles found in nature are colour neutral. In the analogy with real colour (red, blue, green), confinement requires the hadrons to have the right combinations of colours which give white as the final state. There are two main classes of hadrons: mesons and baryons. Mesons are composite states of two quarks, one quark and one antiquark, which have one colour charge and the corresponding anticolour charge. On the other hand, baryons are three quark states (or three antiquarks) which have one of each of the three colours. The process of confinement can be explained by the fact that gluons also carry colour charge. Quarks interact by exchanging gluons, so as two quarks ($q\bar{q}$) are separated, the gluon field lines (the QCD analog of the electromagnetic field lines) form a sort of *flux tube* (as shown in Fig. 4) which has a fixed energy density and radius. As a result, the force between the two colour charges grows proportionally to the distance of the separation. This is different from what happens for the force between two electrically charged particles, which is proportional to $\frac{1}{r^2}$.

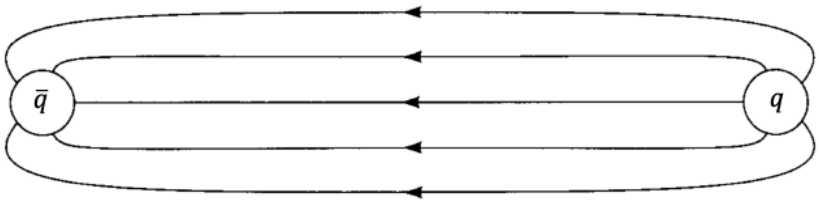

Fig. 4: Schematic diagram of the flux tube formed by the gluon field between two separating colour charges (i.e. quarks). Figure adapted from [2].

Thus, it requires an increasing amount of energy to keep the colour charges separated. The QCD potential between two quarks is then given by the sum of two

terms:

$$V_{QCD} = \underbrace{-\frac{4}{3}\frac{\alpha_S}{r}}_{asymptotic\,freedom} + \underbrace{kr}_{confinement} \tag{37}$$

where $\alpha_S = \frac{g_S^2}{4\pi}$ is the *running coupling constant* for the strong interactions.

The energy required to maintain the separation between quarks eventually exceeds the energy required to produce a pair of quarks: this happens in the limit of large distances ($r \sim 1\,fm = 10^{-15}\,m$), according with Eq. 37. In a process known as hadronization, the force tube 'breaks' and this release of energy creates a quark-antiquark pair which then interact with the separating charges and leave two colour-neutral hadrons.

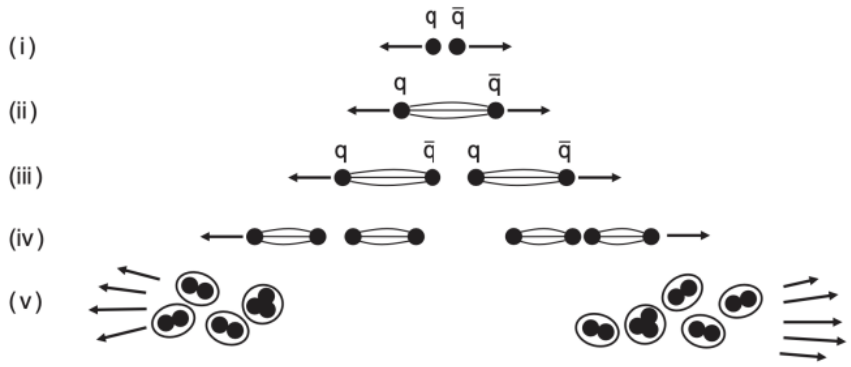

Fig. 5: Schematic multi-step diagram of jet production. The quark-antiquark pair created in a high-energy particle collision undergoes repeated hadronization processes until two jets of particles recoil in the directions of the original quarks' momenta. Figure from [23].

If the two quarks ($q\bar{q}$) are created in a high energy particle collision, then their momenta will be pointing away from each other (in the center of mass frame of reference, see Fig. 5(i)), in a back-to-back configuration. As the two quarks move away from each other, the hadronization process occurs and results in another quark-antiquark pair in between the original. This results in two new flux tubes between the new pair and the original pair (see Fig 5(iii)), however, the new pair are much closer to each other than they are to the original quarks and are therefore attracted to each other as well. As the original quarks continue to separate, the hadronization process repeats, now with the two new flux tubes. This will continue until a sufficient amount of the original quarks' energy has been converted into quark-antiquark pairs, and all the quarks form hadrons. The showering and hadronization processes form collimated sprays of particles, known as jets, moving in the directions of the original quark pairs (see Fig 5(v)).

Asymptotic freedom Along with colour confinement, QCD is characterized by a phenomenon known as *asymptotic freedom*, which states that the strength of the interaction is inversely proportional to the energy transferred. This causes QCD to be strongly coupled at low energy, meaning that the coupling constant, g_S, is of order 1 or larger.

However, this coupling decreases as the energy scale increases (or the distance decreases). Thus, for very short distances (less than the width of a proton), which corresponds to large energies, g_S has a value smaller than 1. Whereas, at large distances (in the context of QCD, larger than the width of a proton) and small energies the value of g_S is much greater than 1. This is different from QED, where the coupling is weak (less than 1) at low energies [14], and grows for high energies.

This change in the coupling strength of g_S is characterized by the QCD confinement scale (Λ_{QCD}), with $\mathcal{O}(\Lambda_{QCD}) \sim \mathcal{O}(m_p)$; at energies below Λ_{QCD}, QCD cannot be studied using perturbation theory, which is the approximation method on which relies upon Feynman diagrams, since it requires the strength of the interactions to be small. Luckily, perturbative QCD can still be used to study high-energy interactions, such as those which takes place at particle colliders.

Valence quarks and sea quarks Analogous to how the outermost (valence) electrons of an atom determine its properties, the quarks that determine a hadron's properties are known as *valence quarks*. So, for instance, a proton is composed by uud and a neutron is made up by udd, in terms of valence quarks.

However, due to gluon interactions, quark-antiquark pairs are constantly being created and annihilated within the hadron. Actually these $q\bar{q}$ pairs do not affect the hadron's quantum numbers, but can engage in the deep inelastic scattering processes of high-energy particle collisions [26].

1.3 Unsolved problems in the Standard Model

At the time of writing, the SM (in the terms of its QCD and EW parts) works perfectly well up to the per-cent level at the highest energies probed so far (13 TeV at LHC) [27]. The experimental frontier has advanced into the TeV range, thanks in particular to the *Tevatron* at Fermilab, Chicago, and to the *Large Hadron Collider* at CERN, Geneva, in the last 30 years. With regard to the data collected by these two hadronic colliders, no unambiguous and clear hints of additional structure has been individuated.

[14] Due to the fact that $\alpha_{EM} \ll 1$, QED processes are typically calculated in perturbation theory, at leading order.

Still, it seems evident that the SM does not represent the final particle physics theory. In fact, some critical issues are present in it and are listed below.

- Firstly, the exclusion of gravity [16] from the SM implies that a new framework will be required at the reduced Planck scale $m_P = (8\pi G_{Newton})^{-1/2} = 2.4 \cdot 10^{18}\,\mathrm{GeV}$, where quantum gravitational effects must become important. It seems nearly as obvious that new physics exists in the 16 orders of magnitude in terms of energy between the presently explored territory near the electroweak scale, provided by the W-boson mass m_W, and the Planck scale, m_P.

- Electroweak and strong forces do not unify in SM. This means that the two interactions, in SM framework, does not appear as different manifestations of the same, underlying interaction.

- All the SM electroweak sector has been investigated by a wide variety of precision studies at particle colliders, in particular at the Large Electron-Positron collider at CERN [28]. The measurements of some EW observables are in tension with SM predictions. The most significant deviation is the one related to the forward-backward asymmetry for the bottom quarks. To that purpose, a complete discussion is reported in Section 2.2.

- The SM cannot explain the number of fermion generations or their large mass hierarchy. The ratio between up quark and top quark masses is:

$$\frac{m_u}{m_t} \simeq \frac{3 \cdot 10^{-3}\,\mathrm{GeV}}{173\,\mathrm{GeV}} \sim 10^{-5}, \tag{38}$$

  with both u and t being elementary particles.

- The SM does not solve the problem of the matter-antimatter asymmetry. The dominance of the matter on the antimatter in Nature, is not explained in the SM, since particles and antiparticles, which have opposite quantum numbers, are formally identical under the Dirac Equation. In some BSM theories, the original matter-antimatter symmetry present in the Universe is supposed to have been broken in a certain point in the past.

- The SM present also the so-called *hierarchy problem*, which is not really a difficulty with the SM itself, but rather a disturbing sensitivity of the Higgs potential to new physics in almost any imaginable extension of the SM. Consider the various terms which appear in the definition of the Higgs mass squared:

$$m_H^2 = (125\,\mathrm{GeV})^2 = m_{H,\mathrm{tree}}^2 + \delta m_{H,\mathrm{top}}^2 + \delta m_{H,\mathrm{gauge}}^2 + \delta m_{H,\mathrm{Higgs}}^2 \tag{39}$$

where the top quark gives the greatest contribute among all the fermions, due to its mass. The various terms are much bigger (at least on TeV scale) than the effective, final value $m_H \sim 100\,\text{GeV}$. So the free term $m^2_{H,\text{tree}}$ needs to be unnaturally fine-tuned to cancel out those huge corrections;

- The SM does not provide the explanation of the nature of the *dark matter*, whose existence is required in order to describe the galaxy clusters which populate the Universe.

These problems, actually, are still unsolved at the state of art, and some of them can eventually be solved with the introduction of new particles at TeV scale, therefore extending the SM to physics beyond-the-SM (BSM). Nowadays there are many separate classes of BSM models that predict different new particles and interactions, for instance the so-called theory of Supersymmetry (SUSY) [29].

Chapter 2

2 Asymmetries at Z-pole

2.1 Asymmetries and coupling constants

A distinct feature of electroweak neutral interactions is the difference between right-handed and left-handed currents. This difference is governed by the Weinberg EW mixing angle $\sin^2\theta_W$, which enters the coupling of the Z-boson to left-handed and right-handed fermions [30]. The different behaviour of the Z-boson when interacting with fermions of opposite chirality has a direct consequence on experimental data, causing measurable asymmetries that can be used to determine $\sin^2\theta_W$ and, using information from the Z-boson partial widths, the couplings themselves [23].

Let's consider a first example, in which a polarized electron beam collides with unpolarized positrons at a center-of-mass energy equal to m_Z to produce an electron-positron pair in the final state; this example can be eventually extended to other leptonic families. In this example, the total cross section will be different, and much higher, if left-handed polarization is used. The relative difference between the two cross sections (σ_L or σ_R) defines the *left-right asymmetry* (A_{LR}), which at leading order can be related to the left-handed (g_{Le}) and right-handed (g_{Re}) electron couplings as follows:

$$A_{LR} = \frac{\sigma_{e_L^-} - \sigma_{e_R^-}}{\sigma_{e_L^-} + \sigma_{e_R^-}} = \frac{g_{Le}^2 - g_{Re}^2}{g_{Le}^2 + g_{Re}^2} \equiv \mathcal{A}_e \tag{40}$$

Since $g_L = \frac{g_{Ve}+g_{Ae}}{2}$ and $g_R = \frac{g_{Ve}-g_{Ae}}{2}$, it can be seen that $\mathcal{A}_e$ depends on the ratio between vector coupling (g_{Ve}) and axial coupling (g_{Ae}) constants of the electron:

$$\mathcal{A}_e = \frac{2g_{Ve}g_{Ae}}{(g_{Ve})^2 + (g_{Ae})^2} = \frac{2g_{Ve}/g_{Ae}}{1 + (g_{Ve}/g_{Ae})^2} \tag{41}$$

The ratio of leptonic couplings $\frac{g_{Vl}}{g_{Al}}$, where l stands for a generic lepton, is used for the operative definition of $\sin^2\theta_{W,eff}$, the *effective* electroweak mixing angle:

$$\sin^2\theta_{W,eff} \equiv \frac{1}{4}\left(1 - \frac{g_{Vl}}{g_{Al}}\right) \tag{42}$$

If the reaction $e^+e^- \to f\bar{f}$ occurs at a center-of-mass energy equal to the Z-boson mass, then it is possible to produce an *on-shell* Z-boson.

In the reaction $e^+e^- \to Z \to f\bar{f}$, where f indicates a generic fermion, the same

effect causes the Z-boson to be partially polarized along the direction of the beams. Indeed, because of angular momentum conservation, left-handed (right-handed) electrons interact with opposite-helicity positrons only; the parity violation causes different cross sections of the two processes and a net Z-boson polarization opposite to the direction of the electron beam. The amount of polarization is exactly $\mathcal{A}_e$ [30].

The Z polarization, and therefore the coefficient $\mathcal{A}_e$, can be measured by analysing the polarization of the outgoing fermion since, once again, angular momentum conservation relates the two quantities. In practice, this is possible only if the emitted fermion is a tau lepton, by measuring the tauon polarization in $e^+e^- \to Z \to \tau\bar{\tau}$.

Alternatively, from an experimental point of view, a physicist can take advantage of parity violation in the Z-boson decay, causing the emitted anti-fermion ($\bar{f}$) being directed preferentially along the direction of the Z-boson spin, while the fermion (f) in the opposite direction. This effect originates a *forward-backward asymmetry* of the fermion emission with respect to the initial electron beam. The forward-backward asymmetry is defined as:

$$A_{FB} = \frac{\sigma_F - \sigma_B}{\sigma_F + \sigma_B} \tag{43}$$

where σ_F is the cross section for fermions which are emitted in the hemisphere centered along the direction of the electron beam, while σ_B refers to fermions in the opposite hemisphere [30]. In general, the total forward and backward cross sections can be formally written in terms of differential angular cross sections:

$$\sigma_F = \int_0^1 \frac{d\sigma}{d\cos\theta}\, d\cos\theta, \quad \sigma_B = \int_{-1}^0 \frac{d\sigma}{d\cos\theta}\, d\cos\theta \tag{44}$$

where θ is the scattering angle between the directions of the incoming fermion (in this case, the electron) and outgoing fermion f. At leading order, the relationship between the forward-backward asymmetry coefficient A_{FB} and the couplings in a transition from electron-positron to fermion-antifermion pair is given by:

$$A_{FB}^f = \frac{3}{4}\mathcal{A}_e\mathcal{A}_f \tag{45}$$

as it can be seen by integrating over the forward and backward hemispheres the $e^+e^- \to Z \to f\bar{f}$ differential cross section.

2.2 Forward-backward asymmetries

The measurement of forward-backward asymmetries, introduced in Eq. 43, requires the identification of the charge of the fermion and the measurement of its direction.

A_{FB} has been measured for individual lepton species (e, μ, τ) [31], for heavy quarks (c and b) and inclusively for hadrons [32]. Assuming lepton universality (see Section 1.1.1), the ratios of the couplings of the Z-boson to charged leptons are equal; therefore the asymmetries involving leptons provide a direct determination of the effective mixing angle $\theta_{W,eff}$ (Eq. 42) using the relation $A_{FB}^f = \frac{3}{4}\mathcal{A}_e\mathcal{A}_f$ (Eq. 45), where the fermion f in this case represents the final state lepton. The quark forward-backward asymmetries depends on $\mathcal{A}_f = \frac{2g_{Vq}/g_{Aq}}{1+(g_{Vq}/g_{Aq})^2}$ where the subscript q indicates the quark flavor. [15] The ratio of quark couplings can be expressed in terms of $\sin^2\theta_{W,eff}$ and non-universal corrections as follows [33]:

$$\frac{g_{vq}}{g_{Aq}} = 1 - \frac{2Q_q}{I_{3L,q}}\left(\sin^2\theta_{W,eff} + C_q\right) \tag{46}$$

The residual vertex correction C_q can be computed assuming the validity of the SM. In particular, for u, d, c, s quarks it is small and presents very little dependence on the parameters of the model itself, while for b it depends strongly on the top quark mass because of the presence of additional $Z \to b\bar{b}$ vertex corrections [30]. It amounts to $+0.0014$ for a top quark mass of $m_t \simeq 173\,\text{GeV}$.

In case of quarks the term $\mathcal{A}_f$ is large and is weakly dependent on $\sin^2\theta_{W,eff}$, leaving most of the dependence on the weak mixing angle to $\mathcal{A}_e$. It follows that for the quark sector of the SM, A_{FB} is essentially linear dependent on $\sin^2\theta_{W,eff}$, while for leptons it shows a quadratic dependence:

$$A_{FB}^l(q^2 = m_Z^2) = \frac{3}{4}\mathcal{A}_l^2 + \text{"small QED extra terms"}. \tag{47}$$

The consequence of this behaviour is shown in Tab. 3, where the magnitude of A_{FB} and its sensitivity to $\sin^2\theta_{W,eff}$ is given by leptons, for u-type and d-type quarks.

Observable O	Fermion species	Value	$\frac{\partial O}{\partial \sin^2\theta_{W,eff}}$
A_{FB}	leptons	0.02	-1.7
	u, c quarks	0.07	-4.0
	d, s, b quarks	0.10	-5.6
A_{LR}	leptons	0.15	-7.8

Tab. 3: Magnitude of A_{FB} and its sensitivity on $\sin^2\theta_{W,eff}$ for various fermion species at the Z-pole. The value of $\sin^2\theta_{W,eff} = 0.2316$ is used for the electroweak mixing angle. For comparison, the last line of the table gives the magnitude and the sensitivity to A_{LR}.

Formally, the forward-backward asymmetry can be determined by measuring the

[15] To avoid confusion, it is specified that q refers to the quark *flavor*, while e in Eq. 41 indicates the electron, which is one of the lepton flavors.

cross section in the forward and backward hemispheres, where these two directions are defined with respect to the original fermion beam, i.e. with respect to the incoming electrons in the case of leptonic e^+e^- colliders; then $A_{FB} = \frac{\sigma_F - \sigma_B}{\sigma_F + \sigma_B}$ (Eq. 43) can be directly computed. Alternatively, it can be extracted by fitting the experimental data on the differential angular distribution:

$$\frac{dN}{d(\cos\theta)} = C(\cos\theta) \cdot \left(\cos^2\theta + \frac{8}{3} A_{FB} \cos\theta + 1 \right) \tag{48}$$

where θ is the scattering polar angle of the fermion in the center-of-mass frame and $C(\cos\theta)$ is an acceptance function modifying the differential cross section.

The measurements can be split in two classes:

- measurements where the selection of both fermions is required, as for the leptonic asymmetries;
- measurements where at least one fermion must be tagged, as for the measurements of heavy quark asymmetries.

In both cases the acceptance is a symmetric function, provided the selection efficiency is charge- or forward-backward symmetric. In fact, this peculiarity is evident if $F(\cos\theta)$ is defined as the efficiency to detect a fermion at a certain scattering polar angle θ. If the efficiency is symmetric with respect to the charge, then the same function, F, gives the efficiency for anti-fermions. Hence for the first class of measurements one has $C(\cos\theta) = F(\cos\theta)F(-\cos\theta) = C(-\cos\theta)$; similarly for the second class $C(\cos\theta) = F(\cos\theta) + F(-\cos\theta) = C(-\cos\theta)$. Similar arguments hold for forward-backward symmetric efficiency.

The symmetry of the acceptance $\cos\theta$ has some important consequences. Firstly, in the $(\cos\theta)$-dependent forward-backward asymmetry, defined as

$$A_{FB}(\cos\theta) = \frac{\frac{dN}{d\cos\theta}(\cos\theta) - \frac{dN}{d\cos\theta}(-\cos\theta)}{\frac{dN}{d\cos\theta}(\cos\theta) + \frac{dN}{d\cos\theta}(-\cos\theta)} = \frac{8}{3} A_{FB} \frac{\cos\theta}{(1+\cos\theta)^2} \tag{49}$$

the $C(\cos\theta)$ acceptance cancels out, showing that it is possible to make a measurement which is independent on the acceptance by exploiting the differential angular distribution. This is an important advantage over the simple counting of forward and backward events, because it makes the measurement insensitive to most instrumental effects, under the assumption of a given angular behaviour.

Another advantage is a more accurate determination of A_{FB} since the whole angular distribution is used, and more weight is given to the most sensitive angular

regions. It is convenient to take advantage of these properties by using an unbinned log-likelihood method to fit the data. If $\mathcal{L}_i = \prod_i \mathcal{P}_i$ is the likelihood function defined as product of event probabilities $\mathcal{P}_i$ and the product is extended to all events, the negative log-likelihood can be written as:

$$\begin{aligned} -\ln\mathcal{L} &= -\sum_i \ln\mathcal{P}_i \\ &= -\sum_i \ln\left[\frac{3}{8}C(\cos\theta)\cdot\left(1+\cos^2\theta_i+\frac{8}{3}A_{FB}\cos\theta_i\right)\right] + \text{const.} \\ &= -\sum_i \ln\frac{3}{8}C(\cos\theta) - \sum_i \ln\left(1+\cos^2\theta_i+\frac{8}{3}\cos\theta_i\right) + \text{const.}. \end{aligned} \tag{50}$$

This relation is derived from Eq. 48. The value of the A_{FB} parameter giving the maximum likelihood does not depend on the angular correction, therefore the first term in Eq. 51 can be ignored in the data analysis.

The energy dependence of the forward-backward asymmetry near the Z-peak, caused by the interference between the photon and the Z-boson exchange, depends on the electric charge of the final fermion and on its axial coupling, and has very little dependence on other electroweak parameters. This dependence from center-of-mass energy s around the Z-peak in $e^+e^- \to f\bar{f}$ can be written as:

$$A_{FB}^f(s) \simeq A_{FB}^f(m_Z^2) + \frac{s-m_Z^2}{s}\frac{3\pi\alpha(s)}{\sqrt{2}G_F m_Z^2}\frac{2Q_eQ_f g_{Ae}g_{Af}}{(g_{Ve}^2+g_{Ae}^2)(g_{Vf}^2+g_{Af}^2)} \tag{51}$$

where α and G_F are the QED running coupling constant and Fermi constant for the electroweak interactions, while Q_e and Q_f indicate the charges of the incoming electron and outgoing fermion, respectively. When the measurement of the forward-backward asymmetry is performed exactly at a center-of-mass energy equal to m_Z, the superscript "0" is added to the writing A_{FB}. The dependence of A_{FB} from s is maximal for leptons ($\Delta A_{FB}^l/\Delta E_{CM} \simeq 0.00009\,\text{MeV}$), while the down-type quarks (d, s, b) show the smallest energy dependence [30]. At LEP, this effect is corrected for using the precise energy determination of the beam energy, by running the measured asymmetry to m_Z. All forward-backward asymmetries are also corrected for the effect of initial state radiation, for imaginary parts of the couplings, for the effect of pure photon exchange and the presence of box diagrams. Specific corrections can be also applied for final state photon radiation (leptons) and gluon emission (hadrons). The total uncertainty is mainly given by the statistical contribution for all measurements at LEP.

2.3 Lepton forward-backward asymmetry

Among all the possible processes which give a fermion-antifermion pair in the final state, it is possible to select $e^+e^- \to Z/\gamma \to l\bar{l}$ events at LEP. The forward-backward asymmetry is determined by fitting the data according to Eq. 48; the observable θ is defined by the scattering (polar) angle of the final-state negative lepton. In the cases of electron and muon, the assignment of the polar angle is trivial, with a sensitivity strictly related to the resolution of the tracker and, eventually, the EM calorimeter (see Section 4). On the other hand, for tau leptons, which can both decay in lighter leptons or hadrons, the direction is given by the sum of the momenta of charged particles associated to the tau decays; the tau charge is measured in the same way.

In the case of e^+e^- final state, the t-channel photon-exchange process induces an important asymmetric correction and requires a careful treatment. The contribution of this process is taken into account subtracting it from the measured angular distribution. Semi-analytical calculations incorporating leading-log photonic corrections, first-order non-log terms and first-order weak corrections are available [34] and are used for this correction. The t-channel influence is reduced by analysing the data in a restricted angular region, typically in the $-0.9 \leq \cos\theta \leq +0.7$ range. Within this range the t-channel contributes 12% to the total cross section, therefore calculations with 1% precision yield an uncertainty of 0.1%. In the fit of the subtracted data to the form given by Eq. 48 an extended maximum-likelihood procedure is used, where the overall normalization is a free parameter of the fit.

The scattering angle of the final leptons in the laboratory system is affected by initial- and final-state radiation (called ISR and FSR); the main effect is due to hard collinear radiation from one of the initial state leptons. The latter can be corrected for by using the scattering angle in the effective center-of-mass system, that is

$$\cos\theta^* = \frac{\cos\left[\frac{1}{2}(\theta_{l^-} - \theta_{l^+} + \pi)\right]}{\cos\left[\frac{1}{2}(\theta_{l^-} + \theta_{l^+} + \pi)\right]} \tag{52}$$

where θ_{l^-} and θ_{l^+} are the scattering angles of the lepton and anti-lepton respectively, and π stands for the flat angle in radians. In practice, since initial state radiation (ISR) is forward-backward symmetric, the use of Eq. 52 is not strictly required, but it simplifies, however, the definition of the acceptance, particularly for the e^+e^- final state. ISR affects the observed asymmetry for another reason: the steep dependence of the asymmetry on $\sqrt{s}$ (Eq. 51)), changes the effective center-of-mass and therefore the observed asymmetry itself. As photons produced in final-state radiation (FSR) are not used in the definition of the scattering angle, their effect is a small reduction

of the observed asymmetry. Semi-analytical programs can be used to correct for final-state photon emission [35].

The asymmetries A^l_{FB} (where $l = e, \mu, \tau$) measured at LEP [36] are extracted from a fit to the measured $A_{FB}(s)$ using data collected near the Z-peak and at the off-peak points used to measure the Z lineshape. It has been already stressed that, since the vector couplings of the leptons are small, the slope of $A^l_{FB}(s)$ as a function of the beam energy is mainly sensitive to the axial couplings. The fitting formula takes into account the energy dependence of the asymmetry and the fit is done simultaneously with the lineshape data to account for the effect of the energy uncertainty. In the simultaneous fit of the lineshape data and $A^l_{FB}(s)$ the axial couplings are essentially determined by the lineshape and they are used to transport the off-peak measurements of $A^l_{FB}(s)$ to $\sqrt{s} = m_Z$. In an alternative method [37], [38], the slope of the asymmetry is described by a free parameter. This different approach allows to check the consistency in the determination of the axial couplings between the lineshape and the forward-backward asymmetries.

The measurement of $A^{0,l}_{FB}$ (where l indicates the lepton and "0" indicates $\sqrt{s} = m_Z$) is a rather straightforward measurement and has low systematic uncertainties. For the μ and τ channels the systematic uncertainties are related to the applied corrections, to the presence of background and to possible detector asymmetries. Typical systematic errors quoted by the LEP experiments are of the order of $\Delta A^{\rm syst}_{FB} = 0.0005 \div 0.001$ for muons and $\Delta A^{\rm syst}_{FB} = 0.001 \div 0.003$ for tauons, depending of the experiment. For electrons, the theoretical uncertainty introduced in the treatment of the t-channel terms (~ 0.0014) has to be taken into account, thus the typical error is increased to $\Delta A^{\rm syst}_{FB} \sim 0.002$. Moreover, the uncertainty on the center-of-mass energies gives a contribution of $\Delta A^{0,l}_{FB} = 0.0004$, comparable to the experimental systematics. This last two uncertainties are common to the four experiments and have to be treated in a correlated way when averaging the measurements.

The combination of the results of the four LEP experiments (see Section 3.3 for details) gives:

$$A^{0,e}_{FB} = 0.0145 \pm 0.0025 \tag{53}$$

$$A^{0,\mu}_{FB} = 0.0169 \pm 0.0013 \tag{54}$$

$$A^{0,\tau}_{FB} = 0.0188 \pm 0.0017 \tag{55}$$

These measurements can be used to determine the ratios $\frac{g_{V,l}}{g_{A,l}}$ for the three charged leptons up to a common sign. The three measurements can be combined assuming

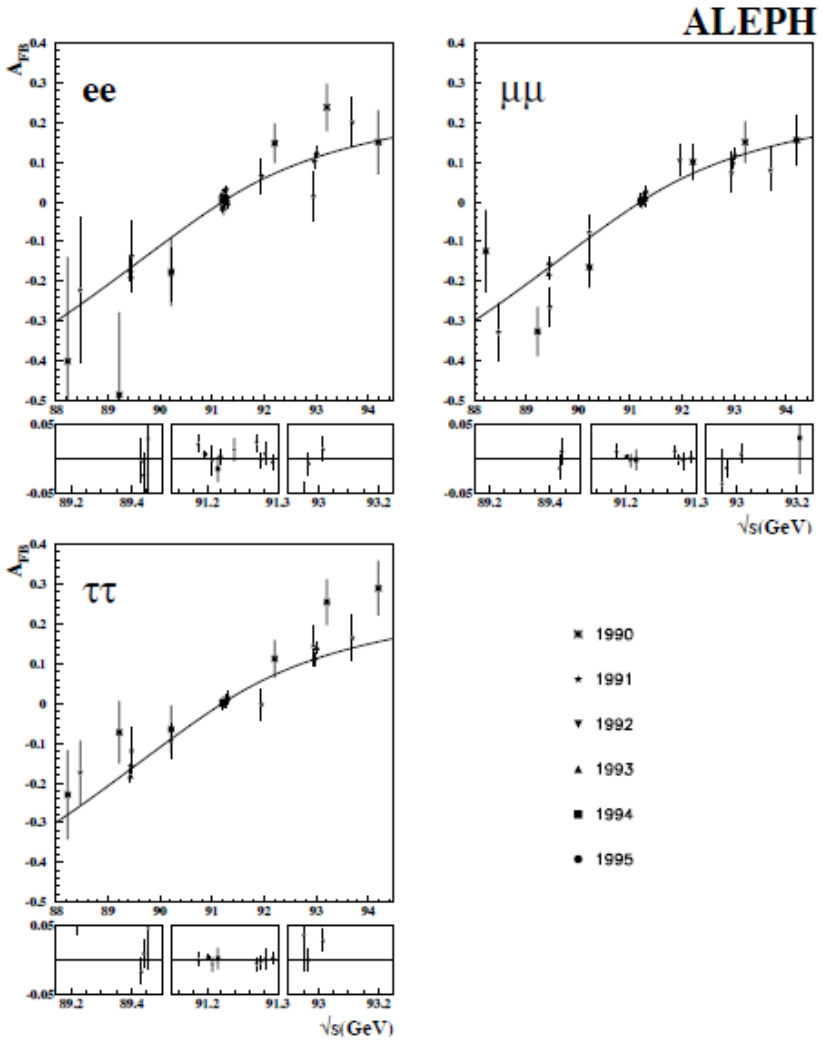

Fig. 6: Measurement of the forward-backward asymmetries for the three lepton generations at various center-of-mass energies, employed by ALEPH collaboration at LEP. [30]

lepton universality, giving:

$$A_{FB}^{0,l} = 0.0171 \pm 0.0010 \tag{56}$$

By converting this result, the value of the effective EW mixing angle can be extracted:

$$\sin^2 \theta_{W,eff} = 0.23099 \pm 0.00053. \tag{57}$$

The dependence of the lepton asymmetries $A_{FB}^{l}(s)$ on the center-of-mass energy $\sqrt{s}$, is consistent with the expected behaviour, value and sign of the lepton axial couplings and it is shown in Fig 6.

2.4 Heavy quark asymmetries

2.4.1 General properties of hadronic events at Z pole

Hadronic events around the Z peak are generally characterized by high particle multiplicity at the Z resonance on average about twenty charged particles per event are produced (Fig. 7), accompanied by a similar number of neutral particles.

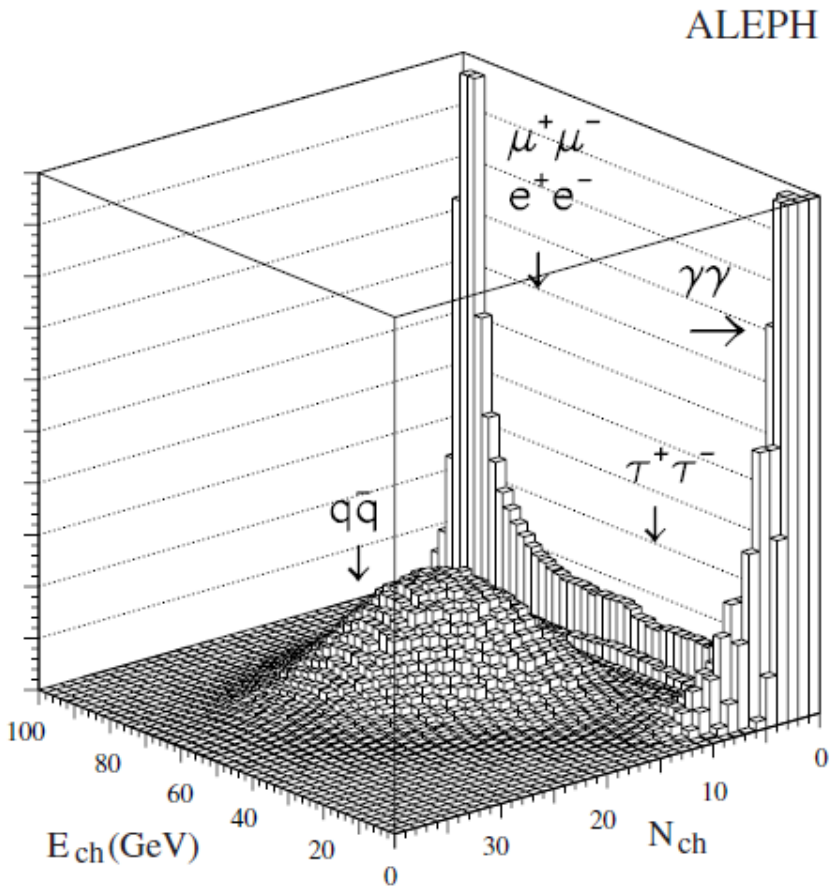

Fig. 7: The sum of charged track energies versus the track multiplicity, for various final states at center-of-mass energies around the Z peak, collected by ALEPH collaboration at LEP. [30]

Since the Z-boson is considerably heavier than quarks, final state particles tend to be relatively collimated around a specific axis, as shown in the event represented in Fig. 8. The main axis of the event can be evaluated as the direction of the unit vector $\hat{n}$ that maximises the *thrust* T:

$$T = \frac{\sum_i |\vec{p}_i \cdot \hat{n}|}{\sum_i |\vec{p}_i|} \tag{58}$$

where $\vec{p}_i$ stands for the momentum of particle i and the sum is calculated over all

the reconstructed particles in the event. In this way, the thrust axis behaves as an estimator of the quark-antiquark flight direction: a plane perpendicular to the thrust axis and containing the interaction vertex, which denotes the point where the Z boson is produced, divides the event in two halves, called *hemispheres*, of which one typically contains the quark and the other the antiquark.

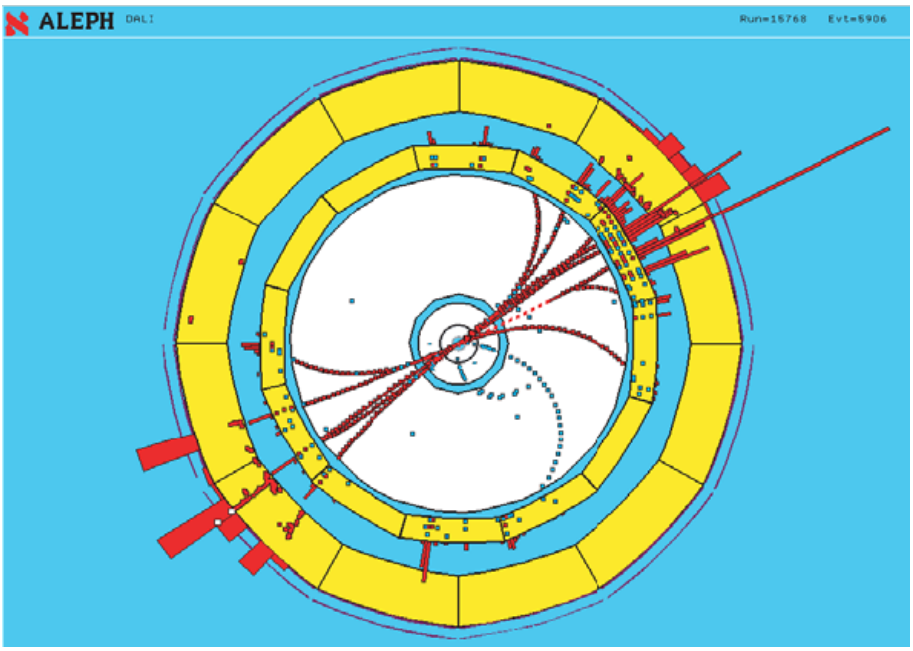

Fig. 8: Display of a Z hadronic decay collected by ALEPH, at LEP (CERN). The reconstructed particles are clustered in two back-to-back jets.

Moreover, emission of hard gluons in hadronic Z decays is a relatively frequent process. Hemispheres containing hard gluons feature broader jets of particles and can show a "multi-jet" structure. The value of T itself ($0.5 \leq T \leq 1$) is an indicator of the presence of hard gluons: broader jets or multi-jet events tend to yield a lower T. A satisfactory definition of jets requires the introduction of jet clustering algorithms. Such algorithms are based on iterative procedures and on the definition of a metric, i.e. a "distance" y_{ij} between particle i and particle j in terms of observable quantities. A widely used metric already developed for EW and QCD studies [39] is related to the invariant mass of the two-particle system:

$$y_{ij} = \frac{2E_iE_j(1-\cos\theta_{ij})}{E_{vis}^2} \tag{59}$$

where E_i, E_j are the particles' energies, θ_{ij} the angle between them and E_{vis} is the energy of all particles used in the event.

The iterative algorithm proceeds as follows: after the computation of the various metrics y_{ij}, the pair of n particles with the smallest value of y_{ij} is replaced by

a pseudo-particle named *jetlet*. The four-momentum of the considered jetlet is recomputed according to a recombination scheme. In a widely used scheme (namely *"E" scheme*), the four momentum of the *jetlet* is simply the sum of the four momenta of the two particles. The clustering procedure is then iterated with $n-1$ objects with the jetlet treated as a new particle. The procedure is repeated until all y_{ij} are larger than a predefined value $y_{\rm cut}$, called *jet resolution parameter*. At the end of the procedure N jets, with definite four-momentum, are overall obtained. The term $E^2_{\rm vis}$ in Eq. 59 simply represents a normalization factor, allowing similar values of $y_{\rm cut}$ to be used when different sets of particles are employed in the event reconstruction. In some of the measurements only charged particles are used, as measured by tracking devices, accounting typically for about 65% of the visible energy at LEP. In most of the final LEP measurements, however, jets were reconstructed using also neutral particles detected from their energy deposits in the calorimeters (Section 4). In this case the visible energy is much closer to the center-of-mass energy. The N-jet rate depends on the chosen value of $y_{\rm cut}$: as an example, for hadronic Z decays $y_{\rm cut} = 0.01$ yields about 65% of two-jet events, about 30% of three-jet events and 5% of events with higher jet multiplicities.

2.4.2 Measurement of heavy quark asymmetries

The measurements of heavy quark [16] asymmetries, such as the forward-backward asymmetries A^b_{FB} and A^c_{FB}, represent an ambitious challenge, due to the complexity in the identification and reconstruction of the jets originated by c and b quarks or by $\bar{c}$, $\bar{b}$ antiquarks. To this purpose, tagging methods based on lifetime seem not to be the best solution, despite their high performance, since they do not provide information about the quark charge. Thus, at LEP inclusive methods have been developed to estimate the charge of the b quark, in order to complement lifetime tags for the measurement of forward-backward asymmetries.

The most challenging experimental issue consists in the determination of the jet electric charge. The jet charge can be defined in several ways. For instance, it can be written as follows:

$$Q_h = \frac{\sum_i q_i p^k_{P,i}}{\sum_i p^k_{P,i}} \tag{60}$$

where $p_{P,i}$ is the momentum of a particle parallel to the thrust axis (defined in Eq. 58), and the sum runs over all charged particles in a hemisphere.

Actually, Eq. 60 does not represent the unique possible definition for jet charge. Alternative definitions can be constructed using the rapidity instead of the projected

[16] As a reminder, the expression "heavy quarks" refers to c and b flavors.

momentum, or using the axis of the leading jet instead of the thrust axis; otherwise, another choice is that of restricting the sum to the particles belonging to the leading jet, as done in this Master Thesis work (Section 5). The parameter k in Eq. 60 can be tuned to obtain high sensitivity to the quark charge, while keeping low correlation between the charge of the two hemispheres: typical values for k are between 0.3 and 1.

In a pure sample of b events, the forward-backward asymmetry is proportional to the mean charge flow between the two hemispheres:

$$Q^b_{FB} \equiv \langle Q^b_F - Q^b_B \rangle = \delta_b A^b_{FB} \tag{61}$$

where the parameter δ_b is called *charge separation*. At parton level δ_q, which is the charge separation for a generic quark q, is equal to twice the quark charge, but hadronization and decays lower its value, diluting the measured charge flow. Thus a precise determination of the forward-backward asymmetry requires an evaluation of δ_q with the lowest possible uncertainty. The advantage of high-purity single-flavour samples, that in practice can be obtained for b quarks only, lies on the possibility of measuring δ_q from the data, lowering considerably the use of theoretical assumptions in the evaluation of this parameter, and therefore lowering its uncertainty. Hemispheres containing the b or $\bar{b}$ quark have average measured charge given by:

$$\langle Q_b \rangle = \frac{\delta_b}{2} + \langle \mathcal{R}_b \rangle \tag{62}$$

$$\langle Q_{\bar{b}} \rangle = -\frac{\delta_{\bar{b}}}{2} - \langle \mathcal{R}_{\bar{b}} \rangle, \tag{63}$$

where $\mathcal{R}_b$ and $\mathcal{R}_{\bar{b}}$ are small corrections which account for interactions with the detector material, that introduce a bias between positively and negatively charged reconstructed particles. The total electric charge measured in the event is $\langle Q^b_{\mathrm{TOT}} \rangle = \langle \mathcal{R}_b - \mathcal{R}_{\bar{b}} \rangle$, which is very close to zero due to the small values assumed by $\mathcal{R}_b$ and $\mathcal{R}_{\bar{b}}$. The product of the two hemisphere charges can be written as:

$$\langle Q^b_F Q^b_B \rangle = \langle Q_b Q_{\bar{b}} \rangle = -\frac{1}{4}\delta_b^2 - \frac{1}{2}\delta_b \big(\langle \mathcal{R}_b \rangle + \langle \mathcal{R}_{\bar{b}} \rangle \big) - \langle \mathcal{R}_b \mathcal{R}_{\bar{b}} \rangle \tag{64}$$

where the last term $\langle \mathcal{R}_b \mathcal{R}_{\bar{b}} \rangle$ takes into account correlations between the charge measurements in the two hemispheres, due to total charge conservation and kinematic correlations between the b hadrons.

The charge separation δ_b can be measured by comparing the widths of the distributions of the charge flow and of the total charge, as demonstrated below

(Eq. 65):

$$\begin{aligned}\sigma^2(Q^b_{FB}) - \sigma^2(Q^b_{\mathrm{TOT}}) &= \langle \left(Q^b_{FB}\right)^2 \rangle - \langle Q^b_{FB} \rangle^2 - \langle \left(Q^b_{\mathrm{TOT}}\right)^2 \rangle + \langle Q^b_{\mathrm{TOT}} \rangle^2 \\ &= -4\langle Q^b_F Q^b_B \rangle - \langle Q^b_{FB} \rangle^2 + \langle Q^b_{\mathrm{TOT}} \rangle^2 \\ &\simeq \delta_q - \langle Q^b_{FB} \rangle^2 + \langle Q^b_{\mathrm{TOT}} \rangle^2 \end{aligned} \tag{65}$$

The last line in Eq. 65 relates δ_b to physical observables, having dropped the corrections for material interactions and hemisphere correlations (introduced above in Eq. 64; in general, in data analysis this corrections are estimated through a simulation. A sketch illustrating the physical meaning of the above quantities is presented in Fig. 9, in order to shed light on their features.

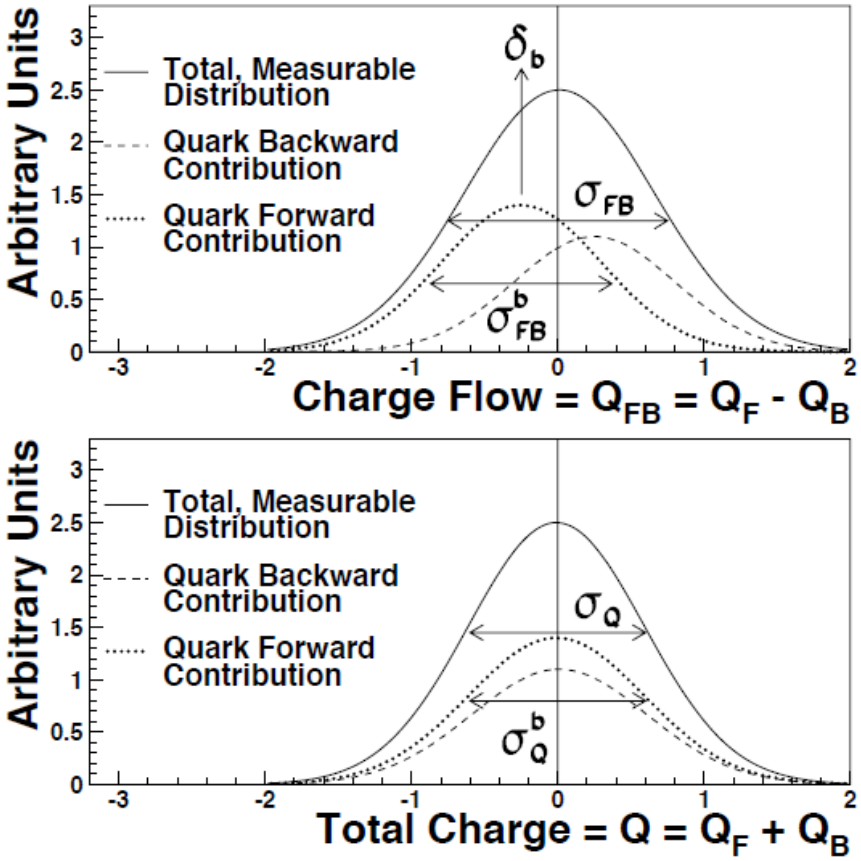

Fig. 9: Sketch showing the distributions of charge flow and total charge: the difference in width between the two distribution is related to the charge separation, as explained in Eqs. 64 and 65.

Although a separation among the different flavours in hadronic events near to Z pole is theoretically achievable, in general pure b samples cannot be selected in an asymmetry analysis. Therefore, the above formalism has to be developed taking into account also the contributions of the other flavors, both the light (u, d, s) and heavy

(c) quarks [17]; for instance, the charge flow can be rewritten as

$$Q_{FB} = f_b \delta_b A^b_{FB} + f_c \delta_c A^c_{FB} + f_{uds} \delta_{uds} A^{uds}_{FB} \tag{66}$$

where f_b, f_c, f_{uds} are the fraction of b, c and light quark events in the selected sample, and light quarks have been, as usual, treated as a single class.

In a simplified approach, the sample composition as well as the charm and light quark charge separations can be estimated with the simulation; δ_b can be extracted from the data (using the simulation to subtract the non-b contributions and correct for hemisphere correlations) and the b asymmetry can be derived from the observed charge flow.

In the more sophisticated approaches single or double tagging techniques can be used to derive most parameters from data. The measurement of the forward-backward asymmetry related to bottom quarks using these techniques is affected by systematic uncertainties much smaller than the statistical error obtained at LEP.

Measurement of jet charge asymmetry using all flavors As already mentioned above, direct measurements of the charge separation for non-b quark flavours require great efforts. Nevertheless charm samples selected by requiring the presence of a D^* meson can be employed to evaluate the parameter δ_c (in Eq. 66) with moderate model-dependence. Lifetime-tagged samples with varying charm content can also be examined to infer the value of δ_c. The charm charge separation is reduced by the presence of the soft pion in the D^* decay. The soft pion retains memory of the original charm charge, but being low momentum it gets a low weight from the jet charge definition (Eq. 60). Individual charge separations for lighter quarks cannot be measured separately, however the average δ_{uds} can be inferred from the difference in width of the $\langle Q_F - Q_B \rangle$ and $\langle Q_F + Q_B \rangle$ and distributions, by a procedure similar to the one based on Eq. 65. When b-tagging is not used, Eq. 66 can be rewritten as:

$$Q_{FB} = C \sum_q \delta_q A^q_{FB} \frac{\Gamma_{q\bar{q}}}{\Gamma_{\rm had}} = C \frac{3}{4} \sum_q \delta_q \mathcal{A}_e \mathcal{A}_q \frac{\Gamma_{q\bar{q}}}{\Gamma_{\rm had}} \tag{67}$$

with $q = u, d, c, s, b$. Here (Eq. 67) C indicates the geometrical acceptance and $\mathcal{A}_q$, $\mathcal{A}_e$ are the left-right asymmetry parameters for the quark and the incoming electron already introduced in Section 2.1; $\Gamma_{q\bar{q}}$ and $\Gamma_{\rm had}$ indicate the widths for $q\bar{q}$ and all hadronic events. Clearly, this relation shows a linear dependence on $\mathcal{A}_e = \frac{2 g_{Ve}/g_{Ae}}{1+(g_{Ve}/g_{Ae})^2}$ and, through this parameter, Eq. 67 can be used to extract the electroweak mixing

[17] In charge flow calculation, top quark is not considered, due to the fact that it immediately decays and does not hadronize through a jet.

angle $\sin^2\theta_{W,eff}$. As the coefficients $\mathcal{A}_q$ are only weakly dependent from $\sin^2\theta_{W,eff}$, then their expected value can be used, and the same is done for the ratio $\frac{\Gamma_{q\bar{q}}}{\Gamma_{\rm had}}$.

The electroweak mixing angle $\sin^2\theta_{W,eff}$ determined from Q_{FB} using untagged hadronic samples is dominated by the systematic uncertanties on the charge separations, given by the δ_q's. In particular detailed Monte Carlo studies are needed to disentangle the δ_u, δ_d and δ_s contributions; eventually the simulation has to be carefully tuned to the measured kaon (K) and hyperon (Λ) production rates in order to have a realistic description of strangeness production.

2.5 Heavy quark asymmetries: LEP combined results and QCD corrections

The LEP measurements of b and c forward-backward asymmetries from semileptonic events, from inclusive samples and from D mesons [40] can be combined to merge the experimental information in an optimal way. The combination procedure follows a χ^2 minimisation and it is described in detail in [41]. Some measurements depend on parameters determined analysing the same data, for example the semileptonic events used to measure the b and c asymmetries provide also information on the b semileptonic branching ratios or on $B\bar{B}$ oscillations. These ancillary measurements must be taken into account in the combination. The covariance matrix used in the fit includes the statistical and systematic correlation among various measurements. Statistical correlations exist for measurements performed with the data collected by the same experiment. On the other hand, measurements of the same parameter by different experiments are affect by common systematic uncertainties.

As introduced in Section 2.2, the extraction of the effective electroweak mixing angle requires the identification of the b and eventually c directions, and as a consequence requires the evaluation of the corrected asymmetries $A_{FB}^{0,b}$ and $A_{FB}^{0,c}$, from the measured asymmetries. Heavy quark asymmetries are affected by radiative effects due to strong interactions, which are related to virtual vertex and gluon bremsstrahlung diagrams that modify the angular distribution of the fermions emitted in the final state. The emission of an hard gluon, for instance, may scatter both b and $\bar{b}$ in the same hemisphere (forward or backward): in such events the original electroweak asymmetry is destroyed. The effect of such radiative effects is to lower the experimentally observed asymmetry by a few percent. However, detailed calculation based on perturbative QCD, including second-order corrections for massless quarks and quark mass effects at first-order, have been developed in the past decades and are available today [88].

An important ingredient of these theoretical calculations is the definition of the b

quark direction, which should closely match the experimental definition based on jet charge reconstruction methods, such as thrust axis reconstruction. In practice experimental cuts reduce considerably the QCD corrections [43]. For instance the momentum cut which is applied in lepton tagging selects events with reduced gluon radiation. Furthermore in some cases the effect of hard gluon radiation is automatically incorporated by analysis procedure. This is the case for the inclusive measurements based on jet charge techniques, because the b charge separation, measured with data, is an effective parameter that includes the QCD smearing.

At the state of art, the present world averages for the b and c forward-backward asymmetries at the Z pole, as given in [28], are:

$$A_{FB}^{0,b} = 0.0992 \pm 0.0016 \tag{68}$$

$$A_{FB}^{0,c} = 0.0707 \pm 0.0035 \tag{69}$$

with a +15% correlation between the two results. Both these LEP results are dominated by statistical uncertainties: in particular, for the b asymmetry, the systematic uncertainties related to the QCD corrections is a factor three lower than the statistical error.

The dependence of the b and c asymmetries on the center-of-mass energy, A_{FB}^{b} and A_{FB}^{c}, is regulated by the quark electric charge and its axial coupling (Eq. 51). Their observed energy dependence is shown in Fig. 8.10 and compared to the MSM [18] prediction. The value of $\sin^2\theta_{W,eff}$ given in [30] is used to normalize the vertical scale for the MSM prediction. The different slope for b and c quarks is due to the absolute value of their electric charge, that in the case of bottom flavour (down-type quarks) is twice larger than up-type quarks. The asymmetry is increasing in both cases because the two quark types have opposite sign (and same absolute value) for the axial couplings.

2.6 Interpretations of asymmetry measurements at LEP

The measurements of the asymmetries presented in Sections 2, 2.2 and 2.3 can be interpreted as a measurement of $\sin^2\theta_{W,eff}$. For the leptonic forward-backward asymmetries, for the measurements of $\mathcal{A}_e$ and $\mathcal{A}_\tau$ from tau polarization, and for the measurement of A_{LR}^0 the interpretation requires the only assumption of lepton universality. The derivation of $\sin^2\theta_{W,eff}$ from hadronic measurements requires the knowledge of the $\mathcal{A}_q$ terms that, as already discussed, have only a mild dependence

[18] Remember that the acronym "MSM" indicates the Minimal Standard Model, as introduced in Section 1.

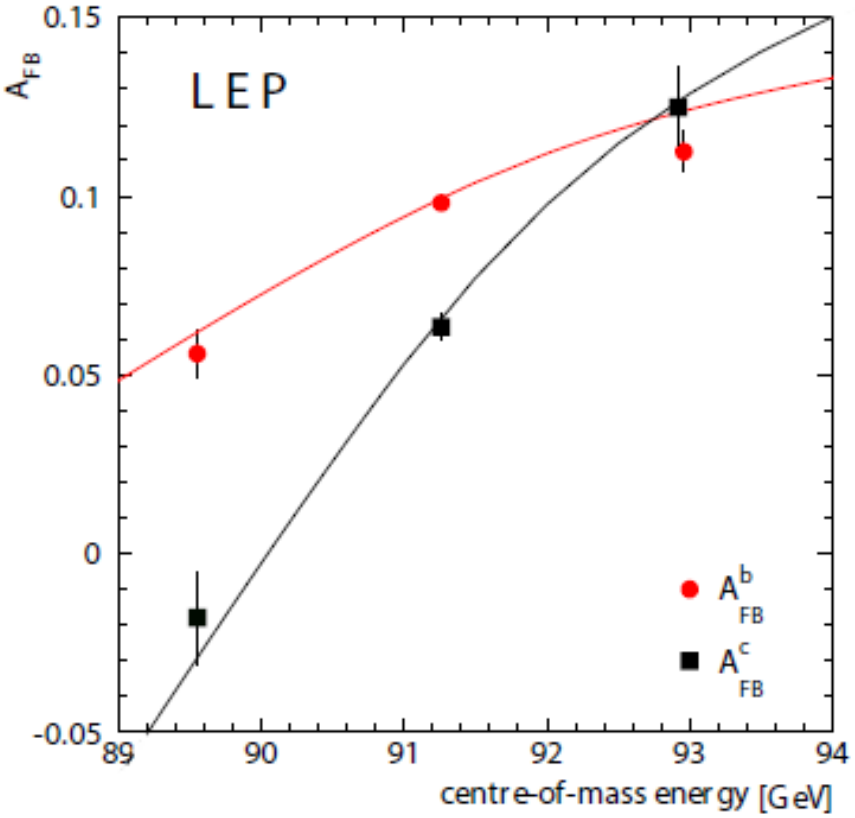

Fig. 10: Measurement of the b and c forward-backward asymmetries as a function of the center-of-mass energy. The MSM expectation for the two quark types is shown. (Courtesy of the LEP Electroweak Working Group [28].)

on the sine of the EW mixing angle, in the Standard Model. For this class of measurements the validity of the SM, at least in his minimal version 1, for the $\mathcal{A}_q$ terms is assumed; this assumption is corroborated by the direct measurements of $\mathcal{A}_b$, $\mathcal{A}_c$ using polarized beams, which agree with the MSM.

A compilation of the various results is shown in Fig. 11, where the dependence of $\sin^2\theta_{W,eff}$ on the Higgs boson mass, not yet know at that time [30], is also indicated. The six results shown in the figure are obtained, respectively, from the lepton forward-backward asymmetry, the tau polarization, the left-right asymmetry, the b forward-backward asymmetry, the c forward-backward asymmetry and the jet charge asymmetry using all quark flavours. The average of the six measurements gives:

$$\sin^2\theta_{W,eff} = 0.23153 \pm 0.00016 \tag{70}$$

with a χ^2 of 11.8 for five degrees of freedom corresponding to a confidence level of 3.7%. This confidence level is relatively low, because the most precise determinations, based on A^0_{LR} and on the $A^{0,b}_{FB}$ asymmetry are about 3σ apart [28].

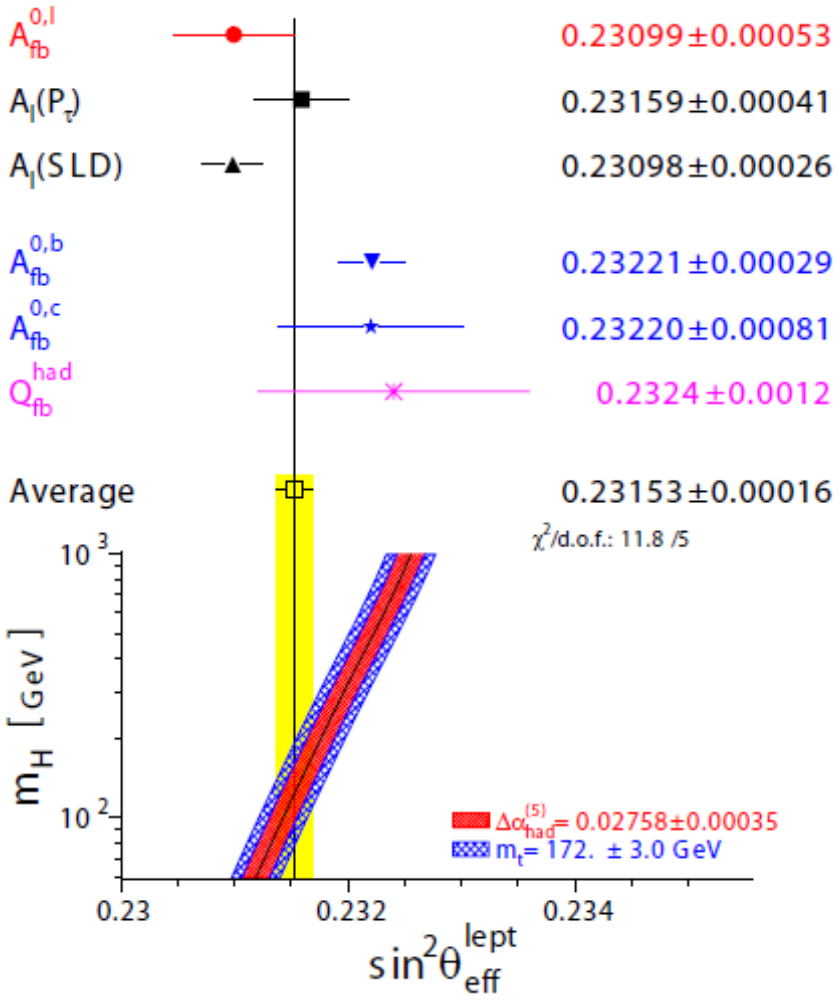

Fig. 11: The determinations of $\sin^2\theta_{W,eff}$ from the measurements introduced in this Section and their average. The measurements are shown, starting from the top, in the following order: the lepton forward-backward asymmetry; the tau polarization; the left-right asymmetry; the b forward-backward asymmetry; the c forward-backward asymmetry; the jet charge asymmetry using all quark flavours. The results are compared to the MSM prediction, as a function of the Higgs boson mass. The uncertainty due to $\alpha(m_Z^2)$ on the MSM predictions is indicate by a band. The effect of varying the top mass within the range indicated in the figure is added as two extra side bands. (Courtesy of the LEP Electroweak Working Group [28].)

From the experimental point of view, both measurements are dominated by statistical errors, with accurate studies of the much lower systematic uncertainties. On the other hand a departure of A_{FB}^b from its expected SM value, and as consequence the discrepancy of the b couplings from their SM expectation, seem to be evident from the precise measurements of $\mathcal{A}_b$.

Global Electroweak Fits An efficient way to report the results of the precision tests on the electroweak sector of the Standard Model consists in writing all observables in terms of the parameters of the SM Lagrangian and then produce a global fit by the least square method. The result is shown in Fig. 12. A large number of observables is reproduced, the values of which are linked by their dependence on the parameters of the Lagrangian of the Standard Model. The fit works well thanks to the inclusion of quantum corrections. The presence of only little deviation from the predicted values testifies the validity and strength of the SM itself. The fit represent a huge success for the model in particle physics and also for quantum mechanics on which it is based.

Looking at Fig. 12, it is crucial to notice that the $A_{FB}^{0,b}$ (combined) measurement at LEP is in tension at $\sim 2.4\sigma$ with respect to the expected SM value, and this deviation is the largest one in all the global EW fits. At the state of art, the origin of this discrepancy from SM predictions is not clear, although one among the possible interpretations is that of assuming it to be related to a statistical fluctuation at LEP [30].

Consequently, the two most sensitive determinations of $\sin^2\theta_{\text{eff}}^{\text{lep}}$, from the LEP measurement of $A_{0,b}^{FB}$ and the SLD measurement of A_ℓ, are in $\sim 3\sigma$ tension with each other [44].

The absence of strong disagreements in other variables related to b quarks, but also the potential for this to be a signal of new physics, makes this tension a puzzle to be solved with dedicated experimental and theoretical studies at a future electron circular collider [45]. The strategy to understand this issue is to address not only the expected uncertainties in the measurement of the asymmetries in the b sector, but also in the charm sector, as well as in the polarization and asymmetries of the tau lepton. The tau asymmetry parameter, in fact, allows to determine directly the lepton asymmetry parameter $\mathcal{A}_e$, and extract the value of $\sin^2\theta_W$, without universality assumptions also at a circular collider, where the longitudinal beam polarization may not be achieved. A measurement of the asymmetry in the charm sector will be important, instead, to improve the understanding of the couplings to the up-sector.

Actually, the A_{FB} measurement has not been done since the LEP program expired, at the beginning of the 21$^{\text{st}}$ Century (see Section 3.3). As a consequence, the discrepancy of bottom forward-backward asymmetry from the SM prediction has remained unsolved for the last 20 years. Thus, the precise determination of seems to be quite urgent. To that purpose, the natural strategy is the waiting for the construction of a more, powerful lepton collider, like the FCC-ee, to repeat LEP measurements with more modern analysis techniques and an expected larger data

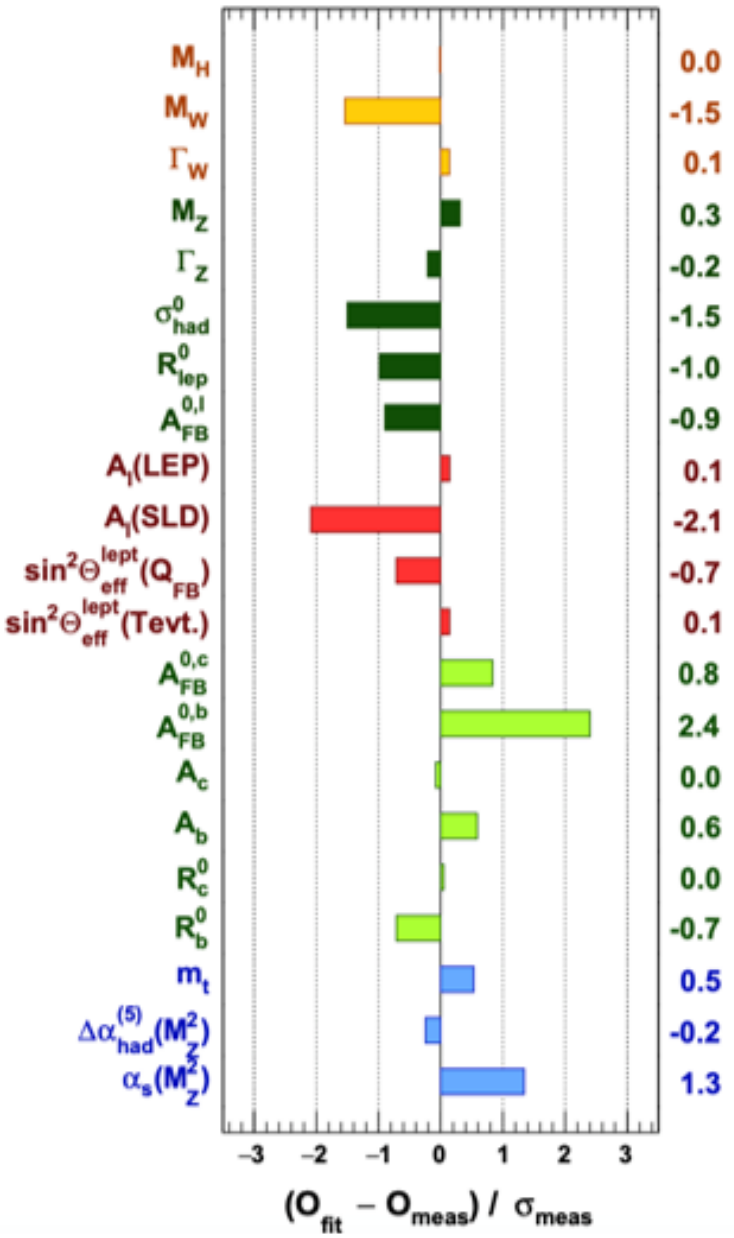

Fig. 12: The global fit of the electroweak observables in the Standard Model. The different observables include masses, widths, asymmetries and couplings. The largest deviation in global EW fits is represented by the b-quark forward-backward asymmetry at Z-pole, $A^{0,b}_{FB}$. [30]

sample (as shown in Section 3.4).

Chapter 3

3 Particle physics at colliders

3.1 Particle colliders

The principal tools for discovery in particle physics are given by *accelerators*. An accelerator is a device which can smash particles (electrons, protons etc...) to produce new particles like the ones which populated the Universe few instants after the Big Bang. If this is done by accelerating and colliding two particle beams coming from opposite directions, the accelerator is properly called a *collider*. Typically the two beams circulate in the same beam pipe. Alternatively, accelerated particle beams can be sent against a fixed target (*fixed target experiments*), often with the purpose of producing secondary beams of charged and neutral particles.

A collider is defined by two main parameters: its *energy* and its *luminosity*. The first one, the energy, is the maximum energy available in the center of mass of the colliding particles, which is equal to the square root of the Mandelstam variable s:

$$E_{CM} = \sqrt{s} = p_1 + p_2 \tag{71}$$

where p_1 and p_2 are the four-momenta of the two incoming beams. This energy is provided by electromagnetic cavities in which strong electric fields accelerate the particles as they come to run inside them on their circular trajectory.

The second parameter is related to the number of collisions performed. Particles are accelerated in bunches. The luminosity $\mathcal{L}$ is given by the number n_1 of the particles in a bunch, by the number of bunches n_2, and, if they come to interact in an area of size a, by the frequency f of collisions:

$$\mathcal{L} = f\frac{n_1 n_2}{a} \tag{72}$$

The luminosity is measured in squared centimeter per second.

In practice, what is interesting is the *rate*, the number of events per second, for a given scattering process. This is given by the cross section σ, which is the probability of that process to take place, times the luminosity:

$$N = \mathcal{L}\sigma \tag{73}$$

where N indicates the rate, which is the number of events of that process per second. This leads to the total number N_{obs} of events of a certain process observed over a

given period of time:

$$N_{\text{obs}} = A \times \epsilon \times \sigma \times \underbrace{\int \mathcal{L}\, dt}_{int.\ luminosity} \tag{74}$$

where the last factor is called *integrated luminosity* over the data taking interval considered. The A and ϵ parameters in Eq. 74 take into account the limited ability of detecting all the produced particles. The *acceptance* A keeps track on the fraction of particles ending up in the detector, out of those which have been produced, and is related to the geometric shape of the detector and of its components. The parameter ϵ instead is the *efficiency* of the final states reconstruction.

Cross sections are measured in squared meter, or in alternative in *barn* (b), defined as $1\,\text{b} = 10^{-24}\text{cm}^2 = 10^{-28}\,\text{m}^2$. The total luminosity is measured in inverse barn, but it is often used a fraction of it, pb^{-1} or fm^{-1}.

A large integrated luminosity is crucial for optimizing physics programs at accelerators, as it provides the experiments with more data for analyses which may involve rare processes.

Colliders can accelerate hadrons (protons and anti-protons) or leptons (typically electrons and positrons) or even a combination of two, or alternatively light and heavy ions, depending on the process one wants to study. Each type of colliders has advantages and disadvantages:

- **Leptonic colliders**. The collision events are, basically, well defined, because no other particles are involved in the initial state than e^+e^-. For a given set of operating conditions, collision energy is actually fixed (energy of e^+e^- known). Unfortunately, the synchrotron radiation emitted by the circulating electrons is a limiting factor as it increases as the fourth power of the energy; which means that it becomes more and more difficult to accelerate the electrons (Eq. 75). For this reasons, such colliders are typically employed for precision studies of a given set of processes.

- **Hadronic colliders** produce less synchrotron radiation (simply because this radiation also goes as the fourth power of the inverse of the mass of the accelerated particles, as shown in Eq. 75) and can thus reach higher energies. However, the energy is shared among the constituents of the accelerated hadrons, the initial state and energy of the colliding qq, $q\bar{q}$ or gg are not known, and there is a very large background of underlying events. The collision events are in fact quite messy: besides the gluons or quark (or antiquark) pairs which make a so-called "*head-on*" collision, the rest of the incoming hadrons can interact producing "debris", which can make more difficult to reconstruct the

main interaction. Hadronic colliders are largely used as tools for discovery at energy frontier.

The difference in terms of energy that can be reached in the two different categories of collider is related to the power emitted by a particle of charge q, mass m and energy E which is moving along a circle of radius R in the direction of the particle's velocity. The power emitted via this *synchrotron radiation* is:

$$P = \frac{q^2 \beta^4}{6\pi R^2} \frac{E^4}{m^4} \tag{75}$$

where $\beta = \frac{v}{c}$ is the velocity of the charged particle, normalized to the speed of light.

Most colliders in the world are indeed *synchrotrons*: they represent the best solution both for high-energy particle physics studies and for high-precision studies in the field of physics of the surfaces. In a synchrotron, charged particles are grouped in bunches and accelerated with *radiofrequency* (RF) *cavities*, while dipole magnets (or supermagnets) keep the particles in a circular orbit within a vacuum pipe, which is a torus with few squared centimeters of cross section. Quadrupoles (or sextupoles, ottupoles etc...) magnets are used to focus and connect the beam. The frequency is modulated in the RF cavities so that it maintains the correct phase at the particles' passages during the various accelerating revolutions. Thus, the intensity of the magnetic field produced by bipolar magnets $\vec{B}$ is variable, and given by:

$$B_{i+1} = \frac{\sqrt{(E_i)^2 - mc^2}}{c\, q\, r} \tag{76}$$

where r is the radius of the circular orbit, m the mass of the particle and E_i the total energy of the particle at the i^{th}-revolution. Notice that the orbit is only approximately a circle, since it is in reality composed by the alternation of straight sections (which accelerate particles) and curved parts (where bending magnets are located).

The complexity of a typical event at a collider is at first sight staggering. There are five elements which contribute to the full picture:

- **the "head-on" process**. This is the primary hard collision. The interactions among quarks, leptons, gluons and electroweak gauge bosons is described by the SM Lagrangian and are originated by the incoming hadrons (p, $\bar{p}$) or leptons ($e^{\pm}$). At present colliders there can be even multiple head-on processes in one collision;

- **the shower**. The subsequent evolution of the partons generates decays and a shower (both electromagnetic and strong) of particles. The showers can originate from both the initial and the final states;

- **the hadronization of the partons**. Eventually all the coloured [19] partons hadronize. Hadronization is the process of the formation of hadrons out of quarks and gluons, described by non-perturbative QCD;

- **the decays of the final hadrons**. The hadrons produced by the hadronization may also further decay, typically through weak interactions in leptonic or semileptonic channels;

3.2 Collider physics: kinematic variables

Before dealing with the features of some particle accelerators, it is important to underline that collider physics has a language of its own in terms of kinematical variables. A brief summary of the conventional coordinate system which is considered in this work is given below.

- The nominal interaction point, i.e. the point in which the collision occurs, is defined as the origin of the coordinate system;

- the z-axis is parallel to the beam;

- the x- and y- axes are perpendicular to the beam;

- x-, y- and z- form a right-handed cartesian coordinate system where x points towards the center of the accelerating ring and y points upward. The $x-y$ plane is called the *transverse plane*;

- the azimuthal angle ϕ is measured around the z-axis, and the polar angle θ is measured from the z-axis;

- particles are often described by their transverse momentum p_T and transverse energy E_T (projections in the transverse plane), as these variables are a better indicator of interesting physics than the standard energy and momentum and since they are assumed to be zero for the colliding partons in the initial state [46].

The momenta of the incoming protons (or proton and anti-proton) or leptons have a very large component in the direction of the beam that is identified with the z direction. The components of the momentum $p^\mu = (E, p'_x, p'_y, p'_z)$ are best written as

$$p^\mu = (p^+, p^-, p_x, p_y) \tag{77}$$

[19] Coloured particles are not colour singlets and thus are not directly observable as free states.

where

$$p^{\pm} = \frac{E \pm p'_z}{\sqrt{2}} \tag{78}$$

and

$$\begin{cases} p_x = p_T \sin\phi \\ p_y = p_T \cos\phi \end{cases} \tag{79}$$

for $\vec{p}_T^{\,2} = p'^{\,2}_x + p'^{\,2}_y$, with ϕ being the azimuthal angle.

Moreover, it is possible to define the *rapidity* y from the components of the particle momentum:

$$y = \frac{1}{2} \log \frac{E + p'_z}{E - p'_z} \tag{80}$$

The rapidity is related to the *polar angle* θ, that is, the angle between the scattered particle direction and the beam direction. For a massless particle or in the limit of very high energy, where fermion and boson masses are negligible, the rapidity becomes:

$$y = \frac{1}{2} \log \frac{E + p'_z}{E - p'_z} = \frac{1}{2} \log \frac{|\vec{p}| + p'_z}{|\vec{p}| - p'_z} \tag{81}$$

$$= \frac{1}{2} \log \frac{1 + \cos\theta}{1 - \cos\theta} = \frac{1}{2} \log \frac{1}{\tan^2 \theta/2} \tag{82}$$

$$= -\log \tan \frac{\theta}{2} \equiv \eta \tag{83}$$

where η is called *pseudorapidity*. By inverting Eq. 81, the scattering angle can be extracted from η:

$$\theta = 2 \arctan\left(e^{-\eta}\right) \tag{84}$$

For a massive particle, rapidity and pseudorapidity do not exactly coincide, especially in case of low energies or momenta, i.e. when a particle's energy is comparable to its mass:

$$\sinh\eta = \sqrt{1 + \frac{m^2}{|\vec{p}|^2}} \sinh y \tag{85}$$

Pseudorapidity is often used as a polar coordinate, since is invariant under Lorentz boost along the beam line (z-axis) for massless particles.

In high energy physics an event is then typically defined in terms of the two variables η and ϕ, in a so-called *lego-plot*.

Starting from the definitions of the observables η (or alternatively θ) and ϕ, a distance between two events, for instance between two jets or two reconstructed tracks, is measured by

$$\Delta R = \sqrt{\Delta\eta^2 + \Delta\phi^2}, \tag{86}$$

and the jet profile is described in terms of E_T, rapidity and azimuthal angles for the sub-components.

The work of this thesis is concentrated on the forward-backward asymmetry analysis which will be conducted at a lepton collider (FCC-ee), which will be built in the future (see Section 3.4). This analysis has been performed at the previous LEP collider (see Section 3.3), and in this Chapter some details of these two machines will be presented.

3.3 Large Electron-Positron collider

The *Large Electron-Positron collider* (abbreviated in LEP) at CERN [20] (the French *Conseil Européen pour la Recherche Nucléaire*, European Council for the Nuclear Research) was situated in the region between the Leman Lake, near Geneva, and the Jura mountains, straddling the Franco-Swiss border. LEP occupied the underground tunnel now used for the *Large Hadron Collider* (LHC). It reached the highest energies ever in e^+e^- collisions and it was characterized by a very precise beam-energy calibration. The tunnel had a length of 26.7 km and was 3.8 m wide. As shown in Fig. 13, four large underground halls, located at a depth varying between 50 and 150 meters, housed the ALEPH, DELPHI, L3 and OPAL detectors.

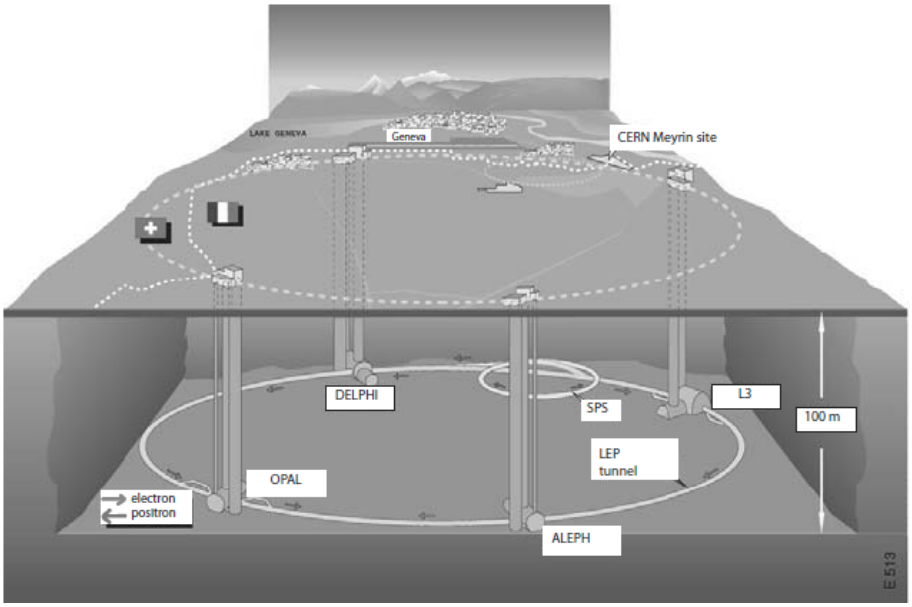

Fig. 13: A sketch of LEP collider with its experiments.

The accelerator was approximately circular, consisting of eight arcs of 2.8 km length and eight straight sections. The electrons and positrons were accelerated at

[20] CERN was officially founded on 29^{th} September 1954, and represents the world's biggest particle physics laboratory at the actual state of art.

20 GeV by the CERN accelerators complex and injected into LEP, where they were further accelerated at their maximum energy. The beam energy was about 45 GeV for the Z run that took place in the years 1989–1995 (LEP1 phase), and reached the maximum energy of 104.5 GeV in year 2000, after five years of operation above the WW threshold (LEP2 phase).

In the LEP1 phase the beams were accelerated by copper radiofrequency (RF) cavities positioned in the straight sections on either side of the experimental halls. The RF cavities were replaced by superconducting cavities in the second, higher energy, LEP2 phase. The replacement was required to compensate the higher energy loss per turn [21] at LEP2, that was about 2 GeV to be compared with 125 MeV at LEP1. The beams were bended in the eight arcs by 3400 dipole magnets and focused by 800 quadrupoles and 500 sextupoles magnets. Electrons and positrons were grouped in bunches and circulated in opposite directions with a frequency of about $11\,kHz$. Typically four bunches were used at LEP, during the LEP1 phase a fraction of data was delivered with eight bunches and even with bunch trains. Most of the LEP1 data was collected closely to the Z *pole*, which is the energy equivalent to the mass of the Z-boson; however, a sizeable fraction of the data was also delivered at side center-of-mass energies, up to 3 GeV above and below the peak of the Z resonance. Such energy scans were essential for the measurement of the Z lineshape. The beams were colliding at the center of the four experimental apparatus, interacting in a region approximately 300 μm wide along the LEP bending radius, 60 μm wide in the vertical direction and 2 mm wide along the beam direction.

LEP achieved a record luminosity of $2.3 \times 10^{31}\,cm^{-2}s^{-1}$ during the Z runs, and went above $10^{32}\,cm^{-2}s^{-1}$ in the LEP2 phase. The total integrated luminosity delivered at the Z, so in the LEP1 phase, was about $150\,pb^{-1}$ per experiment; the four experiments collected a total statistics of more than 15 millions hadronic Z decays and 1.7 millions leptonic Z decays. At LEP2 about $600\,pb^{-1}$ per experiment were delivered, for a total of about 10000 WW interactions per experiment. [30].

Due to its features, LEP represented a milestone in the history of particle physics: in fact, LEP experiments investigated in the 1990's almost every aspect of the electroweak sector of the Standard Model, confirming his consistency in a wide variety of precision studies. LEP had the privilege of opening a new, modern way in investigating the SM, and the competences developed at the four underground experiments resulted crucial in the construction of LHC at the beginning of the 21^{th} Century.

[21] As mentioned in Section 3.1, the energy loss per turn is related to bremssstrahlung, and is much relevant in leptonic machines rather than hadronic machines (like Tevatron collider at Fermilab or LHC at CERN).

3.4 The lepton Future Circular Collider (FCC-ee)

The realization of the *Future Circular Collider* (FCC) will be one of the greatest challenges for particle physics at colliders in the near future. At the time of writing (October 2022), the FCC study is developing designs for a new research infrastructure to host the next generation of higher performance particle colliders to extend the research currently being conducted at the LHC, once the High-Luminosity phase (HL-LHC) reaches its conclusion in around 2040. In the FCC project lots of research institutions are already involved, including CERN and INFN, the Italian Institute for Nuclear Physics [22].

The goal of the FCC is to push the energy and intensity frontiers of particle colliders, with the aim of reaching collision energies of 100 TeV (for hadronic collisions), in the search for new physics.

FCC is planned to be build at CERN, in a region between the Jura mountains and the Geneva lake, slightly west of the LHC tunnel.

The FCC examines scenarios for three different types of particle collisions: hadron (proton–proton and heavy ion) collisions, like in the LHC (FCC-hh), and electron–positron collisions (FCC-ee), like in the former LEP. Other options include proton–electron collisions or proton-heavy ion collisions. A simple sketch is reported in Fig. 14. The leptonic scenario is the one interesting for this Thesis work and will be described in more detail.

FCC is planned to be built after 2030, located at the depth of about $100\,m$, and will operate as a leptonic machine in the years 2045-2060. His design provides a high luminosity at each of many different collision energies, between $88\,GeV$ and $365\,GeV$, as required for $t\bar{t}$ operations, while satisfying several stringent constraints. Apart from a $\pm 1.2\,km$-long section around each interaction point (IP), the machine follows the layout of the $97.756\,km$ circumference hadron collider [47]. The present design houses two interaction points (see Fig. 14). The synchrotron radiation power is limited to $50\,MW$ per beam at all energies.

FCC-ee is designed as a double ring collider, like the KEKB in Japan (which is an asymmetric e^+e^- collider) and PEP-II B (at SLAC, California) factories: this configuration allows to circulate a large number of bunches. The two beam lines cross at two interaction points (IPs) with a horizontal crossing angle of 30 mrad. Two RF sections per ring are placed in the straight sections at points D and J. The RF cavities will be common to e^+ and e^- in the case of $t\bar{t}$. Some FCC-ee parameters are shown in Tab. 4:

The beam current varies greatly between the Z-pole and the $t\bar{t}$ threshold. The

[22] INFN stands for *Istituto Nazionale di Fisica Nucleare.*

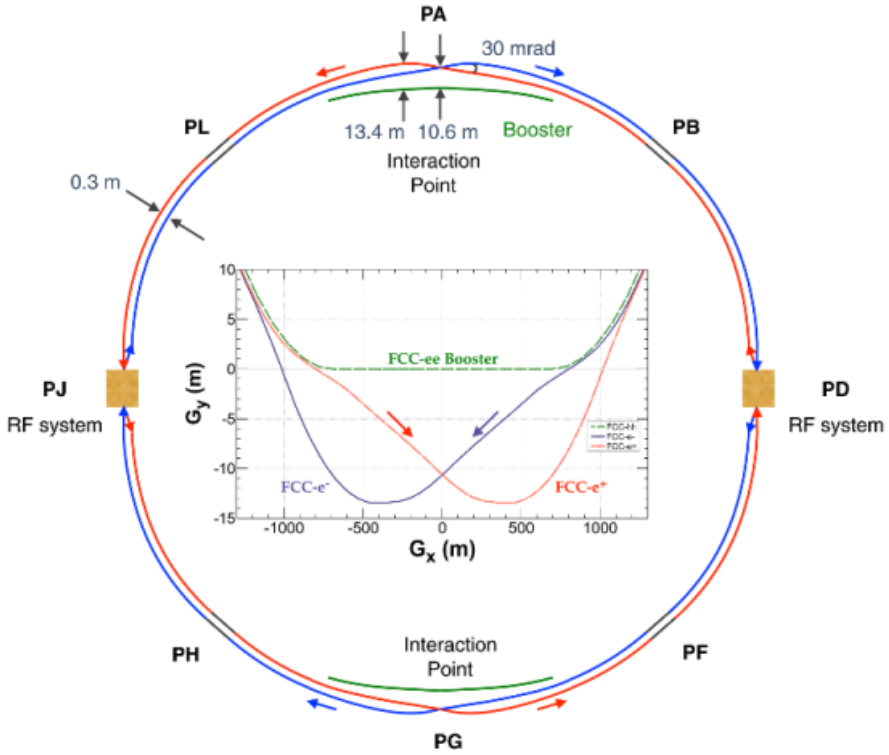

Fig. 14: Overall layout of the FCC-ee (non in-scale) with a zoomed view of the trajectories across interaction point G. The FCC-ee rings are placed $1\,m$ outside the FCC-hh footprint (used for the booster and indicated in green colour in the figure) in the arc. In the arc the e^+ and e^- rings are horizontally separated by $30\,cm$. The main booster follows the footprint of the FCC-hh collider ring. The interaction points are shifted by $10.6\,m$ towards the outside of FCC-hh. The beam trajectories toward the interaction point are straighter than the outgoing ones in order to reduce the synchrotron radiation at the interaction point itself.

current is adjusted primarily by changing the number of bunches. In present electron storage rings, the equilibrium beam parameters are determined by synchrotron radiation generated in the dipoles of the collider arcs. For the FCC-ee, the energy spread and the beam lifetime are also affected by *beamstrahlung*, which is a radiation emitted by the bended electrons and positrons (see Section 3.1).

As a result of the renewed worldwide interest for e^+e^- physics and the pertaining discovery potential since the observation of the Higgs boson at LHC, the FCC is not alone in its quest. At the time of writing, besides the FCC-ee [47], [48], other collider designs are contemplated to study the properties of the Higgs boson and other SM particles with an unprecedented precision: International Linear Collider (ILC [49]) project with a center-of-mass energy of 250 GeV [50], [51]; the Compact Linear Collider (CLIC [52]), whose lowest center-of-mass energy point was reduced

	Z	WW	ZH	$t\bar{t}_1$	$t\bar{t}_2$
Beam energy (GeV)	45.6	80	120	175	182.5
Beam current (mA)	1390	147	29	6.4	5.4
Bunches per beam	16640	2000	328	59	48
Average bunch spacing (ns)	19.6	163	994	2763	3396
Bunch population (10^{11})	1.7	1.5	1.8	2.2	2.3
RF frequency (MHz)	400	400	400	400, 800	400, 800
RF voltage (GV)	0.1	0.75	400	400, 800	400, 800
Actual lifetime (min)	> 200	> 200	18	24	18
Luminosity/IP $(10^{34}\, cm^{-2}s^{-1})$	230	28	8.5	1.8	1.55
Luminosity, Physics Goal (ab^{-1})	150	10	5	0.2	1.5
Run time (year)	4	2	3	1	4

Tab. 4: Machine parameters for the FCC-ee at different beam energies. Informations taken from [58], [56].

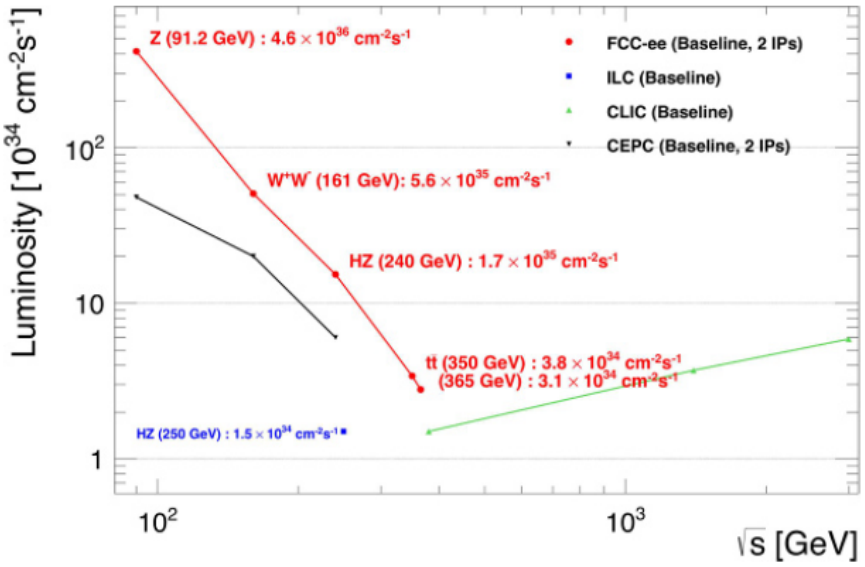

Fig. 15: Baseline luminosities expected to be delivered (summed over all interaction points) as a function of the center-of-mass energy $\sqrt{s}$, at each of the four worldwide e^+e^- collider projects: ILC (blue square), CLIC (green upward triangles), CEPC (black downward triangles), and FCC-ee (red dots), drawn with a 10% safety margin. The FCC-ee performance data are taken from [58], the latest incarnation of the CEPC parameters is inferred from [55], and the linear collider luminosities are taken from [51], [53].

from 500 GeV to 380 GeV [53]; there is also another ongoing project, the Circular Electron Positron Collider (CEPC [54], [55]), in a 100 km tunnel in China, with center-of-mass energies from 90 GeV to 250 GeV. To have an idea of the expected performances of the various leptonic colliders, the baseline luminosities expected

to be delivered at the ILC, CLIC, CEPC, and FCC-ee center-of-mass energies are illustrated in Fig. 15.

Finally, after operating as a leptonic collider [56], FCC will be converted in a hadronic machine in the second half of the 21^{th} Century, to provide proton–proton collisions with a center-of-mass energy of 100 TeV [57], about seven times higher than in LHC [58].

Chapter 4

4 Particle detectors

In an accelerator, collisions between particle bunches occur at especially designed *interaction points* along the particles' orbit. At these points detectors are located with the aims of identifying and collecting the events which are produced in the collisions. The presence and the properties of the particles can be measured by the detectors, thanks to their interactions with the detector material. It is then possible to distinguish different kind of particles, as shown in Tab. 5.

Type of particles	Lifetime	Examples of particles
stable states	∞	p, $\bar{p}$, e^+, e^-, γ
quasi-stable states	$880\,s$ (n, from [59]) $\sim 10^{-6} \div 10^{-15}\,s$	n, $\bar{n}$ $\mu^{\pm}$, $\tau^{\pm}$, $\pi^{\pm}$, $K^{0,\pm}$, $D^{0,\pm}$, $B^{0,\pm}$
short-lived states	$< 10^{-15}\,s$	π^0, $\rho^{0,\pm}$, t, $\bar{t}$, $W^{\pm}$, Z, h
invisible states	∞	ν^e, ν^{μ}, ν^{τ}

Tab. 5: Classification of particles produced in a typical high-energy physics experiment. Neutrinos' lifetimes are not infinite, but they can be assumed very large in vacuum whether *neutrino oscillations* phenomena are not considered.

In this classification, unlike stable and quasi-stable states, short-lived particles are not directly visible and their presence can be deduced by their electromagnetic or strong decays. Instead, invisible particles are not seen at all but their presence can be inferred by the value of the missing energy.

The interesting events must be selected with stringent criteria, taking advantage of their distinctive signatures. The initial selection is based on the requirement of high p_T decay products, i.e. high energy jets and leptons in the central part of the detector, with the central part being normally referred to the low pseudorapidity region (see Section 3.2).

Tab. 6 summarizes the typical different elements (i.e. sub-detectors) which compose a modern detector at a collider. Each sub-detector is designed to identify and measure a given type of particles. The sub-detectors are arranged as concentric cylinders with their axes along the beam axes [60].

Tracker In a typical detector for high-energy particle physics, the innermost part is usually occupied by a tracking system. Its functions are those to reconstruct the charge, the trajectories and momenta of the charged particles produced in the primary and secondary interaction vertices. This is done by applying a strong

Detector element	Principle	Particles
Microvertex detector	High resolution detector near the primary vertex	Heavy quarks and leptons
Inner tracking chamber	Drift chamber, crystals or silicon detector to track charged particles	$e^{\pm}$, $\mu^{\pm}$, charged hadrons
EM calorimeter	Sub-detector to measure the energy deposited by leptons and photons	$e^{\pm}$, γ, jets
Hadron calorimeter	Sub-detector to measure the energy deposited by hadrons	p, n, $\pi^{0,\pm}$, jets, etc.
Muon chamber	Drift chamber to register the trajectories of muons	$\mu^{\pm}$

Tab. 6: Various components of a typical detector, together with the particles which are identified and measured.

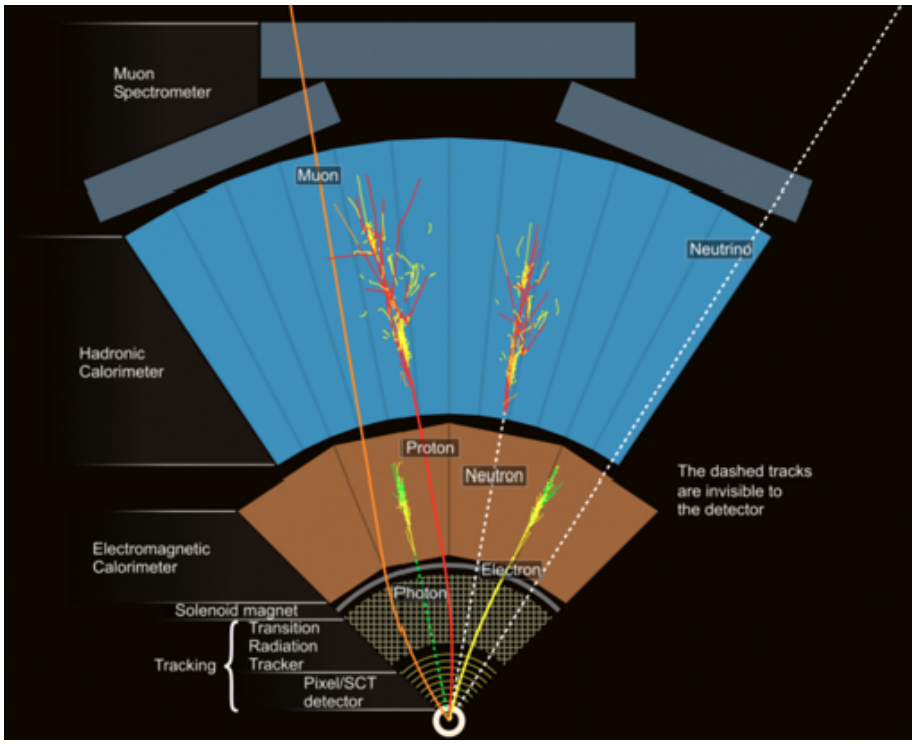

Fig. 16: Section view of a typical detector showing the various layers of which is composed. The tracker and calorimeters can be made of various materials and with various techniques. Picture taken from [61].

magnetic field B, so the momentum of a charged particle passing through the tracker

can be measured by considering the imposed curvature:

$$p = 0.3\, B\, R \tag{87}$$

where R (in m) is the curvature radius of the particle with momentum p (in GeV), when a magnetic field B (in T) is applied.

Nowadays in most of the experiments of particle physics, the tracker is often including an innermost section called "microvertex detector" (also listed in Tab. 6), which has the function to identify the secondary vertices.

Trackers can be made up with different technologies: pixel detectors and multi-wire proportional chambers are examples of devices largely used in modern experiments due to their excellent performances in terms of resolution. Trackers are usually made of light materials (like silicon) in order not to degrade the particle energy [62].

Calorimeter *Calorimetry* is that part of physics which refers to the detection and measurement of particles and their properties through the total or partial absorption of their energy in a block of matter. This destructive process consists in the conversion of the incoming particle energy E into an electric, optical, thermic or eventually acoustic signal. The detector response S has to be proportional to E:

$$S \propto E. \tag{88}$$

In general, a calorimeter is sensitive to almost all SM particles, both charged and neutrals. It is a flexible and compact detector, which in association with the tracker can be employed in particle identification thanks to different response to electrons/photons, single hadrons, muons, tauons, jets, and for angular or time measurements.

Particle interaction with matter will generate a cascade (shower) of lower energy particles until these (or at least their energy) are absorbed in the material itself. The goal is that the number of secondary particles directly scales with the initial particle energy to insure linearity: the greater the energy of the incoming particle, the larger the number of secondaries and the better the resolution, since the detection is based on stocastic processes.

Particle showers in calorimetry, as well as the correspondent calorimeters specialized to detect them, are divided into two categories: electromagnetic and hadronic.

- **Electromagnetic showers** are initiated by e^+, e^- or γ, present a narrow transverse section, and there are little shower-to-shower fluctuations. Their physics is dominated by QED. Bremsstrahlung and pair production are at the

base of the shower propagation, while ionisation (Bethe-Bloch), photoelectric effect and Compton effect are the other phenomena through which photons and light leptons ($e^{\pm}$ or ultra-relativistic $\mu^{\pm}$) can loose most of their energy [62], once the shower development is completed.

- **Hadronic showers** are more complex, being initialized by a hadron (p, n or π). They have large transverse section, with large shower-to-shower fluctuations and their physics is dominated by QCD. About 30 % of their development is determined by EM cascade: this is related to the $\pi^0 \to \gamma\gamma$ electromagnetic decay for the neutral pions, which number can be assumed of the order of 1/3 of the number of the total pions in the whole hadronic shower.

Furthermore, calorimeters are divided into other two categories: *homogeneous* and *sampling calorimeters*. In a homogeneous calorimeters, the detector coincides with the absorber since the structure is composed by a unique material. The entire volume is sensitive to the particles and contribute to the signal generation. They can detect different types of photons, depending on the material they are made of: those produced by Cherenkov effect, or by de-excitation of the ionized atoms along the tracks released by the incoming charge particles; alternatively, they can convert photons in electrons, with the consequence of giving an electric signal proportional to the generated light (this may be the case of large-scale used organic scintillators). Drift chambers and noble liquid detectors (Ar, Kr, Xe at cryogenic temperature) too can be considered as homogeneous calorimeters, with the collection of the charge produced by ionization. This category of calorimeters is usually applied for the reconstruction of electromagnetic showers.

On the other side, sampling calorimeters provide that the functions of particle absorption and signal generation are exercised by different materials, respectively by passive and active media. With respect to the homogeneous ones, sampling calorimeters are cheaper and more flexible. Absorbing, passive materials typically present high atomic number Z (Pb, W, Fe), while detecting, active sections can be scintillators, proportional or ionizing chambers or scintillating fibers. Sampling devices are preferably employed in hadronic calorimetry, due to the enormous complexity of hadronic showers in high-energy physics.

4.1 FCC-ee detectors

The precision physics program at the FCC-ee (see Section 3.4 for details) sets stringent requirements on the detector performance, like a very large solid angle coverage,

excellent particle identification, very good energy and momentum resolution, and efficient track and vertex reconstruction.

As mentioned in Section 3.4, FCC will operate at various center-of-mass energy and will investigate the Z-boson and the Higgs boson physics, at ZH and H production threshold. The detector performance requirements constraints are set by considering specific physics goals for the most important measurements to be performed. Some of these requirements are reported in Tab. 7.

Physics process	Branching ratio	Detector part	Performance requirement
ZH, $Z \to e^+e^-$, $\mu^+\mu^-$ $H \to \mu^+\mu^-$	m_H, $\sigma(ZH)$ BR($H \to \mu^+\mu^-$)	Tracker	$\Delta(1/p_T) = 2 \cdot 10^{-5} + \frac{0.001}{p(\text{GeV})\sin^{3/2}\theta}$
$H \to b\bar{b}, c\bar{c}, gg$	BR($H \to b\bar{b}, c\bar{c}, gg$)	Vertex	$\sigma_{r\phi} = 5 + \frac{10}{p(\text{GeV})\sin^{3/2}\theta}(\mu\text{m})$
$H \to q\bar{q}, WW^*, ZZ^*$	BR($H \to q\bar{q}, WW^*, ZZ^*$)	ECAL, HCAL	$\sigma_E^{\text{jet}}/E \sim 4\%$ at 100 GeV
$H \to \gamma\gamma$	BR($H \to \gamma\gamma$)	ECAL	$\Delta E/E = \frac{0.20}{\sqrt{E(\text{GeV})}} + 0.01$

Tab. 7: Constraints and performance requirements for FCC-ee detectors.

At the time of writing, there are three main detector concepts for FCC-ee, as listed below:

- CLD concept;
- noble liquid ECAL-based detector;
- IDEA concept.

CLD (which stands for **C**LIC-**l**ike **D**etector) is characterized by a well-established design, based on the work for the detector at CLIC [53]. It is characterized by a silicon tracker, an electromagnetic calorimeter (ECAL) made by tungsten, and a hadronic calorimeter (HCAL) in iron [63]. Some of its key parameters are reported in Tab. 8.

Another interesting concept for FCC-ee is in its infancy at the time of writing, and is based on a high-granularity noble liquid electromagnetic calorimeter [64]. It is characterized by a vertex detector and a drift chamber in the innermost parts. The proposed calorimeter is a sampling detector with inclined lead or tungsten absorbers interleaved with liquid Argon (LAr), Krypton (LKr) or Xenon (LXe) gaps, as shown in the top left schema of Fig. 18.

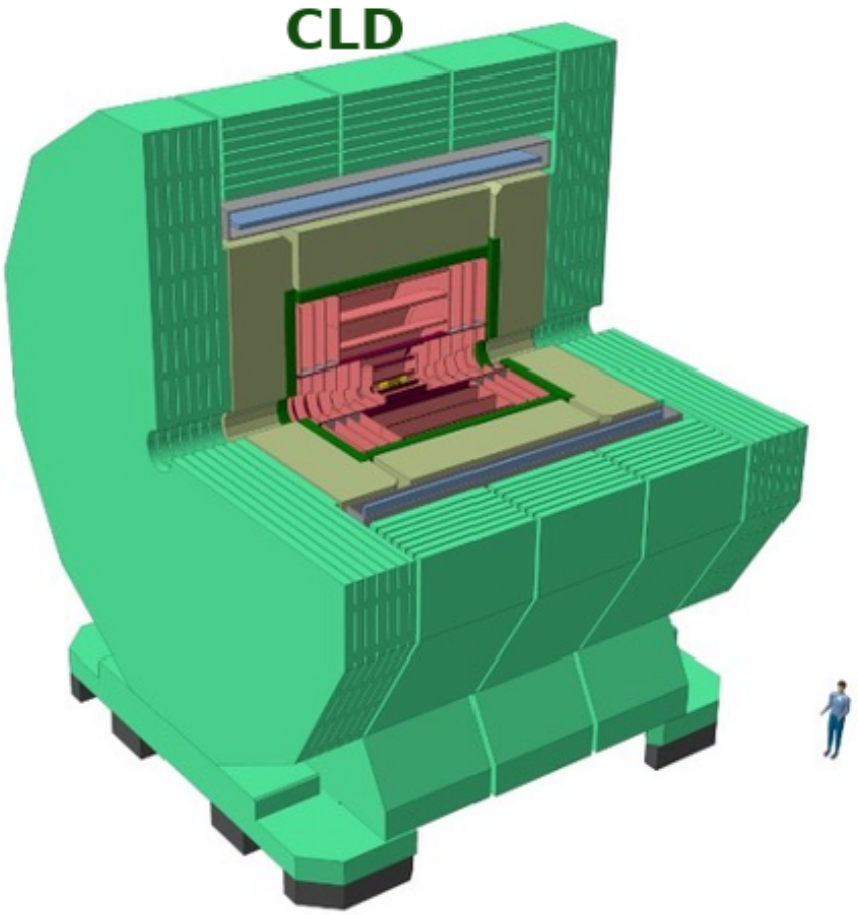

Fig. 17: Schematic layout of the CLD concept for FCC-ee. [63].

Vertex technology	Silicon
Vertex inner radius	1.75 cm
Vertex outer radius	5.8 cm
Tracker technology	Silicon
Tracker inner radius/outer radius	0.127 m/2.1 m
Solenoid field	2 T
Solenoid bore radius/length	3.7 m/7.4 m
ECAL absorber	Tungsten
ECAL (barrel) inner radius	2.40 m
HCAL absorber	Iron
HCAL ring inner/outer radius	2.48 m/3.57 m
Overall height/length	12.0 m/10.6 m

Tab. 8: Key parameters of the CLD detector.

The signal induced by the electromagnetic shower is picked-up by electrodes sitting in the middle of the noble liquid gap from which one creates readout cells. The high longitudinal granularity is achieved by extracting the cell signals both from

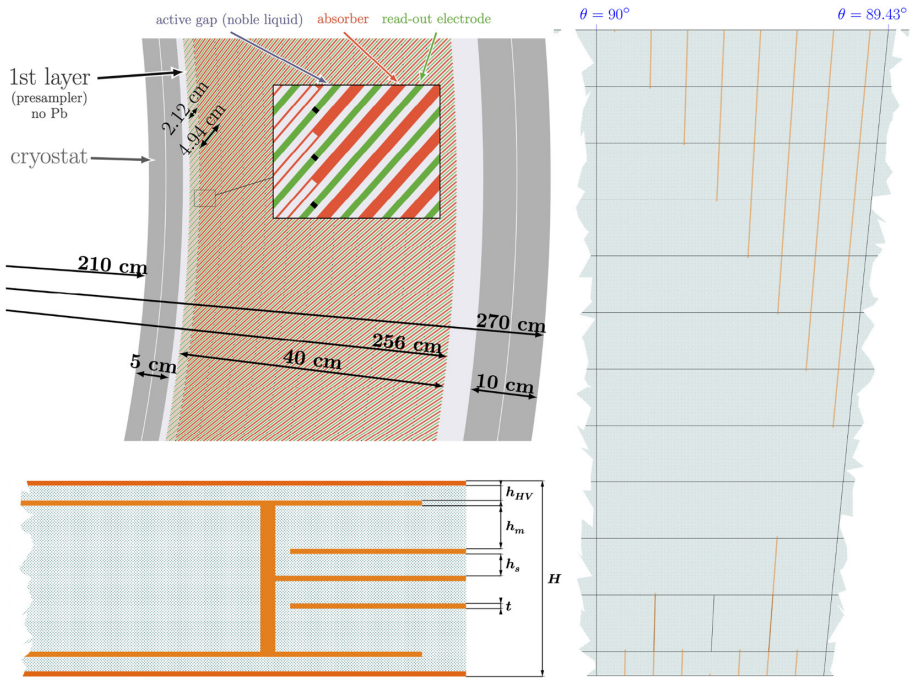

Fig. 18: The FCC-ee Noble Liquid electromagnetic calorimeter. Its layout is shown on the top-left drawing; the signal extraction scheme of the readout electrode is shown on the right-hand side sketch (viewed from top) with a scale 10 : 1 in the horizontal direction. Image taken from [64].

the inner and outer radius sides of the readout electrodes, with traces running inside a multi-layer *Printed Circuit Board*.

Among the detector concepts for the FCC-ee listed above, the IDEA design is considered in this thesis.

4.1.1 IDEA detector

IDEA (which stands for ***I****nnovative* ***D****etectors for* $\boldsymbol{E}^{+}e^{-}$ ***A****ccelerators*) is a handy standard detector concept [65] for fast simulation for physics feasibility studies and is under development specifically for FCC-ee, based on established technologies resulting from years of research.

The structure of the IDEA detector is outlined in Fig. 19, and its key parameters are listed in Tab. 9. The detector comprises a silicon pixel vertex detector, a large-volume extremely-light short-drift wire chamber surrounded by a layer of silicon micro-strip detectors, a thin, low-mass superconducting solenoid coil, a pre-shower detector, a dual-readout calorimeter, and muon chambers within the magnet return yoke.

The innermost detector, surrounding the beam pipe, is a silicon pixel detector. Recent test-beam results on the detectors planned for the ALICE ITS upgrade, based

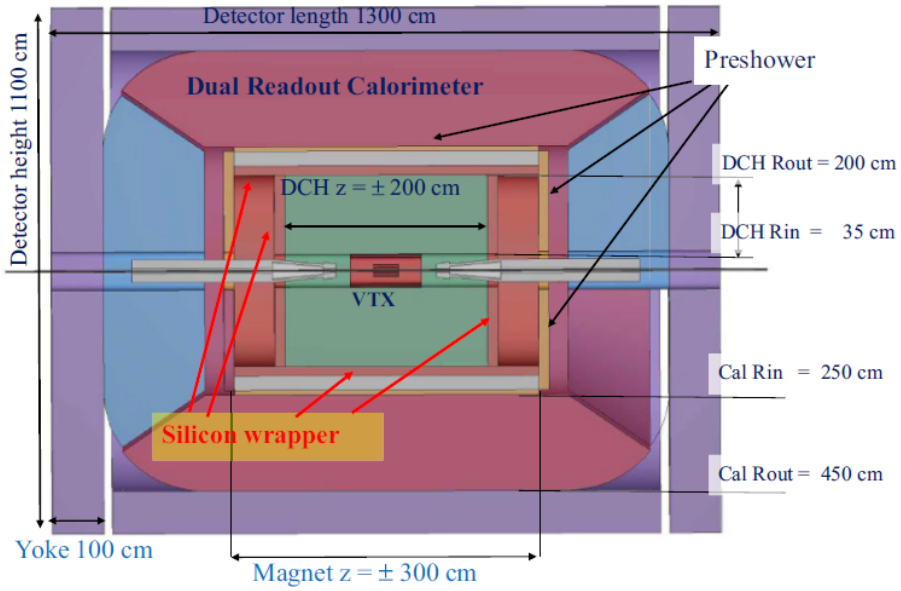

Fig. 19: Schematic layout of the IDEA detector [58].

Vertex technology	Silicon
Vertex inner radius	1.7 cm
Vertex outer radius	34 cm
Tracker technology	Drift chamber + Silicon wrapper
Tracker half length/outer radius	2.0 m/2.0 m
Solenoid bore radius/half length	2.1 m/3.0 m
Pre-shower absorber	Lead
Calorimeter absorber	Lead
Pre-shower inner/outer radius	2.4 m/2.5 m
Calorimeter inner/outer radius	2.5 m/4.5 m
Overall height/length	11 m/13 m

Tab. 9: Key parameters of the IDEA detector.

on the ALPIDE readout chip [66], indicate an excellent ($\sim 5\mu$m) resolution, high efficiency at low power, and low dark-noise rate [67]. These very light detectors, $0.3(1.0)\,\%X_0$, with X_0 being the *radiation length*, per innermost (outermost) layer, are the basis for the IDEA vertex detector.

The IDEA drift chamber (DCH) is designed to provide good tracking, high-precision momentum measurement and excellent particle identification by cluster counting. The main peculiarity of this chamber is its high transparency, in terms of radiation lengths, obtained as a result of the novel approach adopted for the wiring and assembly procedures [68]. The total amount of material in the radial direction towards the barrel calorimeter is of the order of $1.6\%\,X_0$, whereas, in the forward direction, it is about $5.0\,\%X_0$, 75 % of which are in the end plates instrumented with

the front end electronics.

The DCH is a unique-volume, high-granularity, all-stereo, low-mass, cylindrical, short-drift, wire chamber, co-axial with the 2 T solenoid field. It extends from an inner radius $R_{\text{in}} = 0.35$ m to an outer radius $R_{\text{out}} = 2$ m, for a length $L = 4$ m, and consists of 112 co-axial layers, at alternating-sign stereo angles, arranged in 24 identical azimuthal sectors. The approximately-square cell size varies between 12.0 and 14.5 mm for a total of 56448 drift cells.

The chamber is operated with a very light gas mixture, 90% He-10% iC_4H_{10} (isobutane), corresponding to a maximum drift of 400 ns. The angular coverage extends down to $\tilde{1}3\,^\circ$, and could be further extended with additional silicon disks between the DCH and the calorimeter end caps. Analytical calculations for the expected momentum, transverse momentum and angular resolutions, conservatively assuming a 100 μm point resolution, are plotted in the left panel of Fig. 20.

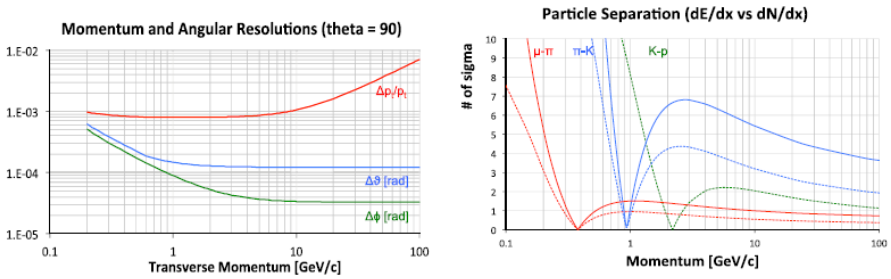

Fig. 20: IDEA drift chamber performance. Left: momentum and angular resolutions for $\theta = 90\,^\circ$ as a function of momentum. Right: particle type separation in units of standard deviations as a function of momentum, with cluster counting (solid curves) and with dE/dx (dashed curves).

IDEA pre-shower detector A pre-shower detector is located between the magnet and the calorimeter in the barrel region and between the drift chamber and the end-cap calorimeter in the forward region. In the barrel region, the magnet coil works as an absorber of about $1\,X_0$ and is followed by one layer of *Micro Pattern Gas Detector* (MPGD) chambers; a second layer of chambers follows after another $1\,X_0$ of lead. A similar construction occurs in the forward region, however, here with both absorber layers made from lead.

The MPGD chamber layers provide an accurate determination of the impact point of both charged particles and photons, and therefore define the tracker acceptance volume with precision. They also further improve the tracking resolution.

In addition, a large fraction of the neutral pions π^0 can be tagged by having both photons from their decay identified by the pre-shower.

IDEA dual-readout calorimeter A lead-fibre dual-readout calorimeter [69] surrounds the second pre-shower layer. The calorimeter is 2 m deep. Two possible layouts have been implemented in the simulation for a realistic $4\,\pi$ detector. Both cover the full volume down to 100 mrad of the z-axis, with no inactive region. In the first configuration, the calorimeter is made of truncated rectangular-base pyramidal towers with 92 different sizes. In the second, it is built with rectangular prisms coupled to pyramidal towers. The total number of fibres is of the order of 108 in both cases.

The dual-readout calorimeter is sensitive to the independent signals from scintillation light (S) and Cherenkov light (C) production, resulting in an excellent energy resolution for both electromagnetic and hadron showers. By combining the two signals, the resolution estimated from GEANT4 simulations is found to be close to $10\%/\sqrt{E}$ for isolated electrons and $30\%/\sqrt{E}$ for isolated pions with negligible constant terms.

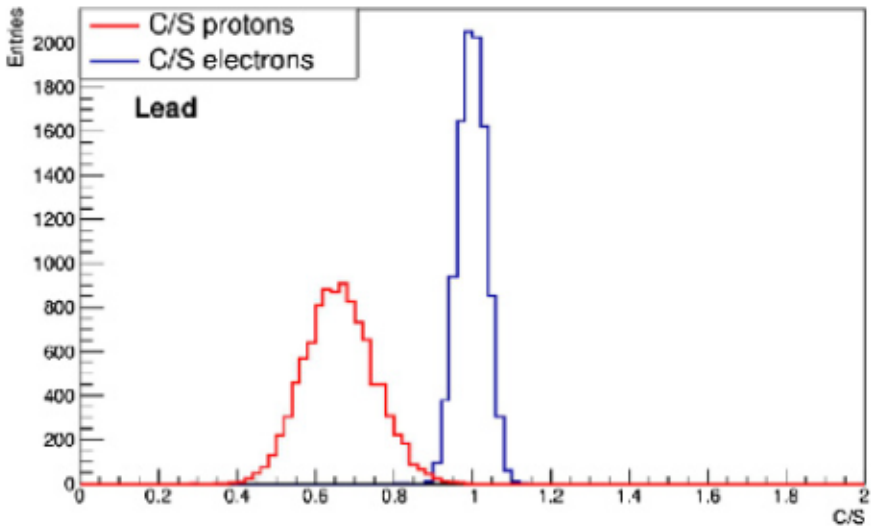

Fig. 21: Particle identification performance of the dual-readout calorimeter: C/S ratio for 80 GeV isolated electrons and protons. [70]

The dual-readout calorimeter provides very good intrinsic discrimination between muons, electrons/photons and hadrons for isolated particles [70]. Fig. 21 demonstrates a nearly perfect separation in the C/S ratio for 80 GeV electrons and protons: for an electron efficiency of 98%, a simulated rejection factor of up to 600 can be reached for isolated protons. The rejection factor in jets remains to be evaluated experimentally.

In addition to the C/S ratio, a few other variables, like the lateral shower profile, the starting time of the signal, and the charge-to-amplitude ratio, can be used to enhance the intrinsic calorimeter particle separation performance.

Besides the intrinsic particle identification capabilities, the fine transverse granularity allows close showers to be separated and provides good matching to tracks in the inner, pre-shower signals, and also to muon tracks, making this calorimeter a good candidate for efficient particle-flow reconstruction. The need for disentangling signals produced by overlapping electromagnetic and hadron showers is likely to require longitudinal segmentation as well. Several ways to implement this segmentation were envisioned and will be studied in the future, e.g. the classical division of the calorimeter in several compartments, an arrangement with fibres starting at different depths, the extended use of the timing information, etc.

IDEA muon system The muon system consists of layers of chambers embedded in the magnet return yoke. The area to be covered is substantial, which calls for a cost-effective chamber technology. Recent developments in the industrialisation of μ-Rwell-based large area chambers [71], proposed for the CMS [23] detector phase-II upgrade, are promising.

4.2 Object reconstruction

In this Section, the way the physics objects are reconstructed in this analysis is briefly described. In general, the typical detectors for particle physics can identify and distinguish several final state particles, as mentioned in 4: electrons, muons, tauons, photons, jets, heavy quark jets (such as b- and c- jets) and neutrinos. Only the objects used in the analysis presented in Section 5 are considered here.

4.2.1 Electrons

Electron reconstruction and identification algorithms are designed to achieve both a large background rejection and a high and uniform efficiency for isolated high-energy ($E_T > 20\,\text{GeV}$) electrons over the full acceptance of the detector. Isolated electrons need to be separated from hadron decays in QCD jets and from secondary electrons originating mostly from photon conversions in the tracker material.

Electron reconstruction is based on the identification of a set of clusters in the electromagnetic calorimeter [72]. The reconstruction efficiency is a function of electron's transverse momentum p_T and pseudorapidity η. In this work, the electron is not identified if $|\eta| > 3.0$; so, in the condition $|\eta| \leq 3.0$, the efficiency for electrons is equal to 0.997 if $p_T \geq 0.5$ GeV, equal to 0.65 if $0.3\,\text{GeV} \leq p_T < 0.5$ GeV, and equal to 0.06 if $p_T < 0.3$ GeV.

[23] CMS is one of the four main experiments at LHC, CERN, together with ALICE, ATLAS and LHCb.

4.2.2 Muons

Together with neutrinos, muons are the only particles that can cross the full system without being absorbed. Muon reconstruction is based on information from the external muon spectrometer, the inner tracker and the calorimeters. Different kinds of muon candidates can be built, depending on how the detector information is used in the reconstruction. Similarly to the electron identification (Section 4.2.1), in this work also the muon efficiency depends on the relative η and p_T. Muons are not reconstructed if $|\eta| > 3.0$; so, in the condition $|\eta| \leq 3.0$, the efficiency for muons is equal to 0.997 if $p_T \geq 0.5$ GeV, equal to 0.65 if $0.3\,\text{GeV} \leq p_T < 0.5$ GeV, and equal to 0.06 if $p_T < 0.3$ GeV.

4.2.3 Photons

Photons have no electric charge, so in principle they do not have an associated track in the inner detector. Like electrons, photon reconstruction is based on the identification of a set of clusters in the electromagnetic calorimeter, where they can initiate electromagnetic showers (see Section 4). Since an EM shower originated by a photon is actually not distinguishable from one initiated by an electron or a positron, the only way to separate the two cases consists in absence or a presence of a corresponding track in the internal section. However, a photon may have converted into $e^{\pm}$ before reaching the EM calorimeter [62]: this is the reason why a typical tracker has low atomic number Z, in order to minimize the probability of photon conversion and, as a consequence, of a mis-identification.

4.2.4 Jets

Hadronic particles deposit their energies mainly in the calorimeter system. In an attempt to resolve particles coming from the hard scatter, these energy deposits may be grouped into object called *jets*. In general, the mapping from partons to jets is a complex problem and it depends strongly on which one is the jet algorithm used. Many solutions have been used or proposed to define jets.

In this work, the so-called *anti-k_T* algorithm [73] has been adopted as default. It is part of a wider part of the wider class of "Clustering Algorithms", based upon pair-wise clustering of the initial constituents. Two "metrics" are defined:

the distance d_{ij} between entities (particles, jets) i and j:

$$d_{ij} = \min\left(k_{T,i}^{2p}, k_{T,j}^{2p}\right)\frac{\Delta R_{ij}^2}{\Delta R^2}; \tag{89}$$

the distance d_{iB} between entity i and the beam:

$$d_{iB} = k_{T,i}^{2p}, \tag{90}$$

where $\Delta R_{ij}^2 = (y_i - y_j)^2 + (\phi_i + \phi_j)^2$, and $k_{T,i}$, y_i and ϕ_i are the transverse momentum, the rapidity and the azimuthal angle of particle i.

The clustering proceeds by identifying the smallest distance among all the entities in the event:

- if it is a d_{ij}, then i and j are combined in a single entity;
- if it is d_{iB}, then i is considered as a single jet and it is removed from the list of entities.

The distances are finally recalculated and the procedure repeated until no entities are left.

Tho parameters characterising the particular jet clustering algorithms are introduced: ΔR and p. For large values of ΔR, the d_{ij} are smaller than the d_{iB}, and thus more merging takes place before jets are complete. The p parameter, instead, causes a preferred ordering of clustering: if the sign of p is positive, clusters with lower energy will be merged first; otherwise, if it is negative, the clustering will start from higher energy clusters. In the anti-k_T algorithm $p = -1$, meaning that objects with high relative momentum k_T are merged first.

Compared with other jet algorithms like the "Cone Algorithms" (for instance, *SisCone* [74]) or other cluster algorithms (like k_T [76] and Cambridge/Aachen [77]), anti-k_T is less sensitive to low energy constituents, its clustering procedure is faster, there is no need of introducing new parameters to decide whether two jets have to be split or merged (the so-called "*split & merge*" procedure, present in the Cone Algorithms [74]) and the resulting jet area is more regular.

The choice of ΔR parameter is analysis dependent: the value of $\Delta R = 0.5$ is used in this work. A cut is applied on the jet transverse momentum p_T: the jet reconstruction occurs only if $p_T > 20\,\text{GeV}$.

4.2.5 b-jets reconstruction

The aim of b-tagging algorithms is to identify jets containing b-flavoured hadrons. For each selected jet, those algorithms provide b-weights reflecting the probability that it originates from a b quark. The discrimination of b-quark jets from light quark jets originates mainly from the relatively long lifetime of b-flavoured hadrons, resulting

in a significant flight path length $L \sim$ mm. This leads to measure secondary vertices and impact parameters of the decay products.

The transverse impact parameter d_0 is the distance in the transverse plane (x,y) (see Section 3.2) between the point of the closest approach of a track to the primary vertex; the longitudinal impact parameter z_0 is the z-coordinate of this point. Various b-tagging algorithms, or "taggers", can be defined, based on these discrimination variables (L, d_0 and z_0), on secondary vertex properties and on the presence of leptons within b-quark jets.

Each tagging algorithm defines a "weight" w, associated to the probability for a given jet to have been originated from a b quark. For each tagging algorithm, different "working points", i.e. different threshold on the w variable cut to define a "tagged" jet, can be used. The choice of the working point sets the tagging efficiency for b-, c- and light quark jets. In this work, based on a Monte Carlo simulation in *Delphes*, the b-tagging efficiency for jets is fixed at

$$\epsilon_b = 0.8, \tag{91}$$

as shown in the *Delphes* card IDEA.

4.2.6 b-quark charge determination

Apart from being able to tell the flavour of the quark originating a hadronic jet, as done through the b-tagging procedure described above, it is often useful to be able to infer the charge of the original quark, by just measuring the properties of the final state jet. This is usually not an easy task due to the fragmentation process giving raise to jets of hadrons in the final state, so it is probably one of the most challenging experimental tasks in collider physics, but it becomes essential in the case of certain measurements, such as the measurement of A_{FB}^b. This challenge is especially relevant in hadron machines, but also in the case of the cleaner environment of leptonic colliders it remains very relevant.

For heavy flavors, no unique general tagging method exists, but different techniques can be applied. The first one is the *soft lepton tagging*, already developed in data analysis at LEP and CDF [83]. It is based on the statement that the b quark, similarly to the other quarks, hadronize within a jet in the detector, thus manifests itself in bound hadronic states like B^0, $\bar{B}^0$ and $B^{\pm}$ mesons; they in turn can decay into leptonic or semileptonic channels. Soft lepton tagging consists in the identification of an isolated *soft lepton*, typically a muon, which can clearly indicate the leptonic or semileptonic decay of a B boson coming from a decaying Z boson [84].

So, restricting the b or $\bar{b}$ jet candidates to those containing a soft lepton, the hadron charge is inferred from the clean measurement of the lepton charge. The adjective "soft" refers to the fact that the identified lepton must have a small momentum in the B-decaying hadron reference frame: this means that, if the B has a huge momentum in the laboratory reference frame, then also the soft lepton will be much energetic (i.e. hard emitted, in the laboratory frame). Among the various lepton families, the muon is the simplest one to use in the soft tagging, because of its low interaction with the calorimeters in detectors [62]. This method requests to know production and decay processes of B hadrons as well as possible, which is supposed to be one of the main sources of systematic uncertainty. For instance, it may occur that a B^0 is converted into a $\bar{B}^0$ before decaying due to the phenomena of B^0-$\bar{B}^0$ oscillations; thus the correspondent positive charged antilepton l^+, which is actually coming from the B^0, must be correctly identified with a $\bar{B}^0$.

However, another method is widely used for the b-jet reconstruction, and consists in the measurement of the so-called "jet charge". For jets initiated both by heavy and light flavour quarks, there is a correlation between the distribution of electric charge of the jet constituents and the charge of the quark or antiquark which originated that jet.

Naively, a up-type quarks and down-type anti-quarks, with charges $+2/3$ and $+1/3$ respectively (see Section 1.1.1 for details), tend to produce in general more positively charged high energy particles in their direction of motion than negatively charged ones, and the other way around for down-type quarks or up-type anti-quarks.

A jet charge quantity can be then defined as the sum of the charges of all the tracks which "belong" to that jet, where a track can be defined as belonging to a certain jet based angular information. In particular, a track can be assigned to a jet if the angular distance ΔR, in terms of pseudorapidity and azimuthal angle (see Eq. 86), is smaller than a pre-defined value, usually set at 0.4 or 0.5 depending on the used jet algorithm.

This sum of the charges can be eventually a weighted sum, considering various options, like the total momentum, the transverse momentum or the longitudinal momentum of the track; the longitudinal direction is defined with respect to the jet direction.

Similarly to the soft lepton tagging method, this jet charge method is sensitive to systematic uncertainties related to the details of the parton shower and hadronization processes. In this thesis, this exact jet charge method is used in the analysis reported in Chapter 5, and the precise procedure which is employed is reported in Section 5.3.

4.2.7 Missing transverse energy

In high-energy physics, neutrinos (see Section 1.1.1) are expected not to interact with the detector, and they can be reconstructed using the difference between the initial and final state total momentum. In a lepton collider, such as FCC-ee (Section 3.4), the initial momentum of the colliding particles is generally known *a priori*, so that in principle the amount of energy can be determined. However, the initial momentum transverse to be beam axis (which is by convention the z-axis, see Section 3.2) is in a good approximation zero, so that the missing energy can be measured in the transverse plane.

The missing transverse energy E_T^{miss} is defined as:

$$E_T^{\text{miss}} = \sqrt{(E_x^{\text{miss}})^2 + (E_y^{\text{miss}})^2}, \tag{92}$$

where E_x^{miss} and E_y^{miss} are the contributions on the x- and y- axes. The missing transverse energy is primarily reconstructed from the energy deposits in the calorimeter and from the reconstructed muon tracks. From momentum conservation, the azimuthal angle ϕ can be obtained, but not the pseudorapidity η, if the detector is not hermetic on the z-axis.

Chapter 5

5 Monte Carlo study on forward-backward asymmetry at the Z-pole

As mentioned in Section 2.6, at present the most important deviation in global EW fits is that of the forward-backward asymmetry for b quarks at the Z-pole, $A_{FB}^{0,b}$. This issue has remained unsolved for about the last 20 years, after the completion of the LEP program at the beginning of the 21^{st} Century (see Section 3.3). The precise measurement of $A_{FB}^{0,b}$ at the future leptonic colliders will then be of utmost importance.

In particular, the FCC-ee will be able to repeat all the precision studies already performed at LEP in the 1990's but with a larger data set and more modern analysis techniques (see Section 3.4). In order to make sure that the design performances of the collider and of its experiments will be suitable for such precise measurements, in particular for $A_{FB}^{0,b}$, simulation-based feasibility studies should be performed already before the finalization of their projects and construction.

This work belongs is indeed a feasibility study for the measurement of the forward-backward asymmetry A_{FB}^{b} in the production of bottom quark/antiquark pairs at the FCC-ee, with a center-of-mass energy $\sqrt{s} = 91.188$ GeV.

It makes use of a simplified Monte Carlo simulation based on the software *Delphes*, implementing a parametric description of the performances of one of the detector designs proposed, namely the IDEA project. Signal events $e^+e^- \to Z \to b\bar{b}$, as well as background events from pair production of lighter quarks, are generated at LO in QCD and EW within the MadGraph framework and showered with *Pythia*. Simulated events are then analysed within the ROOT framework, applying a simple event selection, computing a suitable observable from the reconstructed hadronic jets and charged particle tracks and finally applying an unfolding procedure to obtain a distribution from which to extract the parameter A_{FB}^{0}. The expected statistical uncertainty as well as the most important sources of systematic uncertainty are then computed.

5.1 Simulation software

In order to understand some general aspects of the software used in this thesis, it is important to remember briefly the general structure of a typical event at a collider (as reported in Section 3.1). Since high-energy particle collision events are complicated processes involving, besides the fundamental process under study, initial and final

state radiation effects, unstable particle decays, parton shower and hadronizaton, a dedicated software is employed for their simulation. The Lagrangian of the SM gives the matrix element for the head-on event, which in this case is the process of associated $b\bar{b}$ production from a decaying Z-boson coming from e^+e^- annihilation. While the matrix element, and as a consequence the interaction amplitude, are easily computed in the simplest cases, computation may become more complicated mainly because of the need to integrate over the final-state phase space which becomes complex if there are more than two final state particles. Thus, this matrix element is computed by a dedicated software.

In this thesis, the software MadGraph is used for the simulation of the head-on event [78]. Usually MadGraph performs the event generation in three main steps. First, MadGraph includes the probability distribution functions for the partons (usually called *PDF*s) inside the incoming protons or antiprotons, in case one studies hadromn collider events; clearly, this is not relevant for the case of lepton machines, where the colliding beams are made of elementary and point-like particles. Second, the program computes the cross sections at the partonic level as perturbative series in QCD and QED. Last, MadGraph executes the phase-space integrals by a Monte Carlo simulation.

The output of MadGraph is then fed into another software package, *Pythia*, which simulates the parton shower and hadronization processes. *Pythia* can be used for events generation, especially focusing on multiparticle production in collisions between elementary particles [79] [80]. The most delicate task performed by *Pythia*, the simulation of the hadronization and non-perturbative QCD, is performed with a mix of analytical calculations and empirical models. Pythia implements the so-called p_T-ordered parton shower for the perturbative part of the QCD final-state evolution and the so-called *Lund string model* for the non-perturbative hadronization process [81].

Finally, the simulation of the detector is performed by *Delphes*. *Delphes* is a highly configurable C++ based framework [82] for a fast parametric simulation of a general-purpose collider experiment. Starting from the output of event generators, it simulates how the event is finally recorded in the detector by taking into account the acceptance of the experiment geometry and the instrumental efficiency in the detection. With *Delphes* one gets:

- the geometry of both central and forward detectors;
- the effect of magnetic field on tracks;
- the reconstruction of photons, leptons, jets, b jets, τ jets and missing transverse

energy;

- a trigger emulation;
- a display of the event.

The three parts of the software work together as a chain, and the final result is a *Delphes tree*, i.e. an output file in ROOT format (*.root*) in which all the useful information about reconstructed jets, particles, tracks and their relative energies, momentum and velocity are stored. Through editing appropriate configuration files, called *cards*, it is possible to change the simulation settings (i.e. the number of generated events, the center-of-mass energy, the type of colliding beams), the parameters for parton shower simulation and the SM masses and widths entering in the Lagrangian.

For this work, a set of 13 millions $e^+e^- \to Z \to b\bar{b}$ events have been generated at a center-of-mass energy $\sqrt{s} = 91.1876\,\text{GeV}$, with each beam carrying an energy $E_{\text{beam}} = 45.5938\,\text{GeV}$. An inclusive $Z \to b\bar{b}$ process is considered, and no additional selections are applied during the event generation. The generated process has a cross section $\sigma = 9157\,\text{pb}$ and therefore the integrated luminosity represented by this data-set is:

$$\mathcal{L}_{\text{int}} = \frac{N_{events}}{\sigma} = \frac{1.3 \cdot 10^7}{9157\,\text{pb}} \simeq 1.4\,\text{pb}^{-1} \tag{93}$$

The INFN computing farm in Trieste is used to run the simulation, to store the generated events and to perform the data analysis.

A dedicated *Delphes* card for the IDEA detector geometry and design performance is used in the simulation. An accurate description of IDEA detector concept can be found in Section 4.1.1

5.2 Processing of simulation outputs

The simulated events' information is saved in a set of ROOT files in the form of ROOT trees (TTree class) composed by different branches. There are about four hundred branches in the simulation tree given by MadGraph through *Delphes*. These branches include the detailed information about all the simulated particles (by MadGraph and *Pythia*) as well as of the reconstructed objects by the detector, such as charged particle tracks, hadronic jets, electrons and muons.

5.2.1 Truth-level information

Particles generated by MadGraph and *Pythia* are stored and each one is associated with standard particle identification number (PID) as a default tag for all Standard

Model and Beyond-Standard Model particles, either elementary or composite. By convention, fermions have positive numbers, while antifermions correspond to negative numbers; bosons (both mesons and gauge bosons) and relative anti-bosons are assigned opposite PID numbers. A complete list of the PID codes can be found in the Particle Data Group (PDG) [24]; some of them are reported in Tab. 10.

Particle	PID
d	1
u	2
s	3
c	4
b	5
t	6
b'	7
t'	8
e^-	11
ν_e	12
μ^-	13
ν_μ	14
τ^-	15
ν_τ	16
τ'^-	17
ν'_τ	18
g	(9) 21
γ	22
Z^0	23
W^+	24
h^0/H_1^0	25
Z'/Z_2^0	32
Z^H/Z_3^0	33
W'/W_2^+	34
H^0/H_2^0	35
A^0/H_3^0	36
H^+	37

Tab. 10: Universal particle identification numbers for Monte Carlo event generators and analysis packages in particle physics. Particles are given positive numbers, antiparticles negative numbers. The PDG convention for mesons is used, so that K^+, B^+, W^+ are particles, and their conjugates antiparticles. Here only a fraction of some existing or hypothesized particles are list. For a more detailed discussion, see PDG [24].

As shown in Tab. 10, b and $\bar{b}$, e^- and e^+, and Z, which are the main particles involved in the process $e^+e^- \to b\bar{b}$ at $\sqrt{s} \simeq 91.188$ GeV, have PID respectively 5 and

-5, 11 and -11, and 23 according with the PDG formalism [24]. PID information belongs to the branch "Particle" in *Delphes* tree.

Besides the PID, for each generated particle all its kinematic properties are stored, in the form of four momentum, together with selected information regarding the so-called particle "status" (i.e. whether the particle is part of the initial state, an intermediate particle, or a stable final-state particle) and on the parent-daughter links with other generated particles.

5.2.2 Reconstruction-level information

The information related to the "reconstructed" objects, i.e. those coming from the detector simulation, is stored in a number of additional branches (e.g. "Jet", "Track", "Electron",...). Through them, it is possible to access to all the typical experimental observables for these kind of objects, such as:

- azimuthal angle ϕ;
- total momentum p;
- transverse momentum p_T;
- electric charge Q;
- mass m;
- pseudorapidity η [24].

In this thesis, only information about jets and tracks are used.

Jets are reconstructed with an *anti-k_T* clustering algorithm, with the ΔR parameter (Section 4.2.4) set to 0.5. Cuts on their transverse momentum p_T and pseudorapidity η are applied in *Delphes* framework: the jet identification is performed only if its $p_T > 20\,\text{GeV}$ and if $|\eta| < 2.5$. Both the clustering algorithm and the cut on jet p_T can be changed by editing the relative *Delphes* card.

Similarly to jets, cuts on tracks' transverse momentum and pseudorapidity are also applied: more precisely, tracks from charged particles passing through the inner tracker are stored if they have $|\eta| < 2.5$ and $p_T > 100$ MeV.

The settings and performances of b-tagging, stored in the *Pythia* card, are:

- b-jets mis-identification rate = 0.01;
- c-jets mis-identification rate = 0.10;

[24] Note that *Delphes* does not allow to get directly the scattering (polar) angle θ of a jet or a particle, but this is derived from η through Eq. 84

- b-tagging efficiency = 0.80.

These numbers, which are independent from the jet kinematics, are set as a rough estimate of the b-tagging performances foreseen for the IDEA detector.

5.3 Jet charge determination

One of the key parts of the analysis reported in this work, is the determination of the jet charge (see Section 4.2.5). In particular, one of the two general strategies described in Section 4.2.6 is implemented: the one based on a weighted sum of the tracks in a jet. For this purpose, the following procedure is applied for each jet in the event.

1) First, for each simulated event all the jets and tracks, identified by the IDEA detector, are considered.

2) The b, $\bar{b}$ jet candidates are restricted to those that are b-tagged by *Delphes*, i.e. those which have a BTAG number (readable from the *Delphes* tree) equal to 1.

2) For each jet, an angular distance $\Delta R = \sqrt{\Delta\eta^2 + \Delta\phi^2}$ between the jet itself and each track in the event is defined in terms of the psuedorapidity η and the azimuthal angle ϕ, according to Eq. 86. [25]

3) If the computed distance is smaller than a predefined value, set here at 0.4, then the track is considered to belong to that jet.

4) The total jet electric charge is computed through a sum of the charges of the tracks which belong to the jet itself. This sum is performed as a weighted sum, considering various options: the total momentum p, the transverse momentum p_T, or the longitudinal momentum p_L of the track, where the longitudinal direction for the track is defined with respect to jet direction. In fact, it is reasonable to expect that a track with huge momentum must give a bigger contribution than a low-momentum one in the charge computation.

The different configurations listed in the last step of the procedure have been studied in this work, in order to establish which method to attribute the weights is the best one, or the most realistic. The results from the three different methods with p, p_T and p_P as weights for the tracks are reported in Figs. 22, 23, 24, where distributions of the observable $\cos\theta$ for all the jets in the 13-million-events data set are shown.

[25] Note that this metric is dimensionless, a pure number.

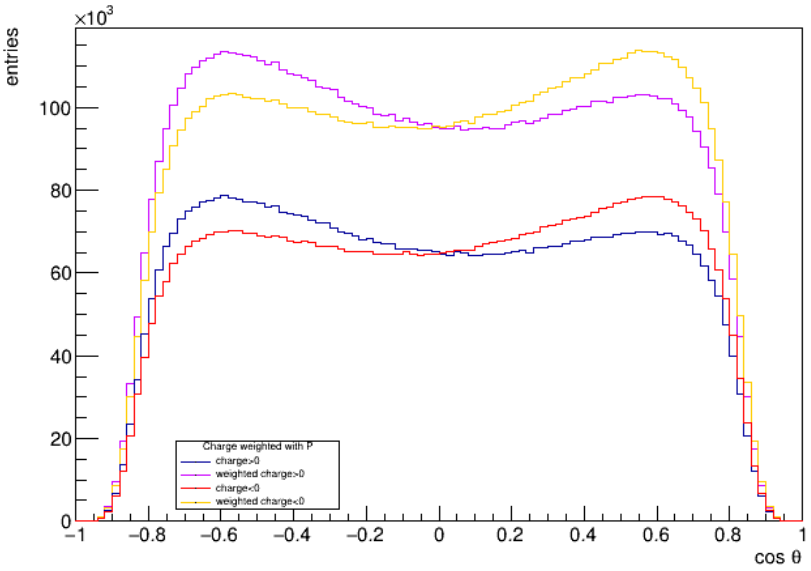

Fig. 22: Distributions of the $\cos\theta$ observable for those jets in the events which have positive (blue) or negative charge (made by a simple sum of the tracks' charges) and positive (violet) or negative (orange) weighted charge; the last two are weighted with the total momentum of the tracks.

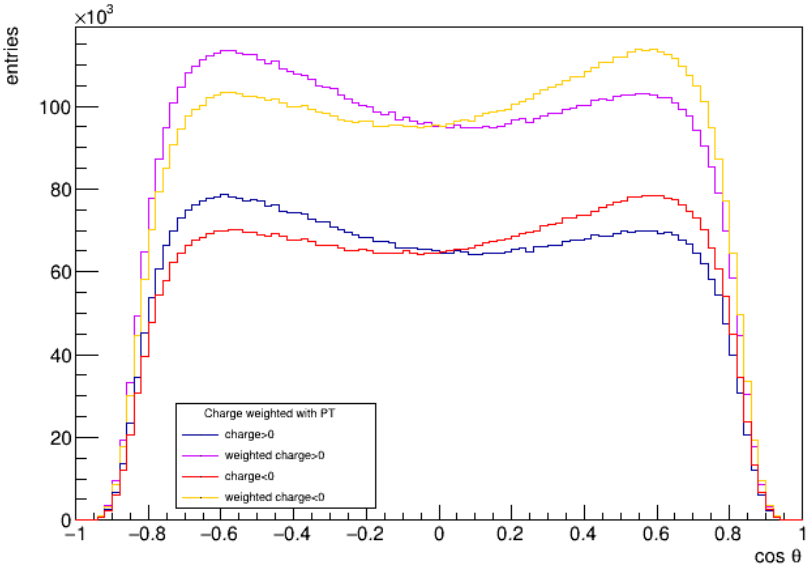

Fig. 23: Distributions of the $\cos\theta$ observable for those jets in the events which have positive (blue) or negative charge (made by a simple sum of the tracks' charges) and positive (violet) or negative (orange) weighted charge; the last two are weighted with the transverse momentum of the tracks.

The blue and red lines represent the distributions obtained if the simple sum of the tracks' charges is positive or negative (thus $Q = 0$ configurations, which are

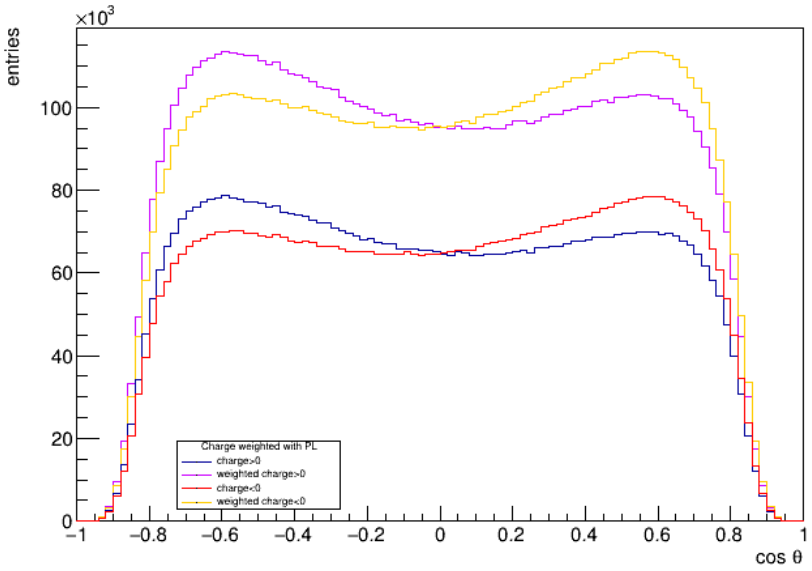

Fig. 24: Distributions of the $\cos\theta$ observable for those jets in the events which have positive (blue) or negative charge (made by a simple sum of the tracks' charges) and positive (violet) or negative (orange) weighted charge; the last two are weighted with the longitudinal momentum of the tracks.

frequently present in this simple sum of integer charges, are excluded). The violet and orange lines indicates the positive or negative weighted charge configurations, where the weight for each track is p (Fig. 22), p_T (Fig. 23) or p_L (Fig. 24) respectively; in the weighted charge computation, jets with total charge $Q = 0$ are very rare, due to the nature of the sum itself, and thus the relative statistics (violet, orange histograms) is bigger than that coming from the simple charges sum (blue, red histograms). By comparing the different ways to define the weights, it is evident that no huge difference emerges. In this work, the final choice for the weights of the tracks' charges relies on their longitudinal momentum p_L (Fig. 24).

Once the reconstructed charge of each considered jet is obtained, for each event two jets are assigned as the reconstructed b and $\bar{b}$ originated jets: the jet with the maximum value of the charge in the event is flagged as "$\bar{b}$-quark" jet, while the one with the minimum charge value is flagged as the reconstructed "b-quark" jet.

5.4 Distributions of $\cos\theta$ and unfolding procedure

As it will be detailed in Section 5.5, the extraction of A_{FB}^{b} requires the measurement of the $\cos\theta$ distributions, separately for the b and $\bar{b}$ quarks produced by the decay of the Z-bosons. These quantities, which can be defined for all the simulated signal events, are referred to as truth-level or parton-level distributions, $\cos\theta_b$ and $\cos\theta_{\bar{b}}$,

and are shown in Fig 25, with 10 bins (left side) and 1000 bins (right side).

In contrast, what can be measured by the IDEA detector, namely the angular distributions of the reconstructed flagged b-quark and $\bar{b}$-antiquark jets using the jet charge information described before, are referred to as reconstruction-level distributions. In the following, the procedure to obtain parton-level distributions from the measured reconstruction-level distributions, referred to as the unfolding procedure, is described.

The reconstruction-level distributions are defined only for events passing a set of requirements on the outputs of the detector simulation and on their processing, which constitute the so-called "event selection", meant at isolating well identified signal events from background process events (see Section 5.7) and from badly reconstructed signal events:

- the event must be characterized by at least two jets;
- at least two b-tagged jets must be present in each event;
- at least one of the selected and b-tagged jets in the event should have a positive value of the weighted charge, and at least one of them should have a negative value of it.

Fig. 26 shows the same distributions shown in Fig. 25, but considering only the events passing these selection requirements. For each of the two choices of binning, the ratio between the bin content of the parton-level distributions in Fig. 26 and Fig. 25 defines the so-called efficiency vector E: each entry of that vector represents the efficiency of the event selection for each bin of the $\cos\theta$ distributions.

Finally, Fig. 27 shows the distribution of the reconstruction-level observables, $\cos\theta(b\text{-jet})$ and $\cos\theta(\bar{b}\text{-jet})$. Again, only for those events which pass the selection.

By comparing Fig. 25 with both Fig. 26 and Fig. 27, it is clear that the original parabolic shape, which obeys to Eq. 49, is replaced by a distribution with two peaks, which represent the detector's response to the physical signal given by the differential angular distribution of events. In particular, values of $\cos\theta$ close to -1 and 1 correspond to the backward and forward regions of the detector (those with large absolute η values), where the jet and track reconstruction becomes inefficient and eventually drops to zero, reaching the limits of the calorimeter and inner tracker acceptance.

At this point, in order to build the unfolding machinery, two-dimensional histograms are created to store the correlation between the reconstructed- and truth-level distributions if the b-tagging selection occurs, for each of the two charge configurations: they provide the inputs for the creation of the *response matrices*. Such response

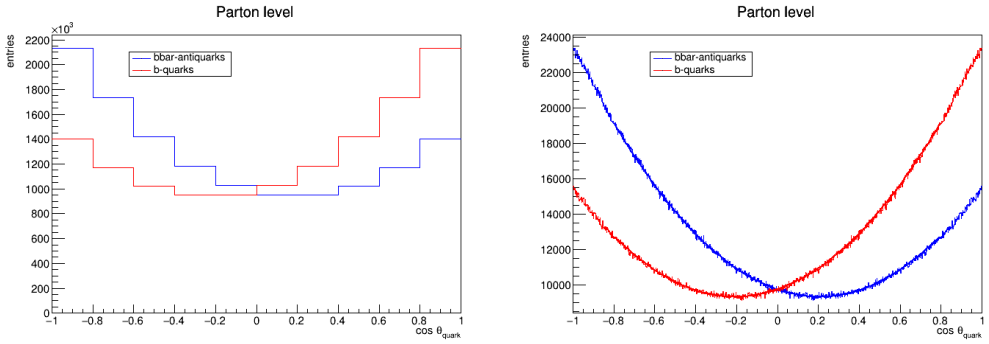

Fig. 25: Histogram for the $\cos\theta$ observable at parton (truth) level for $\bar{b}$ antiquarks (blue) and b quarks (red) for all the events generated in the data set, without any selection on the particles, with 10 bins (left side) and 1000 bins on the x-axis.

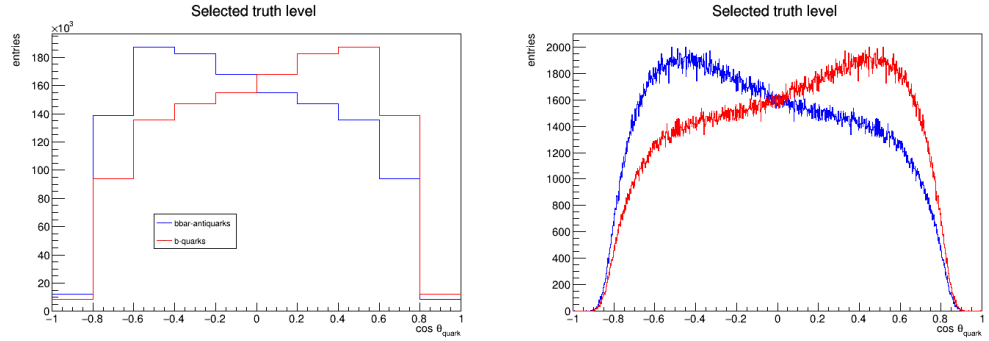

Fig. 26: Histogram for the $\cos\theta$ observable at truth level for $\bar{b}$ antiquarks (blue) and b quarks (red) for those particles which are associated to a $\bar{b}$ or a b jet, thus for those events which enter the selection, with 10 bins (left side) and 1000 bins on the x-axis.

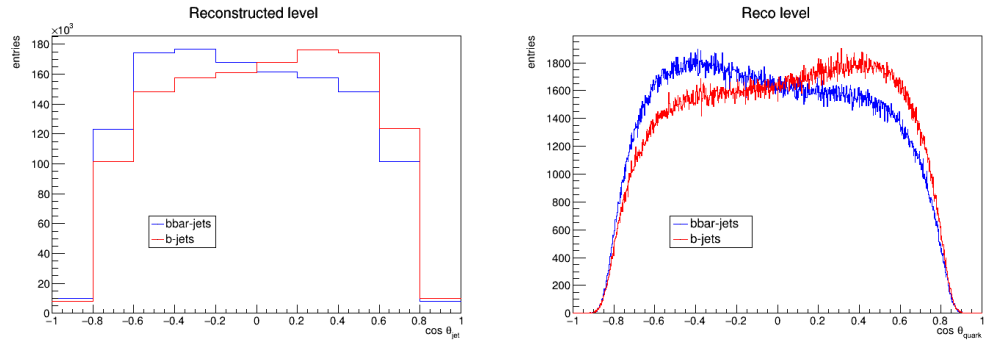

Fig. 27: Histogram for the $\cos\theta$ observable at reconstructed level in the positive (blue) and negative (red) weighted charge configurations, with 10 bins (left side) and 1000 bins (right side) on the x-axis. Jets' charges are computed as explained in 5.3.

matrices, with entries re-scaled row-by-row in order to have the sum of the cells in each row equal to one, are meant to encode all the detector and reconstruction

algorithm resolution effects, except for the selection efficiency effects, which are encoded in the efficiency vector E. Such matrices are often referred to as *migration matrices*.

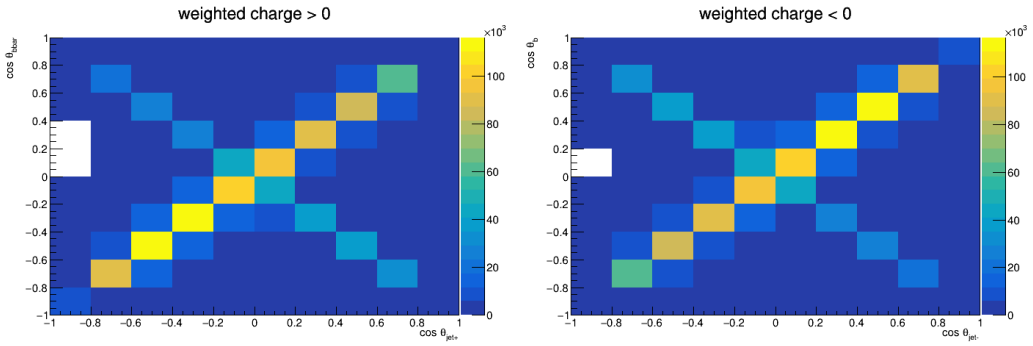

Fig. 28: 10×10 response matrices for the two charge configurations.

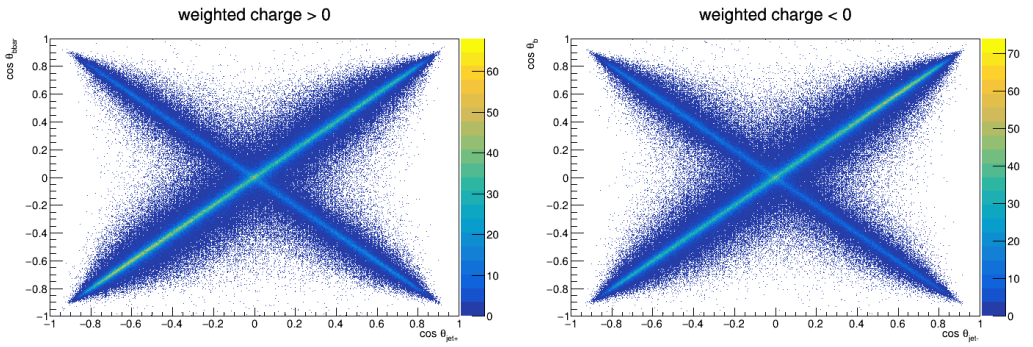

Fig. 29: 1000×1000 response matrices for the two charge configurations.

In both the positive and negative charge cases, the $\cos\theta$ values are arranged along two diagonals. The left-bottom $\rightarrow$ right-top diagonal indicates the events for which both the angle, i.e. the jet direction and its correspondent quark direction, and the charge are correctly reconstructed. Instead, the events which belong to the left-top $\rightarrow$ right-bottom diagonal can be interpreted as those for which the angle has the correct value, while the charge has opposite sign. For instance, this last class of events is made up by the configuration in which a positive jet has been wrongly associated to a b instead of a $\bar{b}$. From an experimental point of view, Fig. 29 suggests that this mis-identification is quite frequent, since in the center-of-mass reference frame b and $\bar{b}$ are emitted *back-to-back* by the Z-decaying boson, in opposite directions [30].

These response matrices are inverted numerically within the ROOT framework in order to get the *unfolding matrices*, namely U. These unfolding matrices allow to turn reconstruction-level distributions to parton-level distributions, ideally getting rid of all the detector and reconstruction bin-migration effects. The unfolding (inverse)

matrices obtained in the two charge configurations which have been considered in this study are shown in Fig. 30.

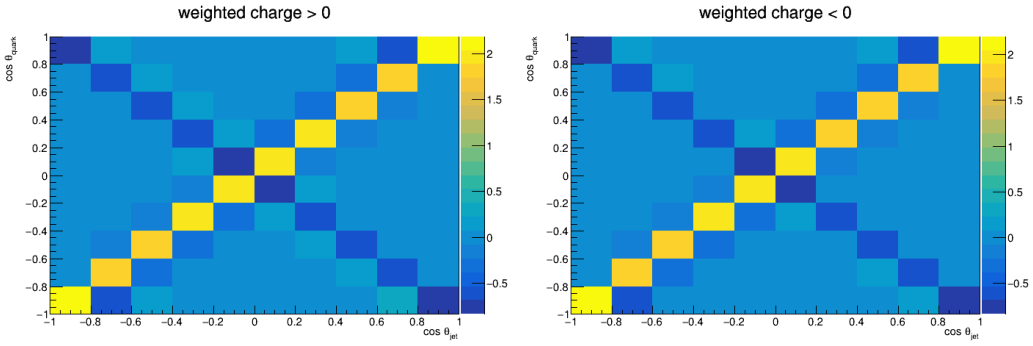

Fig. 30: 10×10 response matrices for the two charge configurations of $\bar{b}$-quark-jets (left side) and b-quark-jets (right side).

Note that, if both the inverse of the efficiency vector (E^{-1}) and the unfolding matrix (U) are applied to a reconstructed-level distribution (R for simplicity) in a certain charge configuration, it is possible to get back the original truth-level distribution (T); in compact form, the following relation must be satisfied by construction:

$$T = E^{-1} U R. \tag{94}$$

5.5 Extraction of the forward-backward asymmetry

From the truth level distributions of $\cos\theta$, the forward-backward asymmetry can be directly extracted. In fact, according to Eq. 48 based on the SM, the differential angular distributions for $\bar{b}$ and b quarks must have a quadratic form:

$$\frac{dN}{dx} = C \cdot \left(x^2 + \frac{8}{3} A_{FB}\, x + 1 \right) \tag{95}$$

where x stands in this case for the observable $\cos\theta$ [30]. Thus, thanks to a direct χ^2 fit (Eq. 95) in the ROOT framework on the truth-level distributions, it is possible to infer the A^b_{FB} value from the linear term in $\cos\theta$. The two parameters used for the fit are clearly the amplitude C, which is just an overall factor for the angular distribution and does not affect the measurement, and A_{FB} itself. Two separate fits are executed, for both the positive charge and negative charge configurations; the corresponding values are reported in Tab. 11 and are the opposites of each other, as expected from the SM.

The difference between the obtained value and that predicted in the SM (see Section 2.2 and Tab. 3) is related to the different value of $\sin\theta_W$ used in MadGraph

	Value	Error (from fit)
A_{FB}^{pos}	-0.153758	0.000334
C^{pos}	$9.74685 \cdot 10^3$	3.16882
A_{FB}^{neg}	0.153758	0.000334
C^{neg}	$9.74685 \cdot 10^3$	3.16882

Tab. 11: A_{FB}^{b} values obtained from a direct fit (Eq. 95) on truth-level distributions of $\cos\theta$ for $\bar{b}$ (first row) and b (second row), without any selection on the parton level events. The total number of events is 13 millions, and the associated integrated luminosity is $1.4\,\text{pb}^{-1}$. The error is given by the ROOT fit. The extracted values are one the opposite of the other.

with respect to the SM value [30]. To obtain the measured A_{FB}^{b} value from a certain given data-set (real data or simulated data from pseudo-experiments or systematic variations), the unfolding procedure described in Section 5.4 is applied to the reconstruction-level distributions $\cos\theta(b\text{-quark-jet})$ and $\cos\theta(b\text{-quark-jet})$, obtaining the unfolded distributions at parton-level. At this point, these unfolded distributions are fitted with Eq. 95 and the measured values of A_{FB}^{b} are extracted.

5.6 Statistical uncertainty

The measurement of $A_{FB}^{0,b}$, being based on the measurement of a distribution of event counts from a limited number of collision events, is affected by an intrinsic statistical uncertainty. In this work, the statistical uncertainty expected for a given integrated luminosity is obtained by means of a set of pseudo-experiments. The following procedure is therefore applied:

- the reconstruction-level distributions of $\cos\theta(b\text{-quark-jet})$ and $\cos\theta(\bar{b}\text{-quark-jet})$ with 10 bins on the x-axis are considered;
- the corresponding histograms are scaled up or down in order to represent a given expected integrated luminosity, by multiplying the histogram bin contents by the ratio of the target integrated luminosity [26] and the value in Eq. 91;
- statistical fluctuations are produced on top of the reconstruction-level distributions: a set of 1000 new replicas of each of the histograms is created, each time replacing the bin contents of all the bins by random numbers following Gaussian

[26] The $\cos\theta$ distributions are re-scaled by a factor in order to take into account the expected luminosity at FCC-ee. In fact, the simulated data set corresponds to an effective luminosity of $1.4\,\text{fb}^{-1}$, but actually a luminosity $\mathcal{L}_{\text{int}} \sim 150\,\text{ab}^{-1}$ is expected as a physics goal for a data-taking period of four years at the FCC-ee (see Tab. 4).

distributions, centered at the nominal value of the bin content and with the standard deviation set to be equal to the square root of the bin content;

- each of the replicas (or pseudo-data-sets) is then processed through the unfolding operation (Section 5.4), obtaining truth-level "fluctuated" distributions for $\cos\theta(b\text{-quark-jet})$ and $\cos\theta(\bar{b}\text{-quark-jet})$, with 10 bins on the x-axis each;
- each of the replicas of the parton-level distributions is then fitted with the usual quadratic formula (Eq. 95) and A_{FB}^{b} values from the b and $\bar{b}$ distributions are extracted for each replica. The fit is done in the range $-0.8 \leq \cos\theta \leq 0.8$, thus excluding the extreme bins of the distributions. This choice is motivated by the difficulty to perform a good measurements in the extreme regions due to acceptance restrictions.

In this way, for each of the two charge configurations (b and $\bar{b}$), a set of 1000 values of A_{FB}^{b} is obtained. The statistical uncertainty on A_{FB}^{b} is then obtained as the root mean squared (RMS) of the distribution of these measured A_{FB}^{b} values, for each of the two configurations.

The distributions of the fitted values of A_{FB}^{b} for the 1000 pseudo-experiments in the case of $\mathcal{L}_{\text{int}} = 1.4\,\text{pb}^{-1}$ (i.e. with no rescaling of the input reconstruction-level distributions) are shown in Fig. 31. The extracted mean and RMS values, for different assumed $\mathcal{L}_{\text{int}}$ are reported in Tab 12.

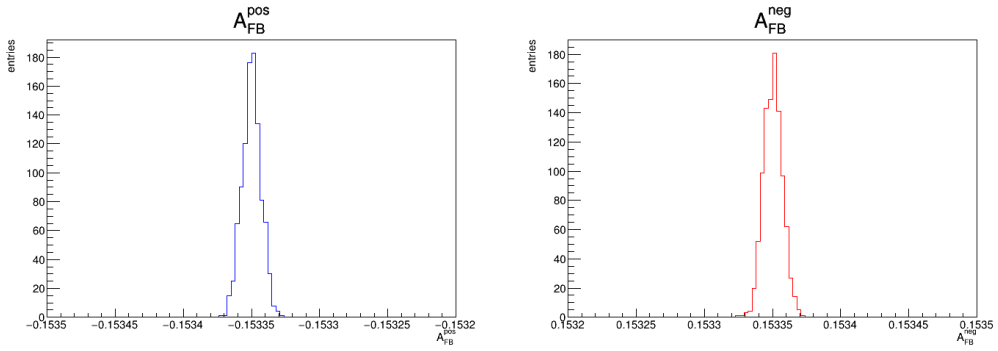

Fig. 31: Distributions of A_{FB}^{pos} (for $\bar{b}$) and A_{FB}^{neg} (for b) for 1000 pseudo-experiments. An estimation of the statistical uncertainty is given from their *root mean squared* (RMS), as shown in Tab 12.

Tab. 12 reports also the expected statistical uncertainty for an integrated luminosity of $1.4\,\text{fb}^{-1}$ (corresponding to the Monte Carlo data-set generated in this work) and of $150\,\text{ab}^{-1}$ (corresponding to the FCC-ee operations at Z-pole). The statistical contribution at $\mathcal{L}_{\text{int}} = 150\,\text{ab}^{-1}$ is of the order of 10^{-5}, showing that a precision competitive with LEP is in reach, thanks to the expected larger data set. It can

$\mathcal{L}_{\text{int}}[\text{fb}^{-1}]$	A_{FB}^{pos}	A_{FB}^{neg}
1.4	-0.153341 ± 0.000091	0.153367 ± 0.000091
$1.5 \cdot 10^5$	-0.153350 ± 0.000007	0.153350 ± 0.000007

Tab. 12: A_{FB}^{b} determination from a set of 1000 pseudo-experiments. The reported central values are the means of the distributions of the fitted A_{FB}^{b} from the $\cos\theta$ distributions for $\bar{b}$-quarks (second column) and b-quarks (third column). The uncertainties are given by the RMS of the A_{FB}^{b} distributions, shown in Fig. 31. The statistical uncertainty becomes smaller ($\sim 10^{-5}$) as luminosity increases.

be seen how, already with a small fraction of the data expected to be collected at the FCC-ee at the Z-pole, a relatively small statistical uncertainty can be obtained. With the expected $150\,\text{ab}^{-1}$ of integrated luminosity (corresponding to four years of FCC-ee operations at Z-pole, for the combination of the two experiments), the statistical uncertainty is of the order of 10^{-5}.

5.7 Inclusion of the background

Until now, only the signal process $e^+e^- \to b\bar{b}$ was considered. However, in a real experiment, events from other physics processes will enter the selection and might dilute the sensitivity of the measurement. In this work, the contribution from two main sources of background are considered:

- $c\bar{c}$ production from a decaying Z-boson;
- contribution of jets from light quarks (u, d, s).

For each of the two cases, new samples of 1 million events are generated, as mentioned in Section 5.2. Jet b-tagging and jet charge reconstruction are executed with the same procedure already shown in Section 5.3, i.e. using the weighted charge method. The reconstruction-level distribution of $\cos\theta(\bar{b}\text{-quark-jet})$ and $\cos\theta(b\text{-quark-jet})$ with 10 bins on the z-axis are extracted. The two background contributions and the $e^+e^- \to Z \to b\bar{b}$ signal are reported for the two charge configurations in Fig. 32.

Looking at Fig. 32, it is evident that the background contribution of jets originated by light quarks (red) is totally negligible, and also the relevance of the $c\bar{c}$ background (blue) is limited in the analysis: The ratio between the integrals of the reconstructed-level histograms of the $c\bar{c}$ background (blue) and the $b\bar{b}$ signal (green) is of the order of $\sim 7.0\%$.

Finally, in the presence of a background the statistical uncertainty of the A_{FB}^{b} measurement is extracted with the same procedure described before. First, the

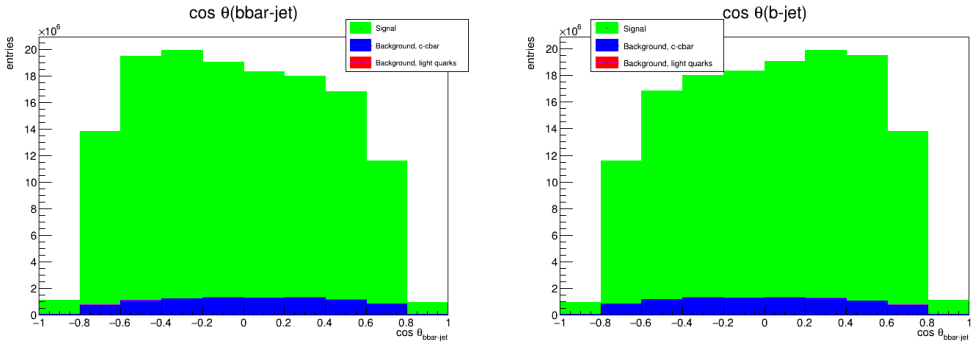

Fig. 32: Reconstructed distributions of $\cos\theta$ for $\bar{b}$-quark-jet and b-quark-jet for signal (green), light quarks background (red) and $c\bar{c}$ background (blue). The light quark-jets contribution is negligible for both distributions.

reconstructed-level distributions of the observable $\cos\theta$ are extracted by using the weighted charge method in the jet reconstruction. The background contribute is subtracted from the signal and an unfolding is done, in order to obtain the parton-level distributions. Then a set of 1000 pseudo-experiments is done. The procedure for each of them consists in the production of statistical fluctuations on top of the reconstruction-level distributions of the pure signal, after the addition of the background. A set of 1000 new replicas of each of the histograms is created, each time replacing the bin contents of the reconstruction-level distributions of all the bins by random numbers following Gaussian distributions, centered at the nominal value of the bin content and with the standard deviation set to be equal to the square root of the bin content of the distributions involving the background; in this case, since the bin content corresponds to the sum of signal and background, the fluctuations will be larger than those applied in 5.6, where no background was considered.

Then the background is subtracted to those "fluctuated" reconstructed-distributions, and through the unfolding operation (see Section 5.4) the correspondent truth-level distributions of $\cos\theta$ for b- and $\bar{b}$-quarks are obtained. By applying the usual fit (Eq. 95), for each of the two charge configurations (b and $\bar{b}$), a new set of 1000 values of A_{FB}^{b} is obtained. The statistical uncertainty on A_{FB}^{b} is then obtained as the root mean squared (RMS) of the distribution of these measured A_{FB}^{b} values, for each of the two configurations. As a result, the extracted statistical uncertainty increases of 5.5%, with respect to those reported in Tab 12, if the background is included.

5.8 Systematic uncertainties

The measurement of the b-quark forward-backward asymmetry will be affected by various sources of systematic uncertainties, which will have to be studied in details

and reduced as much as possible in order to improve the achievable precision. In this thesis, only a small number of effects are considered, among the sources expected to be most important for the measurement. In particular, the uncertainties on the *Pythia* parameters controlling the b-quark fragmentation and the QCD final state radiation, as well as the uncertainty on the fraction of background events are considered.

Modelling of b-fragmentation The modelling of the momentum transfer between the b-quark and the b-hadron is an important aspect of this analysis. The Monte Carlo event generators, such as *Pythia* or *Herwig*, describe this transfer according to phenomenological models, namely the string and cluster models containing parameters which are tuned to data. *Pythia* uses parametric functions to describe the b-quark fragmentation function. The free parameters in this model are typically fit to measurements from e^+e^- colliders.

The *Lund–Bowler parameterisation* [85] [86] in *Pythia* was used. It is given by:

$$f_z = \frac{1}{z^{1+br_b m_b^2}}(1-z)^a \exp\frac{-bm_T^2}{z} \tag{96}$$

where a, b and r_b are the function parameters, m_b is the bottom quark mass, $m_T^b = \sqrt{m_B^2 + p_T^2}$ the b-hadron transverse mass (m_B being the b-hadron mass) and z is the fraction of the longitudinal energy carried by the b-hadron with respect to the b-quark, in the b-quark reference frame. The fragmentation function is defined at the hadronisation scale and it is evolved by the parton shower to the process scale through DGLAP evolution equations [27]. In Pythia, the values of a and b were fit to data sensitive to light-quark fragmentation [87], such as charged-particle multiplicities, event shapes and scaled momentum distributions. They are assumed to be universal for light- and heavy-quarks, while the r_b parameter is specific to b-quark fragmentation.

In order to investigate the b-quark fragmentation, the most relevant parameter, r_b, is varied by changing the values of the *rFactB* variable in *Pythia*. The standard value is 0.855, and values of 0.875 and 0.835 are investigated in this study. The uncertainty for r_b is taken from [89]. The change of the value of r_b allows to give an estimation of the systematical uncertainty related to b fragmentation.

For each value for r_b, a new set of 1 million events is generated. For each set, the reco-level distributions of $\cos\theta$ are extracted for the configurations of positive and negative b-jet charge; the reconstruction of the jet charge is done with the weighted

[27] The Dokshitzer–Gribov–Lipatov–Altarelli–Parisi (DGLAP) evolution equations are equations in QCD describing the variation of parton distribution functions with varying energy scales. [88]

charge method already described in Section 5.3. Then, the corresponding original truth-level distributions are extracted by doing the actual measurement, i.e. by multiplying by the inverse efficiency vectors and the unfolding matrices already built for the initial 13-millions data set, according to Eq. 94. A new A^0_{FB} value for b and $\bar{b}$ is finally obtained by the usual fit (Eq. 95) on the truth-level distributions for b and $\bar{b}$. The difference between the upper and the lower values (Tab. 13) provides an estimation of the systematic uncertainty related to b-quark fragmentation. The results are listed below:

r_b	$A^{\text{pos}}_{FB}(r_b) - A^{\text{pos}}_{FB}(r_b = 0.855)$	$A^{\text{neg}}_{FB}(r_b) - A^{\text{neg}}_{FB}(r_b = 0.855)$
0.875	-0.0080 ± 0.0017	0.0031 ± 0.0017
0.835	0.0009 ± 0.0017	-0.0071 ± 0.0017

Tab. 13: b-fragmentation systematic uncertainty of A_{FB} for $\bar{b}$ antiquarks (second column) and b quarks (third column) for different b-fragmentation parameters, $r_b = 0.875$, 0.835.

The maximum difference is of the order of ~ 0.008 in the case of $\bar{b}$-antiquarks, and of the order of ~ 0.007 in the case of b-quarks. Thus, a value between 0.007 and 0.008 can be assigned as a first estimate for the b-fragmentation uncertainty on the A^b_{FB} measurement.

Final state QCD radiation One of the possible sources of systematic uncertainty is related to the emission of the so-called *final state QCD radiation* (FSR). The FSR is a radiation emitted by the scattered particles after the interaction, which in this case is the Z-boson production from incoming e^+ and e^- and its successive decay into a bottom quark/antiquark pair. The outgoing partons may branch, to build up final-state showers.

In this work, systematic uncertainties from FSR has been inspected varying the value of the *SpaceShower:alphaSvalue* variable, corresponding to the parameter α_S^{FSR} which is used by *Pythia* to simulate the parton shower. The standard value is 0.1365, and values of 0.25 and 0.06 are investigated. The values and the variation range are compatible to the ones used in [87]. Changing the value of α_S^{FSR} allows to give an estimation of the systematic uncertainty related to the emission of radiation in the final state.

For each value for α_S^{FSR}, a new set of 1 million events is generated, and for each set the reconstructed-level distributions of $\cos\theta$ are extracted for the configurations of positive and negative b-jet charge, with the use of the weighted charge method already described in Section 5.3. Then the corresponding original truth-level distributions

are extracted through the unfolding operation. A new $A_{FB}^{0,b}$ value is finally obtained by the usual fit (Eq. 95) on the truth-level distributions for b and $\bar{b}$. The difference between the upper and the lower values (Tab. 14) provides an estimation of the systematic uncertainty related to FSR emission, as listed below.

$\alpha_S(FSR)$	$A_{FB}^{\text{pos}}(\alpha_S) - A_{FB}^{\text{pos}}(\alpha_S = 0.1365)$	$A_{FB}^{\text{neg}}(\alpha_S) - A_{FB}^{\text{neg}}(\alpha_S = 0.1365)$
0.25	-0.0004 ± 0.0017	0.0036 ± 0.0017
0.06	0.0073 ± 0.0017	-0.0073 ± 0.0017

Tab. 14: Systematic uncertainty of A_{FB} related to the final state QCD radiation.

The maximum difference is of the order of ~ 0.007 both in the cases of $\bar{b}$-antiquarks and b-quarks. Thus, the value 0.007 can be assigned as a first, rough estimate for the systematical uncertainty on the A_{FB}^{b} measurement related to the simulation of the FSR emission.

Uncertainty on background rate The final part of this work deals with some considerations on the systematic uncertainty related to different background contributions. As shown in Fig. 32, the $c\bar{c}$ contribution is expected to be sub-dominant for the A_{FB}^{b} measurement performed in this work, with light quarks contribution being negligible.

The typical uncertainty on b-tagging and c-tagging efficiency are typically of the order of $\sim 5\%$ and $\sim 10\%$ respectively. Thus, it is reasonable that the $c\bar{c}$ reconstruction efficiency has an uncertainty of $0.1 \cdot 0.1 = 0.01$. If the c-tagging efficiency is incremented by 10%, so if it becomes 0.11, then the corresponding $c\bar{c}$ efficiency will result to be 0.0121, so that the related background increases by roughly 20%.

Following these considerations, in this study the the $c\bar{c}$ background (in red in Fig. 32) is scaled up and down of a fraction of 20% and then added to the signal, bin per bin, using the same procedure already described in Section 5.7, according with the relationship:

$$D = S + k \cdot B \tag{97}$$

where S and B indicate the signal and the background, and k assumes the values 1, 0.8 and 1.2. From these pseudo-data distributions, D, the nominal expected background B is then subtracted and the unfolding procedure and the fit are performed in order to get the corresponding values for A_{FB}^{b}. A systematic uncertainty related to the background prediction can be set as the maximum difference among these values.

It is interesting to note that the systematic uncertainty on background rate, which

k	$A_{FB}^{\mathrm{pos}}(k) - A_{FB}^{\mathrm{pos}}(k=1)$	$A_{FB}^{\mathrm{neg}}(k) - A_{FB}^{\mathrm{neg}}(k=1)$
1.2	-0.0003 ± 0.0005	0.0003 ± 0.0005
0.8	0.0003 ± 0.0005	-0.0003 ± 0.0005

Tab. 15: Systematic uncertainty of A_{FB} related to $c\bar{c}$ background rate for $\bar{b}$ antiquarks (second column) and b quarks (third column) for different k values, $k = 1.2, 0.8$.

can be quantified in $\sim 3 \cdot 10^{-4}$, is very small. Indeed, this uncertainty is comparable with the error given by the fit procedure $\sim 10^{-4}$.

Chapter 6

6 Conclusions and future perspectives

In this thesis, $e^+e^- \to b\bar{b}$ events have been generated at a center-of-mass energy of 91.188 GeV, corresponding to the Z-boson mass, through a parametric Monte Carlo simulation based on the *Delphes* software. The so-called "jet charge measurement" is performed to extract to electric charge of the b- and $\bar{b}$-jets. An unfolding machinery is built in order to pass from the reconstructed-level to the parton-level distributions of the $\cos\theta$ observable. The $\cos\theta$ distributions are then re-scaled by a factor in order to take into account the expected luminosity of $150\,\mathrm{ab}^{-1}$ for a data-taking period of four years at the FCC-ee. The A^b_{FB} value is extracted thanks to a fit in the ROOT framework applied on the truth-level angular distributions, according to Eq. 95. Additional considerations on the statistical and systematic uncertainties are presented. The final A^b_{FB} value obtained in this work, for an expected integrated luminosity of $150\,\mathrm{ab}^{-1}$ is:

$$A^b_{FB} = 0.153 \pm 0.011(\mathrm{syst}) \pm 7 \cdot 10^{-6}(\mathrm{stat}) \tag{98}$$

where the total systematic uncertainty is given by the sum in quadrature of the different sources considered, related to the b-fragmentation, the simulation of the FSR emission and the variation of the background rate. It is also clear that the statistical contribution to the error is very small, showing that a better precision than LEP is at reach.

On the other side, the estimated systematic uncertainties are significantly larger than those in the measurements by the LEP experiments (see [28]). This suggests that deeper studies will need to be performed in order to access more accurately the expected size of these systematic uncertainties, eventually foreseeing calibration procedures for the most delicate parts of the analysis, in particular for the jet charge determination. Therefore, new and more accurate studies will need to rely on this framework. In addition, alternative or more sophisticated analysis strategies will need to be investigated and compared, in particular the usage of the soft-muon-tagging (see Section 4.2.6) or even machine-learning techniques for the b-quark determination. At the time of writing, a new framework, called *EDM4hep*, is under development with the aim to realize a complete simulation for feasibility studies at future accelerators.

References

[1] D. J. Griffiths and D. F. Schroetter. *Introduction to Quantum Mechanics*, Third Edition, Cambridge University Press, 2018.

[2] M. E. Peskin and D. V. Schröder. *An Introduction To Quantum Field Theory*, CRC Press, Taylor and Francis Group, 1995.

[3] Chinese Physical Society (Particle Data Group). *Chinese Physics C* (Vol. 38, No. 9): Review of Particle Physics, Science Press and IOP Publishing, 2014.

[4] S. L. Glashow, Nucl. Phys. **22**, 579 (1961);
A. Salam and J. C. Ward, Phys. Lett. **13**, 168 (1964);
S. Weinberg, Phys. Rev. Lett. **19**, 1264 (1967);
P. W. Higgs, Phys. Lett. **12**, 132 (1964); Phys. Rev. Lett. **13**, 508 (1964); Phys. Rev. **145**, 1156 (1966).

[5] D. Griffiths, *Introduction to Elementary Particles*, John Wiley and Sons, Inc., 1987.

[6] M. Gell-Mann, Y Ne'eman. *The Eightfold way: a review with a collection of reprints*, 1964.

[7] S. L. Glashow. *Charm: An Invention Awaits Discovery*, Conf. Proc. **21**, 387-392 (1974).

[8] E288 Collaboration, J. Yoh. *The Discovery of the b Quark at Fermilab in 1977: The Experiment Coordinator's Story*, AIP Conf. Proc. **424** 1, 29-42 (1998).

[9] F. Abe *et al.* (CDF Collaboration). *Observation of Top Quark Production in $\bar{p}p$ Collisions*, Phys. Rev. Lett. **74**, 2626-2626 (1995), arXiv:hep-ex/9503002.

[10] J. D. Jackson. *Classical Electrodynamics*, Third Edition. John Wiley and Sons, Inc., 1999.

[11] B. M. Peterson and B. Ryden. *Foundations of Astrophysics*, Pearson Education Inc., 2011.

[12] J. Beringer *et al.* (Particle Data Group). *Higgs Boson: Theory and Searches*, Physical Review D and the PDG, 2012.

[13] Y. Ne'eman, Y. Kirsh. *The particle hunters*, Second Edition, Cambridge University Press, 1996.

[14] P. A. M. Dirac, Proc. Roy. Soc. Lond. **A133**, 821, 60 (1931).

[15] W. Greiner. *Relativistic Quantum Mechanics-Wave Equations*, Third Edition, Springer (2000).

[16] J.B. Hartle, *Gravity: An Introduction to Einstein's General Relativity*, Pearson Education Inc., 2003.

[17] J. C. Peng and J. W. Qiu, *The Drell-Yan Process*, Popular Science Article Vol. 4, No. 3, 2016.

[18] D. H. Perkins, *Introduction to High Energy Physics*, Third Edition, Addison-Wesley Publishing Company, Inc., 1987.

[19] N. Cabibbo, Phys. Rev. Lett. **10** (1963) 531.

[20] M. Kobayashi and T. Maskawa, Prog. Theor. Phys. *49* (1973) 652.

[21] M. Battaglia, A. J. Buras, P. Gambino and A. Stocchi, *The CKM matrix and the Unitarity Triangle*, arXiv:hep-ph/0304132, 2003.

[22] M. D'Onofrio and K. Rummukainen, *Standard Model Cross-Over on the Lattice*, arXiv:1508.07161 [hep-ph], 2015.

[23] M. Thomson, *Modern Particle Physics*, Cambridge University Press, 2013.

[24] P. A. Zyla *et al.* (Particle Data Group), Prog. Theor. Exp. Phys. **2020**, 083C01 (2020).

[25] A. J. Macfarlane, A. Sudbery and P. H. Weisz, *On Gell-Mann's λ-matrices, d- and f-tensors, octets, and parametrizations of SU*(3). Commun. Math. Phys. **11**, 77–90 (1968). https://doi.org/10.1007/BF01654302.

[26] R. C. Walker *et al.*, Phys. Rev. D49, 5671 (1994).

[27] T. Bose, A. Boveia, C. Doglioni, S. P. Griso, J. Hirschauer, E. Lipeles, Z. Liu, N. R. Shah, L. T. Wang and K. Agashe, *et al.*, Report of the Topical Group on Physics Beyond the Standard Model at Energy Frontier for Snowmass 2021, [arXiv:2209.13128 [hep-ph]].

[28] The ALEPH, DELPHI, L3, OPAL, SLD Collaborations, the LEP Electroweak Working Group, the SLD Electroweak and Heavy Flavour Groups, Physics Reports **427** (2006) 257.

[29] S.P. Martin, *A Supersymmetry Primer*, arXiv:hep-ph/9709356v6, 6 Sep 2011.

[30] R. Tenchini and C. Verzegnassi, *The Physics of the W and Z Bosons*, World Scientific, 2007.

[31] C. H. Chen, C. Q. Geng and I. L. Ho, *Forward backward asymmetry in* $K^+ \to \pi^+ l^+ l^-$, Phys. Rev. D **67** (2003), 074029 doi:10.1103/PhysRevD.67.074029 [arXiv:hep-ph/0302207 [hep-ph]].

[32] D. Liu, J. Liu, C. E. M. Wagner and X. P. Wang, *Bottom-quark Forward-Backward Asymmetry, Dark Matter and the LHC*, Phys. Rev. D **97** (2018) no.5, 055021 doi:10.1103/PhysRevD.97.055021 [arXiv:1712.05802 [hep-ph]].

[33] W. Hollik, *Precision Tests of the Standard Model*, World Scientific (Singapore), **37** (1995).

[34] W. Beenakker, F. A. Berends, S. C. Van Der Marck, Nucl. Phys. **B349** (1991) 323.

[35] D. Bardin *et al.*, Z. Phys. C44 (1989) 493.
D. Bardin *et al.*, ZFITTER v6.10 "A Semi-Analytical Program for Fermion Pair Production in e^+e^- Annihilation", DESY 99-070, hep-ph/9908433 (1999).

[36] ALEPH Collaboration, Eur. Phys. J **C14** (2000) 1;
DELPHI Collaboration, Eur. Phys. J **C16** (2000) 371;
L3 Collaboration, Eur. Phys. J **C16** (2000) 1;
OPAL Collaboration, Eur. Phys. J **C19** (2001) 587.

[37] A. Leike, T. Riemann, J. Rose, Phys. Lett. **B273** (1991) 513.

[38] R. G. Stuart, Phys. Lett. **B272** (1991) 353.

[39] JADE Collaboration, Z. Phys. **C33** (1986) 23.
JADE Collaboration, Phys. Lett. **B213** (1988) 235.

[40] ALEPH Collaboration, Eur. Phys. J. **C24** (2002) 177;
DELPHI Collaboration, Eur. Phys. J. **C34** (2004) 109;
L3 Collaboration, Phys. Lett. **B448** (1999) 152;
OPAL Collaboration, Phys. Lett. **B577** (2003) 18;
ALEPH Collaboration, Eur. Phys. J. **C22** (2001) 201;
DELPHI Collaboration, Eur. Phys. J. **C40** (2005) 1;
L3 Collaboration, Phys. Lett. **B439** (1998) 225;

OPAL Collaboration, Phys. Lett. **B546** (2002) 29;
ALEPH Collaboration, Phys. Lett. **B434** (1998) 415;
DELPHI Collaboration, Eur. Phys. J. **C10** (1999) 219;
OPAL Collaboration, Z. Phys. **C73** (1997) 379.

[41] ALEPH, DELPHI, L3, OPAL Collaborations, Nucl. Instr. Meth. **A378** (1996) 101.

[42] G. Altarelli and B. Lampe, Nucl. Phys. **B391** (1993) 3;
V. Ravidran and W. L. van Neerven, Phys. Lett. **B445** (1998) 214;
S. Catani and M. Seymour, JHEP **9907** (1999) 023.

[43] D. Abbaneo *et al.*, Eur. Phys. J **C4** (1998) 185.

[44] The Gfitter Group., J. Haller, A. Hoecker, *et al.*. Update of the global electroweak fit and constraints on two-Higgs-doublet models. *Eur. Phys. J. C* **78**, 675 (2018). https://doi.org/10.1140/epjc/s10052-018-6131-3.

[45] M. Cobal, G. Guerrieri and G. Panizzo. *Study of the Z-boson couplings to heavy fermions at the FCC-ee*, 3^{rd} FCC-France/Higgs ElectroWeak Factory Workshop, Annecy, 30/11/2021-02/12/2021.

[46] M. Pinamonti, *Measurement of the top-antitop production cross setion with the ATLAS experiment at the LHC*, PhD Thesis in Physics, University of Trieste (2011).

[47] D. Schulte. ICFA Beam Dyn. Newslett. **72**, 99 (2017).

[48] A. Blondel, M. Koratzinos, R. W. Assmann, A. Butterworth, P. Janot, J. M. Jimenez, C. Grojean, A. Milanese, M. Modena, J. A. Osborne, F. Zimmermann, H. Piekarz, K. Oide, K. Yokoya, J. Ellis, M. Klute, M. Zanetti, M. Velasco, V. Telnov, L. Rivkin, Y. Cai, *LEP3: A High Luminosity e^+e^- collider to Study the Higgs Boson* (2012), arXiv:1208.0504 [physics.acc-ph].

[49] T. Behnke, J. E. Brau, B. Foster, J. Fuster, M. Harrison, J. McEwan Paterson, M. Peskin, M. Stanitzki, N. Walker, H. Yamamoto, *The International Linear Collider Technical Design Report Volume 1: Executive Summary* (2013), arXiv:1306.6327 [physics.acc-ph].

[50] Linear Collider Board, *Conclusions on the 250 GeV ILC as a Higgs Factory proposed by the Japanese HEP community*, Presentation (November, 2017) http://icfa.fnal.gov/wp-content/uploads/LCB-Short-Conclusion-Nov2017.pdf.

[51] K. Fujii, C. Grojean, M. E. Peskin, T. Barklow, Y. Gao, S. Kanemura, H. Kim, J. List, M. Nojiri, M. Perelstein, R. Poeschl, J. Reuter, F. Simon, T. Tanabe, J. D. Wells, J. Yu, M. Berggren, M. Habermehl, S. Jung, R. Karl, T. Ogawa, J. Tian, J. Brau, H. Murayama, *Physics Case for the 250 GeV Stage of the International Linear Collider* (2017), arXiv:1710.07621 [hep-ex].

[52] M. Aicheler, P. Burrows, M. Draper, T. Garvey, P. Lebrun, K. Peach, N. Phinney, H. Schmickler, D. Schulte, N. Toge, *A Multi-TeV Linear Collider Based on CLIC Technology, CERN Yellow Reports: Monographs* (CERN, Geneva, Switzerland, 2012) https://cds.cern.ch/record/1500095

[53] CLICdp, CLIC Collaboration, M. J. Boland *et al.*, *Updated baseline for a staged Compact Linear Collider*, DOI: 10.5170/CERN-2016-004.

[54] CEPC-SPPC Study Group, *CEPC-SPPC Preliminary Conceptual Design Report. 1. Physics and Detector* (2015), IHEP-CEPC-DR-2015-01, IHEP-TH-2015-01, IHEP-EP-201501.

[55] CEPC Study Group, *CEPC Conceptual Design Report* (IHEP, CAS, 2018), arXiv:1809.00285 [physics.acc-ph], IHEP-CEPC-DR-2018-01, IHEP-AC-2018-01.

[56] A. Blondel, P. Janot, *et al.*, *FCC-ee: Your Questions Answered*, Contribution to the European Particle Physics Strategy Update 2018-2020, arXiv:1906.02693v1 [hep-ph] (2019).

[57] A. Abada, M. Abbrescia, S. S. Abdus Salam, *et al.*, FCC-hh: The Hadron Collider. *Eur. Phys. J. Spec. Top.* **228**, 755–1107 (2019). https://doi.org/10.1140/epjst/e2019-900087-0.

[58] A. Abada, M. Abbrescia, S. S. Abdus Salam, *et al.* FCC-ee: The Lepton Collider. *Eur. Phys. J. Spec. Top.* **228**, 261–623 (2019). https://doi.org/10.1140/epjst/e2019-900045-4.

[59] M. Tanabashi *et al.* (Particle Data Group), *Review of particle Physics*, Phys. Rev. D, vol. 98, 17^{th} August 2018, pp. 030001.

[60] The ATLAS collaboration, *The ATLAS Experiment at the CERN Large Hadron Collider*, JINST 3 (2008) S08003.

[61] M. Hauschild, *Detectors, an introduction*, CERN seminar.

[62] W. R. Leo, *Techniques for Nuclear and Particle Physics Experiments*, Second Revised Edition, Springer-Verlag, 1994.

[63] N. Bacchetta, J. -J. Blaising, E. Brondolin, M. Dam, D. Dannheim, K. Elsener, D. Hynds, P. Janot, A. M. Kolano, E. Leogrande, L. Linssen, A. Nürnberg, E. F. Perez, M. Petrič, P. Roloff, A. Sailer, N. Siegrist, O. Viazlo, G. G. Voutsinas, M. A. Weber, *CLD - A Detector Concept for the FCC-ee*, arXiv:1911.12230 (2019).

[64] B. Francois, FCC Noble Liquid Calorimetry group, *Noble liquid calorimetry for a future FCC-ee experiment*, Nucl. Inst., 1040 (2022).

[65] I. Vivarelli, *The IDEA detector*, 4^{th} FCC Physics and Experiments Workshop, 10-13 November 2020.

[66] ALICE Collaboration, M. Mager, Nucl. Instrum. Meth. A **824**, 434 (2016).

[67] ALICE Collaboration, G. Aglieri Rinella, Nucl. Instrum. Meth. A **845**, 583 (2017).

[68] G. Chiarello, C. Chiri, A. Corvaglia, F. Grancagnolo, A. Miccoli, M. Panareo, A. Pepino, C. Pinto, P. Primiceri, M. Spedicato and G. F. Tassielli, Nucl. Instrum. Methods Phys. Res. A **824**, 512 (2016).

[69] DREAM Collaboration, R. Wigmans, Nucl. Instrum. Meth. A **617**, 129 (2010).

[70] N. Akchurin, F. Bedeschi, A. Cardini, M. Cascella, D. De Pedis, R. Ferrari, S. Fracchia, S. Franchino, M. Fraternali, G. Gaudio, P. Genova, J. Hauptman, L. La Rotonda, S. Lee, M. Livan, E. Meoni, D. Pinci, A. Policicchio, J. G. Saraiva, F. Scuri, A. Sill, T. Venturelli, R. Wigmans, Nucl. Instrum. Methods Phys. Res. Sect. A **735**, 120 (2014).

[71] G. Acquistapace , J. Andre, M. H. Bovard, A. Calvo, D. Campi, B. Cure, D. Delikaris, A. Desirelli, P. Fabbricatore, S. Farinon, F. Feyzi, J. C. Gelebart, H. Gerwig, J. P. Girod, J. P. Grillet, L. Greenler, G. M. Gregerson, A. Herve, I. L. Horvath, V. Kaftanov, A. Le Coroller, C. Lesmond, B. Levesy, J. C. Lottin, J. P. Lottin, R. Loveless, C. Lyraud, W. P. Mason, J. M. Maugain, R. Musenich, G. Passardi, C. Pes, P. Petiot, R. Pintus, J. Pippin, O. Pogorelko, C. Priano, J. M. Rey, F. Rondeaux, J. Y. Rousse, R. Smith, T. de Visser, L. Veillet, B. Wands, G. Waurick, *CMS, the Magnet Project: Technical Design Report* CERN-LHCC-97-10, CMS (1997).

[72] W. Lampl *et al.*, *Calorimeter Clustering Algorithms: Description and Performance*, ATL-LARG-PUB-2008-002 (2008).

[73] M. Cacciari, G. P. Salam and G. Soyez, *The anti-k_T jet clustering algorithm*, JHEP **0804**, 063 (2008), arXiv:0802.1189 [hep-ph].

[74] G. P. Salam and G Soyez, JHEP **0804**, 063 (2008), arXiv:0802.1189 [hep-ph].

[75] The CMS Collaboration, *Identification of b-quark jets with the CMS experiment*, arXiv:1211.4462 [hep-ex] (2012).

[76] S. Catani, Y. L. Dokshitzer, M. H. Seymour and B. R. Webber, *Longitudinally invariant K(t) clustering algorithms for hadron-hadron collisions*, Nucl. Phys. **B406**, 187 (1993);
S. D. Ellis and D. E. Soper, *Successive combination jet algorithm for hadron collisions*, Phys. Rev. **D48**, 3160 (1993), arXiv:hep-ph/9305266.

[77] Y. L. Dokshitzer, G. D. Leder, S. Moretti and B. R. Webber, *Better jet clustering algorithms*, JHEP **08**, 001 (1997), arXiv:hep-ph/97073223;
M. Wobisch and T. Wengler, *Hadronization corrections to jet cross sections in deep-inelastic scattering* (1999), arXiv:hep-ph/9907280.

[78] J. Alwall, M. Herquet, F. Maltoni, O. Mattelaer and T. Stelzer, JHEP **1106** (2011) 128 [arXiv:1106.0522 [hep-ph]].

[79] T. Sjostrand, S. Mrenna and P. Z. Skands, *A Brief Introduction to PYTHIA 8.1*, Comput. Phys. Commun. **178** (2008), 852-867, doi:10.1016/j.cpc.2008.01.036, [arXiv:0710.3820 [hep-ph]].

[80] S. Salis, *Reasons for an accurate measurement of the $A_{FB,Z}$ Asymmetry at the LHC and feasibility study at the ATLAS experiment*, Master Thesis in Physics, University of Trieste (2012).

[81] M. Dasgupta, F. A. Dreyer, K. Hamilton, P. F. Monni and G. P. Salam, *Logarithmic accuracy of parton showers: a fixed-order study*, Journal of High Energy Physics, vol. 2018, no. 9, Sept. 2018.

[82] *Delphes*, a framework for fast simulation of a generic collider physics experiment, arXiv:0903.2225 [hep-ph] 68.

[83] T. Aaltonen, *et al.* (CDF Collaboration), Exclusion of an Exotic Top Quark with -4/3 Electric Charge Using Soft Lepton Tagging, *Phys. Rev. Lett.* **105**, 101801 (2010).

[84] F. Abudinén, N. Akopov, A. Aloisio, *et al.* B-flavor tagging at Belle II. *Eur. Phys. J. C* **82**, 283 (2022). https://doi.org/10.1140/epjc/s10052-022-10180-9.

[85] B. Andersson, G. Gustafson, G. Ingelman and T. Sjöstrand, *Parton fragmentation and string dynamics*, Phys. Rept. **97**, 31 (1983).

[86] M. G. Bowler, e^+e^- *Production of heavy quarks in the string model*, Z. Phys. **C 11**, 169 (1981).

[87] P. Skands, S. Carrazza and J. Rojo, *Tuning PYTHIA 8.1: the Monash 2013 Tune*, Eur. Phys. J. **C 74**, 3024 (2014), arXiv: 1404.5630 [hep-ph].

[88] G. Altarelli, G. Parisi, *Asymptotic freedom in parton language*, Nucl. Phys. B. **126**, 298–318 (1997), doi:10.1016/0550-3213(77)90384-4.
L. Yu. L. Dokshitzer, *Sov. Phys. JETP* 46-641 (1977).
V. N. Gribov, L. N. Lipatov, *Sov. J. Nucl. Phys.* 15-438 (1972).

[89] The ATLAS Collaboration, *Measurement of the top-quark mass using a leptonic invariant mass in pp collisions at* $\sqrt{s} = 13$ *TeV with the ATLAS detector*, arXiv:2209.00583v1 [hep-ex] (2022).

Acknowledgements

There are many people who helped me for the realization of this Thesis.

First of all, I would like to thank my supervisors Prof. Marina Cobal and Prof. Michele Pinamonti. I am so grateful to them, for their continuous and crucial support, their advises and, last but not least, for their incredible passion for experimental particle physics they managed to instill in me. I hope to continue working in this field in the future.

I would like to thank all the colleagues from the Udine/ICTP/ATLAS/FCC group and external collaborators, who shared a lot of time with me. In particular, thank to Nitika, Mohahmed Faraj for his sympathy, Laura Pintucci for her kindness, and Leonid Serkin, to whom I wish the best for the future. A special thank to Hamzeh Khanpour for his professionalism, to Giancarlo Panizzo for his availability and to Prof. Marco Fabbrichesi for his notes.

Thank to all my friends in the Physics Master Degree: Anna, Greta, Paola, Cristiano, Francesco, Michele. They shared with me a lot of time, emotions, concerns and expectations.

I would like to thank my friends, who supported me within these years of studies. A special mention to Giacomo, who is for me the brother I have never had, and Giulia, companion of many adventures.

Finally, a special thank to my family, in particular to my parents, my aunts, my uncle, my cousin, and especially to my Grandma Emma; I hope she will be proud of myself.